EFFECT OF PHYSICAL PROPERTIES ON BREAK-UP AND ATOMIZATION OF LIQUID JETS IN A SUPERSONIC CROSSFLOW

BY

ABDOLLAH SHOKOUHI NEJAD

DISSERTATION SUBMITTED TO GRADUATE FACULTY OF THE VIRGINIA POLYTECHNIC INSTITUTE AND STATE UNIVERSITY IN PARTIAL FULFILLMENT OF THE REQUIREMENTS FOR THE DEGREE OF

DOCTOR OF PHILOSOPHY

IN

AEROSPACE ENGINEERING

J. A. SCHETZ, CHAIRMAN

A. K. JAKUBOWSKI

W. E. KOHLER

P. J. SEBBA

W. L. NEU

June, 1982

Blacksburg, VA

ACKNOWLEDGEMENTS

The author wishes to express his deepest gratitude to his advisor, Dr. J. A. Schetz, who granted this opportunity and whose invaluable technical knowledge was of great help throughout the investigation. Also, special thanks to Dr. A. K. Jakubowski for his continuous technical and moral support. Many thanks to G. Stafford, B. Baseghi and my wife Ladan for their help in this work. Thanks to J. Gay and S. Layman for typing the manuscript.

TABLE OF CONTENTS

LIST OF FIGURES

LIST OF TABLES

Nomenclature

d,D	injector diameter
D_{32}	droplet diameter
h	jet penetration height
$I(\Theta)$	normalized intensity of the scattered light
L	length of coherent zone on the jet column
Mp	freestream Mach number
NrD	a known distribution function of droplet diameters
$N\lambda F$	number of waves on the jet column
Po	freestream stagnation pressure
$\bar{q}$	ratio of dynamic pressure of jet ($\frac{1}{2}\rho_j v_j^2$) to dynamic pressure of freestream ($\frac{1}{2}\rho_\infty v_\infty^2$)
To	freestream stagnation temperature
TR	length of capillary wave zone on the jet column
v	velocity
x	distance downstream of the center of the injector
y	vertical distance from the surface of flat-plate
wv	wave speed on the jet column
wvs	wave speed on the plume near sonic point
cv	clump velocity
Θ	scattering angle
Θ	reduced angle = $\frac{\pi\Theta D_{32}}{\lambda}$
λ	wavelength
α	Amplitude
μ	viscosity of liquid injectant
ρ	density

σ	surface tension of the liquid injectant

Subscripts

j	refers to the jet
∞	refers to free airstream
p	refers to propagation
PS	refers to propagation near sonic point

I. INTRODUCTION

The practical engineering applications of transverse injection of a liquid jet into a high-speed crossflow have been the motivating force behind numerous analytical and experimental studies. Injection of liquids into high-speed crossflow has been considered in many aerospace systems such as the transverse injection of fuel into combustion chambers of ramjets and supersonic combustion ramjets, thrust vector control in rockets, injection into the supersonic airstream around projectiles for jet interaction or external burning to achieve control maneuverability and/or drag reduction, injection in the area of turbines for cooling the blades, fuel injection in the nozzle of jet engines to increase thrust. In high-speed reentry, a very hot, ionized layer of air which is the cause of "black-out" period surrounds the reentry body. In order to provide local cooling in the region of communication antenna to alleviate the blackout period, the possibility of injection of a liquid coolant has been considered.

Liquid injection processes into a supersonic airstream for thrust vector control, external burning supersonic combustion ramjets are similar. For this class of fuel injection, liquids have an advantage over the gaseous fuels. Liquids are denser, easier to handle and require lighter control systems. Also for cost, safety and availability reasons, it is likely that hydrocarbon liquid fuels will be employed as the energy source for these devices. The efficiency of the supersonic combustor of a scramjet plays an essential role in the overall performance of the scramjet vehicle. The combustion processes that are

controlled by mixing of the fuel and air and chemical heat release must be efficient at the design point and adequate at off-design regimes. The demands on the efficiency and performance of the combustor are directly linked to the injector, which places restrictions and demands on the injector/jet parameters. Therefore, such matters as liquid jet penetration, jet break-up and atomization must be clearly understood to produce an efficient design without excessive expensive trial and error testing.

All of the applications cited involve the physical processes of break-up and atomization. Some also involve chemical processes such as ignition and combustion. Even in those, however, the physical processes remain important.

The recent developments in engine design and the emergence of new hybrid fuels with large viscosity and surface tension ranges as well as the possibility of addition of new fire retardation additives which convert the fuel into a gel type substance and the problem of cold starts and the lack of complete understanding of the basic atomization processes were the motivating force behind the present experimental study of the basic effects of the physical properties of the injectant on jet penetration, break-up and atomization.

The problem of penetration and atomization of liquid jet in a crossflow has been studied both experimentally and to a lesser extent analytically. The experiments conducted by Sherman and Schetz (1,2) where large axial waves were noted on the jet and were presumed to be the dominant force of jet decomposition were the source of initial

direction. Also, the present work extends the study done by Kush and Schetz (3,4) who performed extensive experimental work to study the effects of freestream Mach number, freestream total pressure, injector diameter, injector shape and injectant flow rate on jet penetration and structure. They also reported data on wavelength, amplitude, and wave speed of the disturbances on the jet surface leading to breakup of the jet.

In a crossflow injection, the liquid jet is deformed and bent in the downstream direction by the crossflow, thus creating a three dimensional body in the flow field. The flow field about the spray plume is therefore highly three dimensional. A boundary layer separation zone upstream of the injector is produced. This is due to the interaction of the boundary layer and the bow shock caused by a transverse jet. Fig. 1 is a wide view photograph of a transverse liquid injection into Mach 3 crossflow. The boundary layer separation zone ahead of the injector, the bow shaped shock in front of the spray plume and the wave pattern on the jet surface are clearly evident. The separation zone plays an important role in combustion since the rate of heat transfer is often highest in parts of a separation zone. It might also provide the most favorable condition for auto-ignition of the fuel. The interaction shock system associated with each injector has two effects. First, the shock reduces the total pressure of the free airstream and therefore tends to reduce the overall performance. Second, because of the shock the static pressure and temperature of the free airstream will rise, therefore creating a better environment for supporting possible ignition and chemical reaction in the main airstream. Fig. 2 is

a close-up photograph of the transverse liquid jet atomization processes. The bow shaped shock, the cohesive jet body just after leaving the injector, the point of first cross fracture and the atomized region of the jet are shown. Fig. 3 is a schematic of the same processes. The spray plume is crudely divided into three regions: 1) the cohesive jet body, 2) the spray formation region, 3) the atomized region of fine droplets. In the present study, the first and second regions received primary attention. Due to the narrow view field associated with the photograph only a limited photographic study of the third region was possible.

Several types of waves appear on the spray plume windward edge. Some are small capillary disturbances and small waves which are caused by turbulence. Some are large aerodynamically induced waves which are primarily responsible for the decomposition of the jet. Two types of instability can occur, the aerodynamic drag force accelerates the liquid surface in a direction normal to its plane, thus creating Rayleigh/Taylor type instability. Also, since the transverse injection of liquids into a crossflow involves two types of fluids of different physical properties and relative velocities parallel to their interface, Kelvin/Helmholtz instability can occur. The unstable disturbances grow in time to the point of first cross fracture. The presence of the large waves alter the gas boundary layer and shock shape. Therefore, the flow over the spray is altered, which in turn produces different types of wave patterns. The viscosity and surface tension of the injectant have a direct effect on the spray plume, both internally and at its surface. They therefore determine the shape and the

characteristics of the surface waves and hence the atomization processes. It can be seen that there is an interrelationship between the shock shape, viscosity, surface tension and wave mechanisms. Therefore, a detailed study of effects of injectant physical properties on the structure of the plume in the crossflow is required.

From a theoretical point of view, this problem is very complex. A complete analysis of this three-dimensional, unsteady, two-phase, turbulent and mixed supersonic/subsonic problem requires understanding of several related disciplines, such as supersonic aerodynamics, fluid physics, vicous flow, and hydrodynamics. This makes a comprehensive analysis of the full problem prohibitive at this time. Analysis of idealized versions of the problem have appeard.

Liquid jets entering a motionless gaseous medium will eventually break up into droplets. Accounting for an explanation of the decomposition of liquid jets has been the motivation for numerous studies in the past. It has been postulated that, since the surface energy of the liquid jet is not at a minimum, the jet breaks up into spherical particles to reach a minimum stable state. Rayleigh (5,6) was the first to investigate this problem while neglecting viscosity and the effects of the surrounding air. Using linearized analysis, he found that all symmetric disturbances with wavelengths less than the initial jet circumference were stabilized by the damping effect of surface tension. For disturbances greater than the circumference of the jet ($\lambda_{crit} = 2\pi d$) he found that the surface tension increased the disturbance growth, causing the liquid jet to break up. Weber (7) continued

the work of Rayleigh but added the effects of viscosity and the surrounding air. He also studied the effects of symmetric and anti-symmetric disturbances which occur due to Kelvin/Helmholtz instability at high jet velocity. Tomotica (8) furthered the work of Rayleigh by injecting a viscous jet into another viscous medium. Castleman (9,10) conducted an analysis of the work of many previous investigators and reported that the disturbances on the jet grow to become large waves, and when they attain sufficient amplitude they break up into ligaments, which in turn decompose very rapidly into droplets. Dunne and Cassen (11) investigated supersonic velocity jets and showed that symmetrical waves are formed on the jet. York (12) theoretically studied the problem and stated that wave formation is due to instability, and their growth is the major cause of jet break up and droplet formation. Most of the theoretical works have used linearized theory. In recent years some investigators, e.g., Yune (13) and Nayfeh (14) have analyzed the non-linear stability of a liquid jet. Nayfeh presented a non-linear analysis for the capillary stability of the cylindrical column of a liquid using the method of multiple time scales; he obtained a second order expansion. He reported that the cut-off wave number which separates the stable from the unstable disturbances is amplitude dependent. Axisymmetric disturbances with wave number greater than $K' = (1+3a^2/4R^2)R^{-1}$ oscillate and are stable. However, the frequency of the oscillation is amplitude dependent, contrary to the linearized results. Below this cut-off wave number disturbances grow with time.

A problem of greater practical interest is that of injection of a liquid jet into a crossflow. This topic was not addressed in detail

until recently, and the majority of the works are exercises in understanding the instability of the jet and predicting a mechanism for break-up and decomposition. First, the theories of wind generated waves on a plane liquid surface were established and then applied to this problem. Kelvin (15) studied the generation of wind driven waves over a frictionless fluid. Jeffreys (16) furthered Kelvin's work by introducing the concept of "sheltering" for stable disturbances. He assumed that flow separated at the crest of the wave and used an energy balance at the wave surface. He also introduced an arbitrary constant. This model was proven to be wrong by Lighthill (17,18). He showed that in the wind axis, the velocity at the crest is opposite to the free-stream direction, therefore the separation should occur on the windward portion of the wave. Chang and Russell (19) using a linearized approach studied the stability behavior of two dimensional liquid layer adjacent both to subsonic and supersonic gas streams. Adelberg (20) theoretically estimated the mean droplet diameter generated by a liquid jet penetrating a gaseous environment. He divided the flow field into four separate regions according to relative dynamic pressure and treated the two regions having the higher dynamic pressure. He stated that the mechanism of ligament formation and shedding appears to be good model for droplet formation in the case of high relative velocity between liquid jet and the surrounding gas stream. The analytical results were compared with experimental results obtained by Weiss and Worsham and was found in good agreement with experimental results. He also compared his results with Mayer's analysis (21) and found that his predicted droplet diameter was different from that of Mayer's.

Some of Adelberg's base assumptions have been criticized on physical grounds however.

Joshi, Jakubowski and Schetz (22) have investigated the effects of injector geometry on penetration and structure of a liquid jet. They found a relation between penetration and the jet/freestream dynamic pressure ratio. They also found the dependence of penetration on the ratio of the frontal to the streamwise dimensions of the injector. It was observed that for a given mass flow rate of injectant, a rectangular injector has the highest penetration and spread.

Experiments were performed by Chelko (23) and Foster and Ingebo (24) in subsonic streams. Foster and Ingebo measured droplet diameter using a microphotographic technique. Studies by Schetz, McVey and Padhye (25) focused on the behavior of the liquid jet injected normal to a transonic airstream and reported the droplet size distribution, employing a microphotographic technique. They concluded that: a) the mean droplet diameter size was of the order 10^{-2} cm., b) for a given injector and airstream condition, the mass flow rate of the injectant did not affect droplet size, c) an increase in orifice diameter of the injector increased the mean droplet diameter size, d) an increase in the crossflow Mach number decreased mean droplet diameter, e) injector geometry has significant effect on mean droplet diameter. Weiss and Worsham (26) studied the atomization of molten Acrawax-c jets in a high velocity airstream and obtained the diameter of the frozen jet particles. They concluded that the particles were almost uniformly spherical. They also studied the effect of airstream density, relative velocity, liquid viscosity, mass flow rate and injector diameter on

droplet diameter. It was concluded that the relative velocity between the airstream and the liquid jet is of prime importance and that physical properties do effect spray fineness, but their influence is less critical. They also correlated the results empirically by a dimensionless equation. Clark (27) studied transverse jets in low velocity crossflow and developed a model for breakup of flat liquid streams with energy input by shear. Forde, Medler and Szpiro (28) constructed a simple theoretical model (based on Newtonian flow) for prediction of injectant path and hence the penetration distance for secondary liquid injection into a supersonic stream. The experiments showed that it is possible to achieve significant penetration distance by injection from a wall orifice into a Mach 3 supersonic airstream, they reported that: a) their model predicted the penetration height with reasonable accuracy, b) the maximum penetration is dependent on injectant total pressure, the angle of injection and injector diameter, c) upstream injection produced the largest penetration height, whereas a small downstream angle gave a slightly greater penetration than the normal injection. Reichenbach and Horn (29) experimentally investigated the effects of liquid properties on secondary injection from a small diameter nozzle in a supersonic stream. They studied the effects of vapor pressure on penetration by injecting super-heated water and Acetone. Penetration height was correlated with injector pressure ratio for super-heated liquid injection. This data was compared with room temperature results. They concluded that vapor pressure break-up outside of the spray had little effect on penetration. The effects of viscosity and surface tension were also studied over a small range.

They reported that neither property affected the penetration height for flow in the acceleration wave break-up regime.

Horn and Reichenbach (30) investigated the penetration and the width spread of a liquid jet in a supersonic flow. They presented information on lateral spread of the jet and stated that the lateral spreading width has a weak dependence on the injector pressure ratio and also is weakly dependent upon Mach number. Shaikhutdinov and Klevanskii (31) examined the three dimensional boundaries of the atomized plume in Mach 2.5 crossflow by means of temperature survey method. They presented relations for penetration height cross sectional shape and mixing characteristics.

Most of the work that has been reported examines the atomization process and droplet formation by means of direct photographic techniques. Less work has been done to develop other means of studying the structure of the jet spray in the crossflow. The application of the light scattering technique in studying the droplet size is relatively new. Chin, Sliepeevich and Tribus (32) were among the early researchers to investigate this technique, using a theory by Grumprecht and Sliepeevich (33) which describes the scattering properties of polydispersion. Dobbins, Crocco and Glassman (34) are responsible for the formation of a theory for the scattering properties in the more general case of particles of arbitrary refractive index occurring in polydispersion of finite optical depth. Mugel and Evans (35) have introduced the Upper Limit Distribution Function (ULDF) which establishes a correct volume fraction curve and therefore accurate mean droplet diameter. Roberts and Webb (36) studied the accuracy of the

diffractively scattered light technique in measuring particle size by using many different distribution functions. They concluded that the value of the mean droplet diameter D_{32} may be determined to a high accuracy for an extremely wide range of distribution shapes from the intensity of diffractively scattered light from a poly-dispersion of spherical particles without the knowledge of the specific distribution type. Gooderum and Bushnell (37) conducted a study of atomization, droplet size and penetration measurements for cross-stream water injection at high reentry conditions. They employed the scattered light technique in measuring the mean droplet diameter. Data was obtained both in a static environment and in conventional aerodynamic facilities at Mach numbers of 4.5 and 8.0. It was concluded that the mean droplet size for vapor pressure break-up in the absence of external flow is directly proportional to orifice diameter and is an inverse function of the absolute temperature of the injectant. They also reported that droplet size resulting from injection into Mach 8 Cyanogen-Oxygen tunnel was independent of injectant (water) velocity. Bitron (38) used an impact collection method of dibutyl phethalate droplets to measure the droplet sizes, Kurzious and Rabb (39) have studied many aspects of transverse injection and have reported the existence of large axial waves and their influence upon atomization of the jet. Nejad, Schetz and Jakubowski (40) investigated the feasibility of employing the diffractively scattered light method for routine measurements of the droplet diameter in the spray resulting from normal injection of water into supersonic airstream under the high density condition of a blow down type wind tunnel. They reported that the technique is capable of

measuring the mean droplet diameter in the spray with good experimental accuracy. Lorenzetto (41) studied the mean droplet diameter resulting from an air blast atomizer in which the fuel was injected into a co-axial high velocity airstream in the form of a discrete jet. The effects of viscosity, surface tension and density of the injectant on the mean droplet diameter was included.

The present study is concerned with providing a wide range of data and establishing the individual effects of surface tension and viscosity on atomization and structural behavior of a transverse jet. No attempt has been made to further or modify the existing analytical work of previous studies. However, the experimental plan was developed to specifically provide information that is critical in formulating and/or refining theories. This study utilized both the photographic and scattering techniques. Three types of direct photographic methods were used: a) streak shadowgraph with an exposure time of 10^{-3} sec., to record a time averaged jet profile in the crossflow for the purpose of penetration measurements, b) to study the instantaneous structure of the jet crossflow, stop action, spark photography with an exposure time of 9×10^{-9} sec., c) two types of multi-exposure high-speed stop action photographic techniques with exposure times of 8×10^{-7} sec. were developed to study the speed of the surface waves relative to the liquid bulk velocity and clumps in the crossflow.

The scattering technique which was developed for high density wind tunnel applications (40) was utilized to provide information about the droplet diameter variation along and across the spray plume.

The individual effects of injectant density, injectant mass flow

rate, injectant velocity, free-stream velocity and free-stream stagnation pressure were investigated by injection of liquid jets through a wide range (1-20) of jet-free-stream dynamic pressure ratios $\bar{q} = (\rho_j v_j^2 / \rho_\infty v_\infty^2)$. To investigate the influence of injectant physical properties, such as surface tension or viscosity on the spray plume characteristics, plentiful and safe liquid injectants with variable surface tension and fixed viscosity or vice-versa were required. The following plan was adopted (Table 1): a) pure water was used as reference injectant with a surface tension of 73.0 dyne/cm. and viscosity of 1.0 centipoise at 20 degrees Centigrade, b) solutions of different Glycerine concentrations in water were prepared to provide injectants with constant surface tension of 73.0 dyne/cm. and viscosities ranging from 10.6 to 59.8 centipoise, c) ethyl alcohol was added to water which reduced the surface tension to 33.5 dyne/cm. while allowing the viscosity to stay roughly at 1.0 centipoise, d) Fluorinnert Liquid C_8F_{18} with surface tension of 15 dyne/cm. was used to obtain a wider surface tension range. Throughout the investigation the temperature of the injectants was kept roughly at 20°C. in the plenum chamber. The wind tunnel facility did not have provisions to heat the flow, so all tests were performed at ambient air stagnation temperature. The heat transfer between the injectant and the crossflow was assumed negligible.

The parameters which were varied to determine their effects on breakup and atomization were: a) injectant viscosity (μ = 1.0, 10.5, 18.4, 27.6, 40.5, 59.8 centipoise), b) injectant surface tension (σ = 73.0, 33.5, 15 dyne/cm.), c) injection rate ($\bar{q}$ = 1-20), d) injector diameter (d = 0.45, 0.96, 1.5 mm.). Throughout the experiment the

freestream stagnation pressure was kept at 4.2 atm $\pm$ 2%.

The test program and the analysis of the data were designed in such a way as to study the effects of injectant physical properties on surface wave formation, breakup and atomization processes, surface wave and liquid clump propagation velocities, and the resultant spray fineness for crossflow injections of liquids in Mach 3 airstream.

II. EXPERIMENTAL APPARATUS

2.1 Test Facility

The current study was conducted in the Virginia Tech 23 cm. x 23 cm. supersonic wind tunnel. This tunnel is a blow-down type with interchangeable test sections capable of producing freestream Mach numbers of 0.4 to 4.0. In the current investigation, the test section was chosen to produce a freestream Mach number of 3.0. A series of calibration investigations have confirmed the uniformity of the flow in the test section. Throughout the experimental work, the stagnation temperature of the freestream was that of the ambient air (roughly 20°C). The stagnation pressure was controlled at 4.2 atm. $\pm$ 2%. Large thick glass windows normally cover the sides of the test section. These windows were of good schlieren quality and were used in the direct photographic work. However, they were found to be of insufficient quality for light scattering and were replaced for that work.

2.2 Flat Plate Model

The liquid injection was carried out through a flat plate model with a sharp leading edge, Fig. 4'. The flat plate had dimensions of 15.2 cm x 25.4 cm, with the orifice of the injection located 5.1 cm downstream of the leading edge. The model was mounted on a wedge-shaped base which in turn was mounted to the bottom surface of the test section. Three circular injectors, with orifice diameters of 0.45, 0.96 and 1.5 mm were used. The discharge coefficients of the injectors were assumed to be unity. Each injector had a 1.3 cm straight run. All injectors were made of brass and were interchangeable from

beneath the flat plate. A 2.5 cm I.D. plenum chamber was fitted to the flat plate underneath the injector and sealed with a rubber O-ring. A copper constant thermocouple was mounted inside the plenum chamber to record the injectant temperature. The large size of the plenum chamber compared to the size of the injector reduced any disturbances in the injectant. Liquid injectant was supplied to the plenum chamber by a 0.95 cm O.D. copper tubing. Injection through a flat plate was chosen over the injection through the test section walls, to reduce the boundary layer thickness and its effects on the liquid jet.

2.3 Injection System

A schematic diagram of the injection apparatus is shown in Fig. 5. A large stainless steel tank which was utilized as the injectant reservoir was pressurized by nitrogen gas. The size of the tank played an important role in maintaining a constant injection pressure in the plenum chamber during each run, because the volume of the fluid injected during each run was small compared to the total volume of the injectant stored in the tank. The reservoir pressure was regulated to attain the desired mass flow rates through the injector.

The pressurized injectant passed through a solenoid valve which was remotely operated to start and stop the flow. The solenoid valve was followed by a needle valve which regulated the mass flow rate of the injectant. The needle valve was connected in series to a manual valve as a safety precaution, so that if the solenoid valve failed the flow of injectant could be stopped. This valve was followed by a filter which was capable of removing foreign materials larger than 140

microns from the injectant. The filter led to a Brooks Rotameter flat-type flowmeter which measured the mass flow rate of the injectant. Copper tubing of 12.7 cm O.D. was used for this series of connections. Beyond the flowmeter, the size of the tubing was reduced to 0.95 cm C.D. in order to make the connection with the model plenum chamber. The pressure and temperature of the injectant inside the plenum chamber were measured by a pressure transducer and a thermocouple to insure that there were no fluctuations in the chamber during each run.

2.4 Flow Instrumentation

The stagnation pressure and temperature of the free-stream were measured in the settling chamber of the supersonic tunnel. All the outputs of the transducers and the thermocouples were recorded on strip chart recorders during each run. The flowmeter was calibrated for each injectant separately and was directly read during each run.

List of Instruments and Specifications

1) freestream pressure transducer;
   Frederic Flader, Engineering Physics Division,
   Range of 0-100 psi (no model number),
2) model plenum chamber pressure transducer;
   Statham Model 4-326, 0-1000 psi,
3) solenoid valve;
   ASCO Model 8266C1, 400 pdi max.,
4) filter;
   NUPRO Model B6TF2-60, 140 micron,

5) flowmeter;

Brooks Rotameter Float Type, 3.0 GPM,

6) recorders;

Hewlett Packard Model 7100

III. PHOTOGRAPHIC EQUIPMENT

3.1 Still Photography

Two types of still photography were used - stop action (Fig. 6) and streak type (Fig. 7). In the stop action photography, a Xenon model 437A Nanolamp capable of producing a very short duration spark ($t=9x10^{-9}$ sec.) was utilized as the light source. Magnification of the jet in the crossflow was provided by a 20.2 cm. focal length, f/2.5 lens. The camera in this set-up was a simple bellow box capable of holding a Polaroid film holder. The shutter on the camera was left on the open position since the Nanolamp spark acted as the shutter. However, this procedure required the laboratory to be in total darkness while the film was exposed. Polaroid Type 57, ASA, 3000 speed, sheet film was used. In order to verify the magnification factor and the sharpness of the photographic arrangement, a ball bearing of known size was placed in the longitudinal plane of the jet and a picture was taken. The magnification factor was set to 3.9:1 for the majority of the tests and was checked each time the system had to be altered. This arrangement provided sufficiently short time of exposure and adequate resolution to give sharp, blur-free pictures of the jet. With considerable adjustment, proper light intensity and the added advantage of the Nanolamp being a point source, very sensitive photographs were developed. As a result, the bow shaped shock, the boundary layer and at times the weaker secondary shocks were photographed.

The jet penetration depth into the crossflow was obtained from streak type shadowgraph pictures. The bellow box camera was employed

and the shutter speed was set to 10^{-3} sec. The lighting arrangement was changed to a P.E.K. model 910 L.H. continuous mercury arc lamp. The lens was replaced by a 198.3 cm. focal length parabolic mirror and the magnification factor was set to 1:1. This procedure resulted in a time-averaged or integrated picture of the unsteady jet in the crossflow.

3.2 Multi-exposure Photography

3.2.1 Rotating Mirror Camera

In order to study the velocity of the disturbance on the jet column and the speed of the clumps in the plume, a sequence of several pictures is necessary. A multi-exposure photographic technique using an AVCO Type MC 300 Model 2 rotating mirror camera as the framing device was used. The camera is a continuous writing streak type, utilizing a hexagonal mirror driven by an air turbine which is capable of speeds up to 3000 RPS. This is equivalent to a writing speed of 3.8 mm. per microsecond on a stationary film. A photograph of the camera is shown in Fig. 8 and the schematic of the set-up is shown in Fig. 9. By mounting the camera with the mirror axis vertical and using separate sparks as light sources, the camera was converted to a framing device rather than a streak camera. The camera's film holder was modified to accept a Polaroid Type 57 film and the distance between the mirror and the film was lengthened to increase magnification factor.

The timing for the spark triggering was accomplished by a Transistor Transistor Logic (TTL) electronic circuit designed and built at Virginia Tech, Fig. 10. The triggering circuit had the capability

of firing up to eight strobe flash units with virtually unlimited time delay variations. The initial input to the system was provided by a magnetic pick-up mounted on the rotating mirror for the purpose of rotational speed measurements. When the magnetic pick-up was in position to trigger a counting pulse, the mirror was in a given orientation relative to the film. A certain time delay before the first spark was required to allow proper mirror alignment with the film sheet as shown in Fig. 11. Of course, the duration of the time delay was dependent on the rotational speed of the camera mirror. A Beckman model 310 measured frequency of the rotation and its digital read-out displayed the number of RPS directly. When the mirror was properly aligned with the film sheet, a sequence of eight pulses with fixed time spacing between them was generated to trigger the strobe flash units. To ensure the accuracy of the time delay between each flash a photomultiplier was used to "see" the sparks. The output from the photomultiplier was directed to an oscilloscope. The oscilloscope was set to a single external trigger, memory sweep. This resulted in a clear picture of the time space between each flash. The light sources were General Radio Strobotac strobe flash units, producing flashes of 8×10^{-7} sec. duration. To illuminate the same geometric space in the test section with each flash, it was necessary to place the light sources next to each other with the spark tubes as close as possible. Other arrangements such as placement of the light sources at 90° angles apart with the use of a beam splitter resulted in pictures of varying intensity, therefore contributing to the loss of information. The rapid rotational

rate of the camera's mirror and the controlled time delay of 10^{-5} sec. between each flash resulted in two separate pictures of the spray plume on the same film sheet. This corresponds to 100,000 picture frames per second, which is considerably faster than the maximum framing speed of a high speed movie camera. The photograph associated with this technique revealed interesting information about the disturbance velocities on the jet surface. However due to the small magnification there was also some loss of information. For this reason another multi-exposure technique was developed.

3.2.2 Multi-Exposure Photography (fixed mirror)

To extract additional and more accurate information from multi-exposure photographs, larger magnified images are necessary. The rotating mirror camera was only capable of accepting one Polaroid film sheet at a time and a sequence of only two images could be recorded on the same film sheet. Therefore, the size of the images at best were equal to the actual size of the spray plume in the crossflow. Also, because of the limitations in the rotational speed of the mirror, the shortest attainable time space between each flash was about 10^{-5} sec. Another technique for recording the two images became necessary and was developed. Fig. 12 is the schematic of the new system. This system consisted of two General Radio Strobotac strobe flash units as the light sources, a 20.2 cm. focal length f/2.5 lens, a stationary mirror and two bellow box cameras. Because two cameras and two film sheets were employed, it was possible to record a sequence of two highly magnified (3:1) images, each on a separate film sheet. The same (TTL)

triggering circuit generated the pulses necessary to trigger the flash units. However, due to the lack of moving parts the synchronization procedure was eliminated. Also, it was possible to reduce the pulse spacing to 3×10^{-6} sec. corresponding to 330,000 picture frames per second. The system had the disadvantage of being more costly to operate, two film sheets instead of just one necessary for the rotating mirror camera. Also, the proper optical alignment of the system and the consequent data reduction became much more laborious.

IV. THE DIFFRACTIVELY SCATTERED LIGHT TECHNIQUE

4.1 Theoretical Considerations

The mean droplet diameter measurements throughout the field of the jet spray were measured using the Diffractively Scattered Light Method (DSLM). This method was selected over potentially more accurate methods based on short duration microphotographs because of the many practical difficulties associated with those techniques; 1) the difficulties related to sufficient resolution; 2) the small depth of focus required; 3) the small number of particles usually present within the focal plane and the question of whether these particles constitute a representative statistical sample; 4) the differentiation between film grain and droplet images; 5) the problem of deciding between single droplets or the clumps; and 6) perhaps the most important, the very tedious process of counting and measuring the droplet sizes one by one. The same difficulties apply to the use of short-duration Holograms. More elaborate methods based on scattered light were not adopted, because a method simple and reliable enough for routine use over a study involving many individual tests was required.

The investigation of the DSLM was first conducted by Chin, Sliepeevich, and Tribus (32), using a theory by Gumprecht and Sliepeevich (33), which describes the scattering properties of a polydispersion. This theory requires very low droplet concentrations to constitute a small optical depth. It further requires the particle size and refractive index fall within given intervals. The formation of a theory for the scattering properties in the more general case of particles of

arbitrary size and arbitrary refractive index occuring in a polydispersion of finite optical depth has been discussed by Dobbins, Crocco and Glassman (34).

A distribution function $N_r(D)$ is defined in such a way that the integral of $N_r(D)$ over a given diameter interval represents the probability of occurrence of particles within the specified interval. This function determines the relative frequency of occurrence of particles of a given diameter, D. The expression for the intensity of scattering due to a polydispersion is normalized by dividing by the intensity of defractively scattered light in the forward direction (θ=0) centerline. The normalized integrated intensity of forward scattered light $I(\theta)$ due to a polydispersion of particles is given as

$$I\theta = \frac{\int_0^D [2J(\alpha\theta)]^2 N_r(D) D^4 dD}{\int_0^D [N_r(D) D^4] dD} \qquad (1)$$

Equation (1) represents a relationship for the angular distribution of scattered light in terms of the particle size distribution. A problem arises from the fact that one does not know what distribution function is a good representative of the particle sizes being investigated. Mugele and Evans (35) have shown that choosing the parameters in these distribution functions in such a manner as to fit a size histogram closely can predict a completely inaccurate volume fraction curve or give inaccurate values of the mean diameters. These shortcomings were solved by the use of Upper Limit Distribution Function (ULDF) proposed by Mugele and Evans. The ULDF has the property that no particles exist

at sizes larger than a specified D_{∞}. Roberts and Webb (36) studied the accuracy of the DSLM in measuring particle size with many different distribution functions. They concluded that the value of the volume/surface mean droplet diameter D_{32}, may be determined from the intensity of diffractively scattered light from a polydispersion of spherical particles to a good degree of accuracy for an extremely wide range of distributions without knowledge of the specific distribution type. They plotted the mean theoretical illumination profile for all distributions investigated as in Fig. 13. This profile can be regarded as a universal illumination profile and has been utilized in the current study in obtaining mean droplet diameter of particles.

4.2 Optical Arrangement

A schematic of the final optical set up is shown in Fig. 14. For ease of operation, all of the optical equipment, with the exception of the windows, were mounted on a homemade optical bench with two degrees of freedom (vertical, horizontal). A helium-neon laser was used as the light source. A spatial filter located directly in front of the light source produced a larger diameter and a more uniform light beam than that of the laser alone. Two circular high quality glass sections 5.1 cm. in diameter and 1.3 cm. thick were used as windows, one on each side of the test section. A plano-convex lens 5.1 cm. in diameter with a focal length of 50 cm. was used as the condensing lens. This lens focused the unscattered light beam on an aperture of 0.15 mm. diameter located directly in front of a photomultiplier tube. The photomultiplier assembly housed in a 7.6 cm. diameter pipe 20.3 cm. in length,

consisted of the photomultiplier tube, its circuitry and the 0.15 mm. aperture. The aperture plate was located 0.6 cm. in front of the photomultiplier tube and it completely sealed the tube inside the assembly. The photomultiplier assembly was mounted on a traverse mechanism which allowed a smooth and constant speed scanning of the scattered light illumination profile intensity. The illumination profile intensity versus the scattered angle, θ, must be obtained in Fig. 15. The travel distance of the photomultiplier tube was recorded by employing a twenty turn potentiometer. The final arrangement and selection of the optical components came only after a long and trying series of tests. Since the output signal of the photomultiplier varied greatly in magnitude, it was processed through a logarithmic amplifier built at Virginia Tech which made it easier to record accurately. This also greatly facilitated the required extrapolation to the θ=0 value (Fig. 15).

The accuracy of the experimental implementation of the DSLM in obtaining the mean diameter of particles was investigated in three separate cases. These three cases were selected to be representative of the actual experimental conditions. First, the mean droplet diameter of water particles produced by an atomizer was measured by both a direct microphotographic technique and the Diffractively Scattered Light Method. In measuring the particle diameter of the atomizer spray, the optical set-up was the exact set-up used in the supersonic injection investigation, however, the experimental conditions were different. The atomizer discharged the water particles into still air as compared to the injection into supersonic airstream for the main test program. The

particle sizes produced by the atomizer were also measured by the microphotographs and the results were compared to the mean droplet diameter obtained by light scattering technique. The results were in good agreement. The photographs revealed an average droplet diameter of 24.6 microns and the DSLM showed a mean droplet diameter of 26 microns. This amounts to an error of 5.4% which was within our experimental expectations. Second, using the same optical set-up, the mean diameter of known-sized glass beads were measured. The bead diameter size range was from 48-53 microns. The different diameter sizes were necessary to assure polydispersion scattering of the light as required by the theory. The DSLM measured a mean diameter of 48 microns which is again within 5% accuracy of the true average diameter. To substantiate the accuracy of DSLM even further, a high magnification (40-50) microphotographic technique was set up to photograph a few droplets in Mach 3 airstream. The experimental conditions were matched to conditions under which DSLM was used. Fig. 16 is a representative photograph of the droplets in the crossflow. These highly magnified photographs reveal that the droplets are spherical in shape, thereby supporting the necessary assumption of polydispersion of light by spherical particles associated with DSLM. Droplet diameter measurement from these photographs (18 microns) again confirm the accuracy of the DSLM in measuring mean droplet diameter (16 microns) under the adverse conditions of a blow down type supersonic wind tunnel.

List of Optical Equipment

1. Laser: Spectra physics Model 120 Helium-Neon 5M Watts

2. Spatial Filter: JODON Model BET-25 beam expanding laser collimater

   a) Lpsf-100 Spatial filter consisting of 5X, 10X, 20X, 25X, microscope objective and 15, 20, 25, 50, 100 micron pinhole

   b) CL-25 27mm diffraction limited telescopic lens

3. Windows: ORIEL Model A-43-564-80 precision flat windows (2) of Schlieren-free fused silica 2 in. diameter
   0.5 in. thickness
   1 sec. parallelism with surface profile for research grade, optical polish for low light scatter.

4. Photomultiplier tube: RCA Model C7164R

5. DC power supply: ORTACE Model 456H)0-3k) DC voltage (supplier for photomultiplier tube only)

V. TEST PROCEDURE

Injectants with different viscosities and surface tension were prepared and injected over a wide range of jet/freestream dynamic pressure ratios. The penetration and instantaneous structure of the jet in the crossflow were studied by employing still photographic techniques. The wave speed, disturbance propagation and the clump velocities were measured utilizing a multi-exposure photographic technique. Also, the mean droplet diameter of the particles along and across the jet plume was measured by the light scattering technique as illustrated in Fig. 17 .

5.1 Still Photographic Procedure

In the stop action and streak type photography, different light sources were used. However, the experimental procedure associated with the two was similar. For all tests, the tunnel stagnation pressure and temperature, and the injectant pressure and temperature were measured and recorded on strip chart recorders. The injectant mass flow rate was visually determined by observation of the flowmeter. The flowmeter was calibrated separately for each of the injectants. Through considerable adjustments, the tunnel was made to operate with a constant and repeatable stagnation pressure for each run. The test procedure for stop action photography was as follows:

1) the camera shutter was left open;
2) the film was set in the Polaroid film holder;
3) the laboratory was completely darkened;

4) the film was exposed;

5) the strip charts and the tunnel were started;

6) after supersonic flow was established in the test section, the injectant was started;

7) at the desired mass flow rate of injection, the Nanolamp was triggered to spark and the event was marked electronically on all the strip charts;

8) the injectant, the tunnel and the strip charts were turned off;

9) the film was covered;

10) the laboratory lights were turned on.

The test duration ranged from 7-11 seconds.

For the streak type photographs, the light source was changed to a continuous mercury arc lamp and the camera shutter speed was set to 10^{-3} sec. Since the camera shutter was closed, it was possible to expose the film with the laboratory lights left on. The test procedure was completely automated by utilizing a timer. The timer sequence was as follows:

1) the tunnel and the strip charts were started;

2) after 4 seconds the injectant was turned on;

3) the laboratory lights were turned off;

4) the shutter was triggered and the electronic markers on the strip charts recorded the event;

5) the injectant was shut down;

6) the tunnel and the strip charts were turned off;

7) the laboratory lights were turned on.

5.2 Multi-Exposure Photographic Procedure

Multi-exposure photography required the operation of the rotating mirror camera at a rapid and steady rotational speed. The time necessary for the camera to reach a steady state was between 20 and 30 seconds. The test procedure was as follows:

1) after the camera had reached a steady rotational speed, the laboratory was completely darkened and the Polaroid film was exposed;
2) the strip charts and the wind tunnel were started;
3) when supersonic flow was established, the process of liquid injection was carried through;
4) at desired the mass flow rate of injection, the light sources and the event markers on the strip charts were triggered;
5) the injection, the strip charts, the tunnel and the air supply to the camera were turned off;
6) the film was covered;
7) the laboratory lights were turned back on.

The total duration of the procedure was between 40-50 seconds, including the tunnel run time of 8-12 seconds.

5.3 Diffractively Light Scattered Method Procedure

To measure the mean droplet diameter resulting from the atomization of the jet in the supersonic crossflow accurately, separate test runs without injection were conducted to determine the background scattering of the light by the optical equipment including the windows and the supersonic flow. Theoretically, there should be no scattering

of the light by the optical equipment and the air flow. However, there was a slight diffraction caused by the optical equipment and random particles in supersonic flow, which resulted in a very low intensity scattering profile, Fig. 15 . Once the null condition scattering was established to be satisfactory, injection runs were made and the intensity of the illumination profile vs. the angle of scattering was recorded. It was found unnecessary to subtract the null condition intensity from the intensity of the injected runs. This was an improvement over the procedure (40), which reduced the number of runs necessary to obtain droplet diameter by almost 50%. However, a random check of the null conditions was still necessary to ensure accurate measurements. The test procedure was as follows:

1) the laser and the photomultiplier tube were energized and were allowed to reach a steady state;
2) the laboratory was completely darkened;
3) the uniformity of the light beam produced by the spatial filter was checked;
4) the tunnel, the injection (when used) and the recorders were switched on, after the supersonic flow had started, the photomultiplier tube on the traverse scanned the illumination profile intensity of the scattered light;
5) in the case of an injection run, the injection was turned off after completion of the scan;
6) the tunnel was shut down;
7) the recorders were turned off and the laboratory lights were turned on.

The duration of each run was between 7-10 seconds and the time necessary for the scan of the illumination profile was 5 seconds. The location of the light beam with respect to penetration height and injector port was then changed, and the test procedure was repeated.

VI. RESULTS AND CONCLUSION

6.1 Overview

The behavior of a liquid jet in a high speed crossflow is highly unsteady, random and rapid. A complete and detailed understanding of the problem requires a large amount of quantitative and qualitative information. The aerodynamic forces deform and bend the liquid jet in the down stream direction, creating a three-dimensional body in the flow field. Large amplitude waves of high frequency form on the surface of the jet, which play an important role in the unsteady behavior of the jet. These waves propagate downstream along the surface of the jet, and thus grow in wavelength and amplitude. The process of wave growth is found to be the dominant mechanism for break-up and decomposition of the jet for the cases of moderate viscosity and surface tension injectants ("moderate" is defined as of the order found for water at STP). The jet break-up starts with a cross fracture of the jet column at a trough between two waves. This critical development is similar to the Rayleigh problem, however, the cause of fracture and the nature of the waves leading to the cross fracture are different. The processes of cross fracture and atomization divide the jet plume into three regions observable on Fig. 18 : 1) the cohesive jet body which is that section of the jet plume between the injector surface and the first cross fracture, 2) the region of the separated liquid clumps, which starts after the first cross fracture and contains only large clumps of liquid (this region is referred to as the spray formation zone) and 3) the atomized region, which is the area that contains

atomized spherical particles. The cohesive jet body is usually the largest segment of the jet. The surface deformities and disturbances on the cohesive jet range from small capillary waves to large aerodynamically induced waves. There are usually three separate sub-regions on the cohesive jet column: 1) the coherent, disturbance-free jet column right after the injector, 2) the zone of small capillary waves on the jet column, which starts just after the coherent jet column and 3) the large wave zone. The waves in this zone are mostly aerodynamically induced, and they grow in wavelength and amplitude to the point of first cross fracture.

The parameter $\bar{q}$ ($\equiv \rho_j V_j^2 / \rho_\infty V_\infty^2$) was used as a primary reference in all tests. This parameter principally determines the overall shape of the jet and also effects other jet characteristics. For given free-stream conditions, varying $\bar{q}$ implies varying mass flow rates, velocity, Reynolds number and pressure. The study of the behavior of the jet in the supersonic crossflow led to division of the range of $\bar{q}$ into 3 regimes; low, medium and high. The principal idea was taken from the work of Kush and Schetz (3,4). But, the ranges of the present regimes are different from the values reported in their work.

Regime 1 corresponds to injection at $\bar{q} \approx 2$. An example is shown in Fig. 19. Transverse injection in this regime results in a very low penetration spray plume. Because of the small penetration injection in this regime is not suitable for fuel injection applications. However, due to the large liquid surface layer formation and the interaction of the jet with the injector surface, it can be used for surface cooling.

Regime 2 corresponds to injection of liquids with $\bar{q}$ ranging between 4 and 12. A typical case is given in Fig. 20. The jet has sufficient momentum to penetrate quite far into the crossflow. Therefore, it is suitable for fuel injection applications. Regime 3 corresponds to injection at $\bar{q}$ 12 up to 20 Fig. 21. The jet penetration is the largest. To attain the high pressures and mass flow rates necessary for injection in this regime, large, heavy pumps would be required, which prohibit fuel injection application of this regime.

6.2 Effects of Viscosity and Surface Tension on the Atomization Process

To study the effects of physical properties on the break-up and atomization of the spray plume in the crossflow, injectants with various combinations viscosity and surface tension were injected through a circular injector (d=0.96 mm.) at three values of the jet to freestream dynamic pressure ratio, $\bar{q}$ = 2, 8 and 14. Table I shows that addition of glycerine or enthonol to water substantially changes the viscosity or the surface tension of the solution, while insignificantly effecting the liquid density. Also, for injection at a specific value of $\bar{q}$, jet velocity remains virtually the same for all injectants. Therefore, with the exception of the Fluorinert liquid (due to its larger density) the changes in injection Reynolds and Weber numbers are mainly due to the changes in viscosity and surface tension of the liquid injectants.

6.2.1 Low $\bar{q}$, Regime 1 (q=2)

Fig. (22a) shows the atomization processes associated with a water jet plume (Re_j = 16.8 x 10^3, We = 4.0 x 10^3, μ = 1.0C.P., σ = 73.0 dyne/cm.). The cohesive jet body, the point of first cross fracture, the region of spray formation and the atomized regions are clearly evident. The cohesive jet body is the largest liquid clump in the flow field. The wave pattern on the jet column consists of two large waves extending from the injector surface to the point of first cross fracture. Superimposed on the large waves, there are small capillary waves. The cohesive jet column has a very short coherent length near the injector. The spray formation zone right after the fracture consists of several irregularly shaped large clumps accompanied by large liquid particles. The clumps are accelerated downstream, and they further break-up into smaller particles. The region of finely atomized particles seems to be near the top of the spray plume. The liquid layer on the flat plate is extensive. The atomization processes are clearly due to surface wave growth and cross fracture of the jet leading to clump formation and finally droplets.

Fig. (22b) shows the atomization processes associated with a water/glycerine jet plume (Re_j = 1.7 x 10^3, We = 3.9 x 10^3, μ = 10.6 C.P., σ = 73.0 dyne/cm.). The jet cohesive body is clearly visible in the photograph. The wave pattern on the jet column consists of only large wavelength waves. No capillary waves are visible. The coherent jet column has a longer length than for the case of the water spray plume. The point of first cross fracture is clearly observable on the photograph. The region of spray formation is quite large and

consists of many irregularly shaped clumps. These clumps have been reduced in size at downstream locations of the spray formation zone. The beginnings of the atomized region is also photographed. It can be deduced that jet decomposition is primarily due to wave formation and wave growth leading to jet cross fracture. However, some ligament formation has started which can easily be seen. Sections of the jet have been stripped of and carried to higher penetrations than the main jet. Also, because of small penetration depth, there is extensive liquid formation on the flat plate.

Fig. (22c) is a photograph of a more viscous water/glycerine jet spray ($Re_j = 9.7 \times 10^{-3}$, $We = 3.8 \times 10^3$, $\mu = 18.4$ C.P., $\sigma = 73.0$ dyne/cm.). The cohesive jet body is very large and the point of first cross fracture is not easily distinguishable. The waves on the cohesive jet body are mainly large, with few capillary waves present. The zone of spray formation consists mainly of elongated, irregularly shaped clumps. The completely atomized zone lies outside of the field of photograph. The droplets and the liquid particles between the jet plume and the flat plate are large in size. The process of ligament formation is more pronounced. The ligaments have increased both in length and diameter. As before, sections of the jet have been separated and penetrated the crossflow higher than the main jet. The atomization process is divided between wave formation and ligament shedding.

Fig. (22d) is a photograph of a thicker water/glycerine jet ($Re = 6.5 \times 10^3$, $we = 3.940 \times 10^3$, $\mu = 27.6$ C.P., $\sigma = 73.0$ dyne/cm.). The cohesive jet body has an irregular shape. The waves on the leading edge of the plume have been reduced in amplitude. The spray formation

zone consists only of large ligaments, and it is densely populated. The atomization processes are slow, thus the atomized region does not form within the frame of the photograph. A segment of the jet has separated from the main jet body and has penetrated the crossflow higher than the main jet body. Ligament formation has become the primary mechanism for jet break-up and atomization. The space between the flat-plate and the main jet is filled with ligaments and large spherical particles.

Fig. (22e) is a photograph of still more viscous water/glycerine jet plume ($Re_j = 4.3 \times 10^3$, $We = 3.8 \times 10^3$, $\mu = 40.5$ C.P., $\sigma = 73.0$ dyne/cm). The cohesive jet body is well defined and column-like but bent over in the downstream direction. The waves on the body are few and of small amplitude. The coherent length of the jet column is long. The cohesive jet body divides into three large ligaments at its end. The spray formation zone is well defined and is quite long. The atomization procedure has slowed further and not within the field of the photograph. Again, a segment of the jet has been stripped to higher penetration and has been atomized into fine droplets. Ligament formation is responsible for jet break-up and atomization.

Fig. (22f) shows the most viscous water/glycerine jet spray tested ($Re = 0.3 \times 10^3$, $We = 3.810 \times 10^3$, $\mu = 59.8$ C.P., $\sigma = 73.0$ dyne/cm.). The cohesive jet body and the point of first cross fracture are clearly shown. The cohesive jet body shows a long, coherent, disturbance free column starting at the injector surface. Large ligaments are present in the spray field. The photograph shows that the spray formation zone is large. There is no evidence of the atomized regions

in the photograph. The spray field totally consists of large ligaments. Segments of the jet have penetrated the crossflow deeper and have been atomized to fine droplets. Jet break-up and atomization is due only to ligament shedding.

Fig. (22g) is a photograph of the low surface tension water/alcohol jet plume (Re_j = 15.3 x 10^3, We = 8.6 x 10^3, μ = 1.0 C.P., σ = 33.5 dyne/cm.). The cohesive jet body is large and has spread to several times its base diameter. There is only a slight capillary wave formation. Due to the rapid rate of jet atomization, the point of first cross fracture is not clearly visible. The spray plume rapidly disintegrates into fine particles. The region of spray formation is composed of many clumps which in a short distance atomize to fine droplets. The fully atomized region is very quickly reached, and it is within the view field of the photograph. The particles are small in size, and they are distributed throughout the field of spray plume. The wave generation phenomenon is the main mechanism of jet decomposition, there are no ligaments in the field of spray.

Fig. (22h) is a photograph of the very low surface tension Fluorinert liquid jet spray (Re_j = 14.8 x 10^3, We_j = 2.7 x 10^4, σ = 15 dyne/cm., μ = 1.5 C.P.). The cohesive jet body, the point of first cross fracture, spray formation zone and the region atomized particles are indistinguishable. There are large waves present on the leading edge of the spray plume. The atomization is rapid and complete, so that the total spray field between the flat plate to the top of the spray plume appears dark and solid on the photograph. The droplet formation seems to start immediately from all sides and the underbody

of the jet. It is obvious that lower surface tension injectant rapidly disintegrates and atomizes without generating the spray formation transition zone.

6.2.2 Medium $\bar{q}$, Regime 2($\bar{q}$ = 8)

Fig. (23a) is a photograph of a water spray plume (Re = 33.8 x 10^3, We = 16.1 x 10^3, μ = 1.0 C.P., σ = 73.0 dyne/cm.). The spray plume has a larger penetration than the Regime 1 case. The jet cohesive body shows two separate zones: 1) the zone of small capillary waves on the jet column and 2) the zone of large aerodynamically induced waves. The aerodynamically induced waves grow in wavelength and amplitude to the point of first cross fracture, while the capillary waves stay superimposed on these larger waves. The cohesive jet body rapidly spreads to several times its base diameter in a very short axial distance along the jet. The spray formation zone contains large liquid clumps. The immediate beginning of the atomized region is also observable. Due to the large penetration of the jet, there is an open space between the flat plate and the main jet body. This space is filled with fine spherical particles which have resulted from jet decomposition. A close examination of the cohesive jet body indicates bands of denser (darker) areas. These bands suggest the fact that waves are wrapped around the cohesive jet body. The boundary layer formed on the flat plate is also observable. Wave generation and growth is the jet decomposition mechanism.

Fig. (23b) shows the atomization processes associated with water/glycerine jet spray (Re_j = 3.4 x 10^3, We_j = 13.8 x 10^3, μ = 10.5 C.P.,

σ = 73.0 dyne/cm.). The spray plume, the bow shaped shock in front of the spray plume and the boundary layer on the flat plate are well defined. The cohesive jet body shows the three zones of the coherent column, small capillary waves, and the large aerodynamically induced waves. The coherent column is rather lengthy, and its diameter stays nearly constant throughout its length. The capillary wave section has a short axial length. The jet column starts to spread and increase in diameter with increasing distance in the axial direction. Waves of small wavelength and large amplitude cover the initial portion of the aerodynamically induced wave zone, and their wavelength increases with increasing axial distance. The point of first cross fracture is easily seen. The region of spray formation consists of densely populated clumps. The space between the jet main body and the flat plate is filled with spherical droplets. A close examination of the under side of the jet suggests that some ligament formation has started. The majority of the ligaments are sheared from the coherent and small capillary wave zones of the jet column. The ligaments are thin and short and rapidly form into droplets. The main mechanism for jet decomposition is still wave growth and cross fracture.

Fig. (23c) is a photograph of a thicker water/glycerine plume (Re_j = 1.837 x 10^3, We_j = 15.3 x 10^3, μ = 18.4 C.P., σ = 73.0 dyne/cm.). The three zones of the cohesive jet column are clearly shown. The capillary section has a larger length, and the waves grow in wavelength and amplitude to the point of first cross fracture. The jet cohesive body is quite large and spreads to several times its base diameter. The region of spray formation consists of densely populated clumps and

ligaments. The underside of the jet near the injector surface consists of ligaments that break-up into droplets further downstream. The space between the main jet and flat plate is filled with large spherical droplets. The unsteadiness of the jet on the top surface is greater than in the previous case. This is evident from the fact that segments of the jet have crossed the main bow shock in the upstream direction. The photograph suggests that the decomposition mechanism is mainly due to wave generation and growth. However, this is accompanied by significant ligament formation from the jet column near the injector surface.

The atomization mechanisms of a still more viscous water/glycerine jet ($Re_j = 1.3 \times 10^3$, $We = 15.7 \times 10^3$, $\mu = 27.6$ C.P., $\sigma = 73.0$ dyne/cm.) is shown in Fig. (23d). The large aerodynamically induced waves grow in wavelength and amplitude to the point of first cross fracture. The main jet body spreads out, but less than before. Large amounts of liquid have been stripped from the top surface of the jet body and have been atomized into fine particles. The spray formation zone consists of several large liquid clumps which are irregularly shaped. The space between the jet and the flat plate consists of ligaments near the jet body and large spherical particles away from the main jet. The majority of the ligaments are sheared from the coherent and capillary wave regions of the jet column. The main jet body decreases in diameter at large axial distance from the injector port. It can be said that the main jet body behaves like a massive ligament in the crossflow. The atomization process is due to both wave growth and ligament shedding, which has increased substantially.

Fig. (23e) is a photograph of a yet higher viscosity water/glycerine spray plume (Re_j = 0.8 x 10^3, We = 15.4 x 10^3, μ = 40.5 C.P., σ = 73.0 dyne/cm.). The process of atomization and jet decomposition has changed. The cross diameter of the spray plume remains virtually constant. The jet behaves as a very long, thick ligament while continuously shedding smaller sub-ligaments into the crossflow. The cohesive jet body clearly exhibits the coherent, the capillary wave and the aerodynamically induced wave zones. The large waves of the aerodynamically induced wave zone, show an inconsistent wave pattern, and thus have lesser wavelength and amplitude than the cases of lower viscosity spray plume. The point of first fracture is easily distinguishable. Again, there are particles above the main spray plume at higher penetrations which have atomized to fine droplets. The coherent and the capillary wave zone of the cohesive jet body are responsible for extensive ligament shedding. The large wave zone also sheds ligaments, however their length is much shorter and they rapidly break-up into spherical particles. The space between the main jet body and the flat plate is at first sparsely populated with liquid particles. As the main jet is approached, the particle concentration increases. The beginning of the spray formation zone is in the view field of the photograph. This area consists of large ligaments. The photograph clearly establishes that the atomization process is now due to ligament shedding. There are no spherical particles and the time and scale necessary for complete atomization has greatly increased.

Fig. (23f) is a photograph of the most viscous water/glycerine spray plume tested (Re_j = 0.6 x 10^3, We_j = 15.4 x 10^3, μ = 59.8 C.P.,

σ = 73.0 dyne/cm.). The spray field is nearly the same as the previous photograph. The coherent length is long, the capillary wave zone is well defined and the aerodynamically induced waves are small and disorganized. It is noted that the waves tend to curl toward the upstream direction (counterclockwise) thus creating an upstream surface upon which the pressure forces can act. When the upstream surface area of the wave is large and correctly oriented with respect to the freestream, the pressure forces acting on these areas become of sufficient magnitude to overcome the surface tension forces holding the jet together. However, for the cases of high viscosity injectants this does not result in a cross-fracture of the jet. At times a small segment of the liquid jet breaks away and penetrates higher in the crossflow than the rest of the plume. This process is clearly visible in the photograph of high viscosity spray plumes, regimes 1 and 2. The coherent and the capillary wave zones of the cohesive jet column are again responsible for the formation of large ligaments. The space between the flat plate and the jet body is populated with liquid clumps and ligaments near the jet body.

Fig. (23g) is a photograph of a low surface tension water/alcohol spray plume (Re_j = 32.8 x 10^3, We_j = 34.8 x 10^3, σ = 1.0 C.P., μ = 33.5 dyne/cm.). The atomization and break-up processes are very rapid, and they start immediately near the injector surface. The spray cross diameter becomes several times the jet column diameter at only a small axial distance in the crossflow. The coherent zone on the jet cohesive body has vanished. The capillary waves first grow into large amplitude waves, then increase in wavelength and finally result in the cross

fracture of the jet. The space between the flat plate and the spray plume is filled with droplets which increase in concentration as the jet body is approached. There is no evidence of higher penetrating clumps on the windward edge of the plume. The break-up mechanism is due to wave generation and cross fracture. However, due to low surface tension of the injectant, jet disintegration is rapid and the resultant droplet diameters are smaller and more uniform.

Fig. (23h) is a photograph of the very low surface tension Fluorinert spray plume ($Re_j = 29.4 \times 10^3$, $We_j = 7.7 \times 10^4$, $\mu = 1.5$ C.P., $\sigma = 15$ dyne/cm.). The process of atomization and break-up is very rapid and complete. The atomization starts on the jet column immediately near the injector surface. The cohesive jet body disintegrates into fine droplets without establishing the spray formation zone, hence the jet does not exhibit the point of first cross fracture. The waves on the leading edge of the cohesive jet have large wavelength and amplitude. The capillary wave zone of the jet column has vanished. The field of spray everywhere above the flat plate is densely and uniformely populated with fine droplets. The break-up and atomization is due to wave formation and almost instantaneous disintegration rather than the cross fracture, clump formation and spray formation steps exhibited by higher surface tension liquid jets.

6.2.3 High $\bar{q}$, Regime 3 ($\bar{q} = 14$)

Fig. (24a) is a photograph of water spray plume ($Re_j = 44.7 \times 10^3$, $We_j = 28.3 \times 10^3$, $\mu = 1.0$ C.P., $\sigma = 730$ dyne/cm.). The bow shock, the spray plume and the flat plate with the boundary layer are clearly

observable. The cohesive jet body is the largest part of the jet in the photograph. The jet column near the injector part is circular and has not deformed. The two regions of capillary and large aerodynamically induced waves of the jet column are clearly distinguishable. The aerodynamically induced waves grow in wavelength and amplitude with axial distance from the injector port to the point of first cross fracture. The capillary waves continue and stay superimposed on these large waves. The jet cross diameter increases rapidly as it disintegrates into droplets. The spray formation zone just after the point of first cross fracture is evident. This region consists of large liquid clumps which further break up into droplets. The underside region between the flat plate and the main jet is composed of densely populated spherical droplets. A close examination of the photograph reveals the fact that the waves are three dimensional and are wrapped around the jet surface. It is clear that the jet decomposition process into droplets is very rapid. The mechanism responsible is wave generation and cross fracture.

Fig. (24b) is a photograph of a more viscous water/glycerine spray plume ($Re_j = 4.5 \times 10^3$, $We_j = 27.7 \times 10^3$, $\mu = 10.5$ C.P., $\sigma = 73.0$ dyne/cm.). The bow shock in front of the spray plume, and the boundary layer are clearly visible. The cohesive jet body is the only part of the spray plume photographed. The three regions of cohesive column, capillary waves and the aerodynamically induced waves are clearly distinguishable. As the axial distance along the jet increases, the jet is spread out and increases in diameter. This spreading of the jet plume is more pronounced in the large wave region. The large

aerodynamically induced waves increase in wavelength and amplitude as they move away from the injection port. The underside region of the jet consists of ligaments from the coherent and capillary wave regions of the jet column and droplets from the large wave region. The atomization mechanism is clearly due to wave generation. However, it is accompanied with small amounts of ligament formation.

Fig. (24c) is a photograph of a thicker water/glycerine spray plume (Re_j = 2.5 x 10^3, We_j = 26.9 x 10^3, μ = 18.4 C.P., σ 73 dyne/cm.). The bow shaped shock, the spray plume and the boundary layer area easily observable. The cohesive jet body is the only section of the spray plume photographed. The three regions of coherent column, capillary wave and large aerodynamically induced waves are present. The large waves grow in wavelength and amplitude as they move away from the injector port. The spray plume increases in diameter with increasing axial distance, and this is more pronounced at the large wave region. The study of the flat plate side of the spray plume reveals the fact that, ligaments are produced by the coherent column and capillary wave regions. These ligaments are short in length, and they quickly break-up into large diameter particles. The ligament formation reduces as the large wave region is approached. The particles formed from the jet decomposition are spherical and large. The break-up mechanism is still due to wave propagation and growth, accompanied by increasing amounts of ligament formation.

Fig. (24d) is a photograph of a higher viscosity water/glycerine spray plume (Re_j = 1.7 x 10^3, We = 27.5 x 10^3, μ = 27.6 C.P., σ = 73.0 dyne/cm.). The bow shaped shock, the spray plume, and the boundary on

the flat plate are clearly established. The cohesive jet body is the only part of the spray plume photographed. The three regions of coherent jet column, capillary wave region and the large aerodynamically induced waves are visible. The large aerodynamic waves start with large amplitude, then grow in wavelength. Large thick ligaments have sheared away from the coherent and the capillary wave regions. These ligaments quickly break-up and form droplets of large diameter. The underside of the large wave region is composed mainly of droplets. The process of wave growth and propagation to the point of first cross fracture has been reduced. The break-up mechanism is composed of both ligament shedding from the underside of the jet and wave growth on the leading edge of the plume.

Fig. (24e) is a photograph of a still more viscous water/glycerine spray plume ($Re_j = 1.165 \times 10^3$, $We = 26.9 \times 10^3$, $\mu = 40.5$ C.P., $\sigma = 73.0$ dyne/cm.). The spray plume behaves as a large thick ligament, while continuously shedding smaller ligaments into the cross flow. The three regions of coherent jet column, capillary wave and large waves are present. The jet column near the injector port has remained coherent on both sides (windward and leeward). As the axial distance increases, the downstream side of the jet coherent column starts to shed ligaments. These ligaments are long and thin. The process of ligament formation persists throughout the underside of the jet spray. As a result, the jet column has been reduced in diameter. It is also noted that the waves on the leading edge curl counterclockwise, and they are being continuously stripped away by the cross flow. The atomization process is incomplete in the photograph and is only due to

ligament formation.

Fig. (24f) is a photograph of the most viscous water/glycerine spray plume (Re_j = 0.8 x 10^3, We = 27.1 x 10^3, μ = 59.8 C.P., σ = 73.0 dyne/cm.). The cohesive jet body is the only part of the spray plume photographed. The regions of coherent column, small capillary waves and large aerodynamic waves are clearly visible. The jet column near the injector port is coherent and disturbance free on its entire circumference. At a small axial distance, the downstream side of the column starts to show the process of ligament shedding. The main jet body remains virtually constant in diameter throughout the field of spray. The windward long waves have large amplitude. At increasing axial distance, these disturbances are stripped to higher penetration, and the leading edge of the jet becomes smoother. The process of break-up and atomization is only due to ligament formation.

Fig. (24h) is a photograph of low surface tension water/alcohol spray plume (Re_j = 42.6 x 10^3, We = 58.8 x 10^3, μ = 1.0 C.P., σ = 33.3 dyne/cm.). The cohesive jet body and parts of the spray formation zone is photographed. The cohesive jet body consists of two sections - the capillary and the large wave region. The large waves grow both in wavelength and amplitude to the point of first cross fracture. The spray formation zone consists of large liquid clumps of irregular shape. The jet column retains its shape for a short distance into the crossflow. The underside region of the jet spray is composed of liquid droplets which decrease in density as the flat plate is approached. The atomization of the jet is very rapid and starts near the injector

port. Clearly, the main mechanism for the atomization is wave generation, growth and cross fracture of the jet.

Fig. (24g) is a photograph of the very low surface tension Fluorinert spray plume (Re_j = 39.3 x 10^3, We_j = 13.5 x 10^4, μ = 1.5 C.P., σ = 15 dyne/cm.). The atomization processes are rapid and complete in the field of the photograph. The space between the flat plate and the outer edge of the spray is filled with densely packed droplets. The jet column of the cohesive jet body exhibits a very short capillary zone and a rather long aerodynamically induced wave zone. The jet column spreads to several times its base diameter at a small axial distance from the injector port. Because of the extensive atomization, the photograph does not show the point of first cross fracture and spray formation. The break-up and atomization is due to wave formation and instantaneous droplet formation bypassing the spray formation zone.

An examination of the results reveals that increasing Reynolds and Weber numbers enhances the atomization processes. For cases of low viscosity (high Reynolds number) jets, the atomization processes are due to wave growth, wave propagation and ultimately cross fracture of the jet. As the viscosity of the injectant increases (Reynolds number decreases) ligament formation increases. At high viscosities of 40.0 centipoise or greater the atomization processes are slow and are only achieved by ligament formation. The field of spray consists of large ligaments which eventually form large droplets. Decreasing surface tension (increasing Weber number) does not change the atomization processes completely, however, the break-up and atomization becomes much more rapid and the resultant spray seems to be composed of

finer droplets. At first, it seems that Reynolds and Weber numbers are the controlling parameters and their effect on jet break-up and atomization can be easily established. However, one must note that these two non-dimensional parameters are also dependent on jet velocity, injectant density and injector diameter ($Re = \rho Vd/\mu$, $We = \rho V^2 d/\sigma$) which makes their effect on break-up processes more complex. For example, by decreasing the injectant surface tension one increases injection Weber number which results in a spray with faster atomization processes and finally in smaller droplet diameter. The same increase in Weber number can be achieved by increasing the injector diameter. This time however the atomization processes are retarded and the resultant spray has larger diameter particles. A similar argument holds true for the Reynolds number effects. Increasing jet diameter increases the Reynolds number, however the resultant spray atomizes at a much slower rate and the resultant spray particles are much larger in diameter compared to the case of small diameter, low viscosity (also higher Re) injection. Therefore viscosity and surface tension of the injectant have the primary effect on the jet break-up and atomization. A simple correlation of these processes to Reynolds and Weber numbers is not possible.

6.3 Effects of Viscosity and Surface Tension on Wavelength, wave amplitude and jet structure.

The effects of surface tension and viscosity on the jet structure and, in particular, on the wave formation phenomena of the large aerodynamically induced wave zone of the cohesive jet body for low to moderate viscosity liquid jets is tabulated in Tables (2-7). Each table consists of 7 columns $\bar{q}$, λ/d, α/d, λ/α, $N\lambda F$, L/d and TR/d. The

$\bar{q}$ entries are the values of the dynamic pressure ratios. The λ/d entries are the average non-dimensional values for wavelength of the surface waves. The entries of α/d column are the average non-dimensional values for the wave amplitude measured peak to peak. The λ/α values show the average values for the ratios of wavelength to wave amplitude of the waves. The values of the $N\lambda F$ column represents the number of waves from the start of the large wave zone of the cohesive jet body to the point of first cross fracture. The L/d column entries are the non-dimensional length of the coherent zone of the cohesive jet body. The TR/d column entries show the non-dimensional length of the capillary wave zone of the cohesive jet body.

Table (2) shows the variation in λ/d, α/d, λ/α, $N\lambda F$, L/d and TR/d data for the case of water injectant μ = 1.0 centipoise, σ = 73.0 dyne/cm. Due to the unsteady nature of the jet behavior in the cross-flow and few statistical realizations, the data at first appears to show mainly trends. However, a close examination of the data, neglecting the high and low extremes of the data points, permits solid conclusions to be made. The λ/d and α/d entries reveal that the wavelength and wave amplitude are independent of injection rate $\bar{q}$. Injection throughout the three regimes resulted in average non-dimensional wavelengths and amplitudes of 1.2 and 0.4 diameters respectively for the large aerodynamic wave zone. The λ/α entries average to 2.5. The entries of the $N\lambda F$ column are the number of waves formed on the cohesive jet body from the end of the capillary wave zone to the point of first cross fracture. Injection in regime 1 resulted in formation of 2 to 3 waves on the jet body. This process increased to 8 waves for

regime 2 injection and further increased to an average of 11 waves for injection in regime 3. All photographs showed that there was not a coherent, disturbance free jet column near the injector port. The capillary wave region varied in length from 1.3 diameters for regime 1 injection to 4.2 diameters for regime 2 injection and finally to a maximum of 6.8 diameters at $\bar{q} = 16$. Further increases of $\bar{q}$ decreased the length of the capillary wave zone.

Table 3 shows the variation in λ/d, α/d, λ/α, $N\lambda F$, L/d and TR/d for the case of a more viscous water/glycerine injectant μ = 10.5 centipoise, σ = 73.0 dyne/cm. The average non-dimensional wavelength has increased to 1.6 diameters which corresponds to a 16% increase when compared to the results in Table 2 (pure water, μ = 1.0 C.P., σ = 73.0 dyne/cm.). The wave amplitude averaged to 0.6 diameters which corresponds to a 33% increase over the results of Table 2. The coherent length on the cohesive jet body L/d increased from 0.5 diameter in regime 1 to a maximum of 4.0 diameters in regime 3 at $\bar{q} = 14$. Then it decreased to 3.0 diameters at $\bar{q} = 20$. The capillary wave zone of the cohesive jet body increases in length with increasing $\bar{q}$. It has a range of 1.4 diameters in regime 2 which increases to 3.3 diameters in regime 3. The trend is similar to the results of Table 2. The number of large aerodynamically induced waves on the cohesive jet body ranged from 3-5 waves for regime 1 injection, increased to an average of 7 waves for regime 2 and regime 3 injections.

Table 4 shows results for the case of a higher viscosity water/glycerine injectant μ = 18.4 centipoise, σ = 73.0 dyne/cm. The unsteadiness of the jet structure is quite noticable from the λ/d column

entries, with values ranging from 0.5 to 2.8 times the injector diameter. By neglecting the extreme data points, it becomes evident that the wavelength is independent of the injection rate $\bar{q}$. The average non-dimensional value for the wavelength is 1.5; this average is 25% larger than the corresponding average value of Table 2 (pure water) μ = 1.0 C.p., σ = 73.0 dyne/cm.). The average non-dimensional value for the wave amplitude is 0.7 diameter. This value is 60% greater than the corresponding average of Table 2. Again the data suggests that wave amplitude is independent of $\bar{q}$. The λ/α entries averaged to 2.5. This suggests that wave formation become deeper and shorter. The NλF column data shows that for regime 1 and 2, 7 waves were present on the cohesive jet body before the point of first cross fracture. This process continued in regime 3, and at the highest injection rates ($\bar{q}$ = 18, 20) 15 waves were present on the cohesive jet body. The entries in the L/d column varied from a minimum of 1.5 diameter for $\bar{q}$ = 2 to a maximum of 4.4 diameter corresponding to injection at $\bar{q}$ = 14. Further increases in $\bar{q}$ decreased the L/d value of a minimum of 2.6 diameters at $\bar{q}$ = 20. A direct comparison between Tables 3 and 4 shows that L/d entries have the same trend. The TR/d column entries in regime 1 show that the large wave region started right after the coherent region of the jet column. For regime 2 and 3, the capillary wave zone increases in length from 1.0 diameter to 5.6 diameters at $\bar{q}$ = 14 and then decreases to 3.7 diameters at $\bar{q}$ = 20. Again, the results follow the same trend when compared with the results of Tables 2 and 3.

Table 5 shows the data for the case of the still higher viscosity water/glycerine injectant μ = 27.6 centipoise, σ = 73.0 dyne/cm.

By neglecting the high and low extremes of the data, it can be seen that the wavelength and amplitude are independent of injection rate $\bar{q}$. Injection throughout the three regimes resulted in an average non-dimensional wavelength and amplitude of 1.2 and 1.1 diameters respectively. The wavelength is 12% smaller than the pure water results of Table 2, while the wave amplitude has increased 162% over the value of Table 1. The λ/α entries average to 1.1. This suggests that wavelength and wave amplitude have the same magnitude which indicates truly steep waves. The number of large waves from the start of the large wave zone to the point of first cross fracture varies from 4 waves in regime 1 to 7 for regime 2. The number of waves further increases to an average of 10 waves for regime 3 injection. Throughout the 3 regimes, the injection Reynolds number based on injector diameter and injectant velocity remained below 2000. A coherent, disturbance free or perhaps a laminar section on the jet column immediately near the injector has formed. The axial length of this zone has a minimum value of 1.6 diameter for regime 1. This length increases to 5.4 diameters for regime 2. Further increases in the injection rate decreased the length of the coherent column to a minimum of 2.4 diameters at $\bar{q} = 20$. The entries of TR/d column show the non-dimensional length of capillary wave zone. The entries increased from 5.4 diameters for regime 1 injections to 8.0 for injections in regime 2. The regime 3 cases show a trend with values of TR/d ranging from 4.4 to 8.5.

Table 6 shows the variation λ/d, α/d, λ/a, $N\lambda F$, L/d and TR/d data for the low surface tension case of a water/alcohol injectant $\mu = 1.0$ centipoise and $\sigma = 33.5$ dyne/cm. The average value for the

wavelength on the jet surface was 1.7 diameters. This is a 24% increase over the results for pure water in Table 2. The wave amplitude has a value of 0.7 diameters. This is a 55% increase over the results of Table 2. The number of waves on the cohesive jet body increases from 3 waves in regime 1 to a maximum of 12 waves in regime 3. The cohesive jet column disappeared throughout the first 2 regimes and only appeared to have a significant measurable length in the latter part of the third regime. The capillary wave zone of the cohesive jet body has a longer length compared to the results of Tables 3-5 and is of the same magnitude compared with the results of Table 2.

Table 7 shows the data for the very low surface tension Fluorinert spray plume μ = 1.5 centipoise, σ = 15 dyne/cm. The λ/d entries show the unsteady nature of the wave growth on the jet surface. The surface waves have the largest wavelengths compared to previous results, with average non-dimensional wavelength and amplitude of 1.9 and 0.8 diameters respectively which corresponds to 12% and 20% increases over the tabulated results for water/alcohol in Table 6. The surface waves on the Fluorinert spray plume have increased in wavelength and amplitude an average of 39% and 85% respectively over the tabulated results for the pure water spray plumes in Table 2. The results clearly suggest that wave formation on the windward surface of the jet is inversely related to the surface tension of the injectant. Decreasing surface tension stimulates the process of wave growth both in wavelength and amplitude. The ratio of wavelength/wave amplitude roughly averaged to 2.5. For regime 1 and 2, the cohesive jet body consisted of 2-4 large aerodynamically induced waves. Regime 3

injection mostly exhibited 7 to 8 waves on the cohesive jet body. The coherent, disturbance free jet column did not appear in any regime. The capillary wave zone TR/d had a minimum length of 2.3 diameters and a maximum of 5.5 diameters at regime 2($\bar{q}$ = 4, 10). Further increases in $\bar{q}$ decreased the length of the capillary wave zone to 4.2 diameters at $\bar{q}$ = 16. The trend is similar to previous cases.

Fig. 25 shows the effects of viscosity and surface tension on wave growth phenomena associated with Regime 2 ($\bar{q}$ = 8). The waves associated with the Fluorinert plume (σ = 15) dyne/cm.) increase linearly in length from λ/d = 0.96 at x/d = 4.1, Θ = 4° diameters. The water/alcohol spray plume (σ = 33.5 dyne/cm.) exhibits waves of smaller wavelength along the surface. The waves stay equal in length λ/d = 1.6 from θ = 16° to Θ = 32°, then increase in length to 2.5 diameter with increasing axial distance along the jet. The pure water spray plume (σ = 73.0 dyne/cm.) exhibited waves along its surface which stayed constant in wavelength (λ/d = 1.4) from Θ = 16° to Θ = 38°. Increasing viscosity first increases the wavelength to λ/d = 1.55 with water/glycerine injection (μ = 10.6 centipoise). Again the waves exhibit constant length along the jet column from Θ = 18° to Θ = 39°. Further increases in viscosity decreases the wavelength of the surface disturbances to λ/d = 1.36 for μ = 18.4 centipoise and λ/d = 1.0 for μ = 27.6 centipoise.

The tabulated results of λ/d columns of Tables 1.6 and 7 are plotted vs. the injectant surface tension (σ) Fig. 26. The plot shows a wide band of data at each of the three stations (σ = 15, 33.5, 73.0). This is due to the unsteady nature of the jet in the crossflow and lack

of a precise measurement technique. However, the plot clearly shows that increasing surface tension decreases the wavelength of the surface disturbances.

The tabulated results of λ/d column of Tables 2, 3, 4 and 5 are plotted vs. injectant viscosity (μ) Fig. 27. Again the plot shows a wide band of data at each station (μ = 1.0, 10.6, 18.4, 27.6). However, it can be observed that increasing viscosity at first increases the wavelength of the disturbances, further increases in the viscosity decreases the wavelength of the surface waves.

In a summary it can be said that increasing viscosity decreases the wavelength of the disturbances, on the other hand wave amplitude greatly increases with increasing viscosity. These two effects together result in deep square looking waves on the windward edge of the jet plume, which in turn helps the process of jet break-up via ligament formation. Decreasing surface tension increases both wavelength and wave amplitude. The tabulated data and the photographs help show the unsteady nature of the wave growth. For the cases of low surface tension spray plumes, the waves are generally more uniform and almost sinusoidal. The wave growth enhances the process of jet break-up via wave generation and crossfracture for the cases of low surface tension injections.

6.4 Effects of Viscosity and Surface Tension on Jet Penetration

The test plan involved injection of various injectants at several values (1-20) of the liquid jet to freestream dynamic pressure (or momentum flux) ratio, $\bar{q} = \rho_j v_j^2 / \rho_\infty v_\infty^2$. Water with viscosity of 1.0

centipoise and surface tension of 73.0 dyne/cm. served as the reference injectant. Five solutions of different glycerine concentrations in water were prepared to provide injectants of various viscosities (Table 1). A 36% mixture of alcohol in water was prepared to reduce the surface tension of water to 33.5 dyne/cm. A single circular injector of 0.96mm. orifice diameter was used throughout the investigation to eliminate the effects of injector geometry on penetration.

Long exposure (10^{-3} sec.), back lighted streak photographs of the jet in the crossflow were obtained Fig. (28) and the solid black portion of the spray in the airstream was measured to reveal the jet penetration height. Penetration measurements were taken at 5.2, 10.4, 26.0 and 52.0 diameters downstream of the injector. The results are tabulated in Tables (8-14). The effects of injectant mass flow rate, injection velocity and injection Reynolds number were extracted from the values of dynamic pressure ratio $\bar{q}$.

Fig. 29 shows the non-dimensional penetration height h/d of water and the five solutions of water/glycerine as a function of $\bar{q}$ measured at 26 diameters downstream of the injector. The water/glycerine data points have all collapsed around a single line and consistently show a higher penetration than the penetration of water. This difference in penetration height increases with increasing $\bar{q}$. At $\bar{q}$ = 20, highly viscous liquid jets penetrate the crossflow 22% more than a water jet.

Fig. 30 shows the non-dimensional penetration height h/d of water and the five water/glycerine solutions as a function of $\bar{q}$ measured at 52 diameters downstream of the injector. Again, the water/glycerine data points have all collapsed around a single line, and they consis-

tently show a larger penetration than that of water, with a maximum of 34% higher penetration at $\bar{q}$ = 20. A direct comparison of Fig. 29 and 30 shows that the peneTration of water/glycerine injectants measured at 52 diameters downstream of the injector port has increased 20% over the penetration measured at 26 diameter station. The same comparison for water jet yields only a 7% difference. This suggests that the penetration profile of more viscous jets in the crossflow is different from the low viscosity jet profiles. The low viscosity liquid jets tend to be atomized at a distance of roughly 25 diameters downstream of the injector and the atomized particles are carried along by the freestream with negligible further penetration in the crossflow.

Fig. 31 shows the non-dimensional penetration height h/d measured at x/d = 26 as a function of injectant velocity. The trend is similar to the penetration height as a function of $\bar{q}$. Viscous jets show a higher penetration than water, with a maximum of 34% more penetration at jet velocity of 50 m/sec.

Fig. 32 shows the non-dimensional penetration height measured at 52 diameters as a function of jet velocity. The penetration of the more viscous jets are greater than that of water as injectant, with a maximum of 44% more penetration at jet velocity of 50 meter/sec. Comparison of Figures 47 and 48 shows that water/glycerine injectants have 20% higher penetration at 52 diameters downstream compared to 7% for water jet plume. This again illustrates the fact that higher viscosity liquid jets tend to continue their crossflow penetration at large downstream distances.

Fig. 33 shows the non-dimensional penetration height h/d as a

function of mass flow rate measured at x/d = 26. All the points have collapsed around a single line. Fig. 34 shows the non-dimensional penetration height as a function of mass flow rate at x/d = 52. Again, all the points have collapsed around a single line. A study of Figures 33 and 34 suggests that penetration height is independent of viscosity when the mass flow rate is the controlling injection parameter.

Fig. 35 shows a study of non-dimensional penetration height h/d as a function of Reynolds number based on injector diameter and injectant velocity. The study shows that as viscosity increases, higher penetrations are reached at lower values of Reynolds number. For water/glycerine injectants of viscosities greater than 27.6 centipoise the injection Reynolds number stays in the laminar regime (less than about 2000) throughout the test series ($\bar{q}$ = 1-20).

Fig. 36 contains 8 plots. Each curve represents non-dimensional penetration height h/d measured at x/d = 26 as a function of viscosity for a specific value of dynamic pressure ratio. The overall observation of the whole figure confirms the fact that an increase in dynamic pressure ratio results in higher penetration of the jet in the crossflow. One by one examination of each curve shows that water with viscosity of 1.0 centipoise has the lowest penetration. Increasing viscosity increases the penetration height. Water/glycerine injectant at μ = 10.5 centipoise shows the highest penetration. Further increases in viscosity reduce the penetration height, with the minimum at 40.5 centipoise. After this point, an increase in viscosity increases the penetration of the liquid jet in the crossflow. At this time a physical explanation

of this phenomena is not available. This behavior can be attributed to injector characteristics or possibly to the physical properties of the injectant. A more indepth investigation of the problem is necessary.

Fig. 37 shows the non-dimensional height of water and a 36% mixture of alcohol in water as a function of $\bar{q}$ measured at x/d = 26. The surface tension of water/alcohol mixture is 33.5 dyne/cm. which is 65% lower than the surface tension of pure water. Throughout the range of $\bar{q}$ there is not a significant difference between the penetration heights, with both data being scattered around the same line.

Fig. 38 is a non-dimensional penetration height of pure water and water/alcohol mixture as a function of $\bar{q}$ measured at the non-dimensional downstream distance of x/d = 52. Again, there are no significant differences. The data shows that both pure water and the lower surface tension fluid penetrate the crossflow equally.

A further reduction of surface tension by introduction of larger quantities of alcohol in water is not possible. Ethanol has a surface tension of 23 dyne/cm. and higher concentrations of it in water does not change the surface tension greatly. Also, injection of pure alcohol into the crossflow was not possible since the secondary effects of rapid evaporation of the jet further changes penetration and jet structure which was beyond the scope of this study.

6.5 The Effects of Viscosity and Surface Tension on Spray Fineness

The physical properties of injectants such as surface tension and viscosity determine the spray fineness. To establish these effects, four injectants were used, water, water/alcohol, water/glycerine and

Fluorinert (C_8F_{18}). The mean droplet diameter resulting from injection of these injectants was measured at various stations along and across the jet plume. The effects of dynamic pressure ratio and injector diameter upon droplet diameter were also included. The results are tabulated in Tables 15-28. To help the reader understand the nature of the droplet size variations, Figs. (39-42) were prepared. These figures show a scale drawing of the jet penetration, the location of the measurement stations and corresponding mean droplet diameter at that station. Each Table contains four columns, x/d, y/d, h/d and D_{32}. The x/d entries are the non-dimensional distance downstream of the injector port. The y/d column show the non-dimensional distance measured from the surface of the flat plate. The values of x/d and y/d are the coordinate locations of the incident beam in the jet plume with respect to the injector port which is at x/d = 0, y/d = 0. The h/d entries denote the non-dimensional penetration heights measured from the relatively long exposure streak photographs. The D_{32} column entries are the measured droplet diameter at station x/d, y/d in the jet plume.

Table 15 and Fig. 39a show the variation of droplet diameter in the plume for the case of pure water injectant at $\bar{q}$ = 12 with d = 0.45 mm. ($Re_j = 19.6 \times 10^3$, $We_j = 1.13 \times 10^4$). Measurements were taken along the jet from x/d = 10.9 to 207.7. The droplet diameter decreased as one moved downstream. For example D_{32} = 19.0 microns at (x/d = 54.4, y/d = 11.4, h/d = 23.0) which decreased to D_{32} = 14.0 microns at (x/d = 207.7, y/d = 12, h/d = 24). The cross plume measurements of droplet size revealed the fact that droplet diameter decreases to its smallest value near the boundaries of the plume. At x/d = 109.4, y/d was changed

from 6.6 to 21.9 and the droplet diameter increased in size from 10 to 14 microns, the decreased to 13 microns. The same holds true for the cross-plume measurements taken at x/d = 207.7. At stations x/d = 10.9 and 22.0 the droplet sizes are small, this may be due to the fact that very near the injector orifice the total laser beam is not in the main-jet and the measurements are of the small particles that have sheared away from the main jet column.

Table 16 and Fig. 39b show the variation of droplet diameter in the jet plume for the case of pure water injectant at $\bar{q}$ = 4, d = 0.45 mm. ($Re_j = 11.3 \times 10^3$, $We_j = 3.7 \times 10^4$). The most important result is the general increase in mean droplet diameter compared to that found at $\bar{q}$ = n. The droplet diameter again decreases in size as one moves down-stream of the injector. Because of the small penetration of the jet at $\bar{q}$ = 4 with respect to the size of the incident beam, it was not possible to check the variation of mean droplet diameter across the plume in this case.

Table 17 and Fig. 39c show the results of a study of droplet distribution across the along the jet plume for pure water, at $\bar{q}$ = 12 but now with a larger diameter injector d = 0.96 mm. ($Re = 41.2 \times 10^3$, $We = 2.3 \times 10^4$). The comments for Table 16 with regards to droplet diameter distributions throughout the spray also apply here. It appears that, at high values of $\bar{q}$, the jet plume breaks up fully and the droplet diameters reach a limiting size regardless of the injector diameter.

Table 18, Fig. 39d show droplet distributions throughout pure water spray, injected at $\bar{q}$ = 4 through the bigger injector d = 0.96 mm.

($Re_j = 23.9 \times 10^3$, $We_j = 8.1 \times 10^3$). The comments about the variation of droplet diameter in the plume are the same as the ones for previous tables. However, there is an increase in droplet diameter as compared to that in Table (16).

Table 19 and Fig. 39e give the distribution of droplets as the result of injection of pure water through the largest diameter injector d = 1.5 mm at $\bar{q} = 4$, ($Re_j = 36.3 \times 10^3$, $We_j = 1.2 \times 10^4$). Clearly the cross plume variation of droplet diameter is similar to that of the previous figures and Tables. However, this injector produces the largest diameter droplets, which decrease in size as they move downstream of the injector port.

Table 20 and Fig. 40a display the variation of droplet diameter across and along the jet for injection of the lower surface tension water/alcohol solution at $\bar{q} = 12$ through the smallest injector d = 0.45 mm. ($Re_j = 18.4 \times 10^3$, $We_j = 2.3 \times 10^4$). The surface tension of this injectant is roughly one-half of the surface tension of pure water, while it has the same viscosity. Again, the droplet diameter decreases in size as one moves downstream from the injector port. The process of atomization seems to be more complete than that for pure water, as there is not a great variation in droplet diameter throughout the plume. A direct comparison with results of Table 15 (water, $\bar{q} = 12$) shows that due to a lower surface tension complete atomization of the jet takes place earlier downstream of the injector port, roughly at x/d = 33 for water/alcohol rather than x/d = 109.9 for pure water. Also, the droplet diameters appear to be slightly smaller for the case of lower surface tension keeping other variables constant.

Table 21 and Fig. 40b show the same type of study as in Table 20, but here the injection is carried out at $\bar{q}$ = 4 with other injectant properties being held constant ($Re_j = 10.6 \times 10^3$, $We_j = 7.5 \times 10^3$). It is evident that droplet size has increased in comparison to the results of Table (20) (water/alcohol, $\bar{q}$ = 12). The droplets are however, smaller than the droplets resulting from atomization of pure water Table (16). It is also clear that, the process of atomization is completed at a shorted distance downstream of the injector port, x/d = 54 for water/alcohol injectant and x/d = 109 for the case of water spray plume.

Table 22 and Fig. 40c show the droplet diameter variation in water/alcohol jet plume injected at $\bar{q}$ = 12, d = 0.96 mm ($Re = 39.5 \times 10^3$, $We = 5.0 \times 10^4$). The results clearly show that atomization is almost instantaneous at x/d = 54. The droplet diameter stays almost constant as one moves downstream, and the variation of droplet diameter across the jet plume is not great. A direct comparison with the results of Table 17 shows that the water/alcohol spray has a finer spray, but more importantly the atomization is more uniform throughout the jet plume.

The results shown in Table 23 and Fig. 40d are the results of water/alcohol injection through the larger injector d = 0.96 at $\bar{q}$ = 4 ($Re_j = 22.8 \times 10^3$, $We_j = 17 \times 10^4$). A comparison with the results of the previous Table (water/alcohol, d = 0.96, $\bar{q}$ = 12) shows that decreasing $\bar{q}$ increases the droplet diameter. The droplet diameter decreases in size for stations downstream from the injector orifice which was not observed at the higher $\bar{q}$ injection. (Table 22). Also, the values of D_{32} are slightly smaller than the tabulated results of Table 18 (pure water, d = 0.96, $\bar{q}$ = 4).

The droplet diameter variation across and along the jet plume for water/alcohol injectants injected through the largest diameter injector d = 1.5 mm. at $\bar{q}$ = 4 (Re_j = 35.8 x 10^3, We_j = 2.7 x 10^4) are given in Table 24 and Fig. 40e. The variations across and along the plume follow the now familiar trend. A comparison with the results of Table 19 (pure water, d_j = 1.5 mm) shows that the water/alcohol injectant has a much finer spray than that for pure water. Also, the atomization of the jet seems to get underway much faster and to go to completion earlier than that of pure water.

Table 25 and Fig. 41a show the mean droplet diameter variation resulting from atomization of very low surface tensions. Fluorinert σ = 15 dyne/cm, μ = 1.5 centipoise, d = 0.96, $\bar{q}$ = 12 (Re_j = 21.0 x 10^3, We_j = 3.9 x 10^5). Due to extensive atomization, the light absorption by the spray particles at stations deep inside the spray was greater than 20%, clearly suggesting multiple scattering of the light. Therefore, it was only possible to obtain droplet size information for stations very near the spray edge with the DSLM. The results suggest extreme atomization. The droplets at stations x/d = 5.2, 10.4, 15.6 and 28 were all 7 microns in diameter. At x/d = 60 and 93 the droplets were reduced in diameter to 5 microns. The small droplet diameter near the spray plume edge together with the excessive light absorptions suggest that atomization is rapid and complete.

Table 26 and Fig. 41b illustrate the droplet diameter variation resulting from atomization of Fluorinert spray d = 0.96 mm., $\bar{q}$ = 4 (Re_j = 36.3 x 10^3, We_j = 1.7 x 10^6). The droplet diameters are slightly larger than the previous case. At x/d = 5.2, 10.4, 15.6 and

28 the droplets were 8 microns in diameter, while slightly dropping to 7 microns at x/d = 60 and 93. Again, it can be said that lower surface tension Fluorinert spray atomizes rapidly into a uniform very small particle size spray.

Table 27 and Fig. 42a show the variation in droplet diameter in the water/glycerine jet plume injected at $\bar{q}$ = 12 through the middle size injector d = 0.96 mm ($Re_j = 4.8 \times 10^3$, $We_j = 2.4 \times 10^4$). The viscosity of this injectant is ten times greater than that of pure water, but has the same surface tension as water. Again, the study of droplet variation across and along the jet shows that droplets are the smallest at or near the plume outer edges, and that droplet diameter decreases as one moves downstream of the injector. Comparison with the data of Tables 25 and 17 (water, water/alcohol) show that an increase in viscosity while holding other properties constant increases the droplet diameter. Further, the process of atomization across the jet is not as uniform as for the cases of water/alcohol and pure water spray plumes.

Tables 28 and Fig. 42b give the droplet sizes at several stations along and across the water/glycerine spray injected at $\bar{q}$ = 4 through middle size injector d = 0.96 mm. ($Re_j = 2.8 \times 10^3$, $We_j = 8.1 \times 10^3$). The atomization of the jet is slow, and throughout the plume the particles are large. The droplet size decreases at first from 47 microns at x/d = 15.6, y/d = 7.0 to 36 microns at x/d = 60, y/d = 93. However, after x/d = 60 the droplets stay constant in size. At x/d = 93 station the cross diameter measurements revealed particles of almost identical in diameter to that of x/d = 60 station. It is clearly noted that the

smallest droplets are near the windward edge of the spray.

In a short summary it can be said that droplet diameter is inversely related to jet/free-stream dynamic pressure ratio $\left(\bar{q} = \frac{\rho_j v_j^2}{\rho_\infty v_\infty^2}\right)$. Therefore, for given freestream conditions increasing jet velocity decreases droplet diameter, or vise-versa. Droplet diameter increases or decreases monotonically with jet diameter, viscosity and surface tension of the injectant. Increasing surface tension, viscosity or jet diameter increases the resultant droplet diameter in the spray plume. It has been suggested that simple interrelations of these parameters such as Reynolds and Weber number groupings ($Re = \rho ud/\mu$, $We = \rho u^2 d/\sigma$) are capable of correctly correlating the mean droplet diameter to the experimental conditions. In the present test program the injection Reynold and Weber numbers had a range of (2.8×10^3 - 41.2×10^3, 3.7×10^3 - 1.7×10^6) respectively. This is due to jet diameter, jet velocity, injectant viscosity and surface tension variations programmed in the test. Both Reynolds and Weber number increase as a result of increasing jet diameter and jet velocity. Decreasing viscosity and surface tension of the injectant also increases the two non-dimensional parameters.

In depth study of Tables 15-28 shows that, mean droplet diameter does not follow the trends predicted by either Reynolds or Wever numbers by themselves. For example, from a comparison of the results of Table 26 (water/glycerine spray, μ = 10.0 centipoise, $Re_j = 2.8 \times 10^3$) and Table 18 (water, μ = 1.0 centipoise, $Re_j = 23.9 \times 10^3$) it can be concluded that increasing Reynolds number by decreasing viscosity has resulted in smaller droplet diameter. However, the exact opposite

conclusions can be drawn by comparison of Table 19 (water, d = 0.15 mm, μ = 1.0, $\bar{q}$ = 4, Re_j = 36.3 x 10^3) and Table 18 (water, d = 0.96, μ = 1.0, $\bar{q}$ = 4, Re_j = 23.9 x 10^3). This time increasing Reynolds number by increasing diameter increases the dropelt diameter. The same type of argument holds true for Weber number effects. Thereby it is clear that the relationship between surface tension, viscosity, injector diameter, jet velocity to the mean droplet diameter is more complex than through a simple Reynolds and Weber number correlation.

6.6 Effects of Viscosity and Surface Tension on Wave and Clump Velocities Along the Jet

Due to the poor resolution and small image size of the rotating mirror photographs Fig. 43, the wave speed and clump velocity measurements were obtained from the high magnification (3:1) photographs of the fixed mirror photographic technique Figs. (44a-f). First, the wave-speed along the jet plume at or near the sonic point was measured. This was decided based on the assumption that in most cases the jet travels downstream with small increasing penetration after the sonic point. Also, it is noted that the waves near the sonic point are large and very high amplitude (deep), marking the beginnings of the break-up and clump formation processes. The clump velocity was only measured when a clear picture of a separated liquid clump was recorded on both photographs. Due to extensive atomization of the low viscosity and low surface tension liquid jets, the clumps were not easily and clearly photographed. For high viscosity liquid jets, the clump formation was easily recorded. However, at times the more viscous jets did not clearly break-up into clumps within the view field of the photographs.

The results are tabulated in Tables 29-34. Each table consists of five columns $\bar{q}$, v_j, wv, wvs and cv. The $\bar{q}$ entries denote the ratio of the jet to freestream dynamic pressures. The v_j column entries are the injectant injection velocities associated with each $\bar{q}$. The wv column entries show the wave velocities of the large aerodynamically induced waves. These measurements were taken from the portion of the jet column which was bent 10-30 degrees to downstream direction, i.e., the flow around the jet had turned between 10-30 degrees. The wvs column entries show wave velocities on the jet plume near or at the sonic point where the jet had turned roughly 60 degrees to the downstream direction. The cv column entries denote the clump velocities after the cross fracture of the jet.

The results are tabulated in Tables 29-34. To clearly illustrate the effects of surface tension and viscosity on the wave propagation speed and liquid clump velocities Figs. 45-50 were prepared. To obtain wave propagation speed it was necessary to subtract contribution of local jet velocity V_L from the tabulated results of wv and wvs entries. The local jet curvature is determined by the downstream and the vertical jet velocity vx, v_y at that location. Assuming conservation of momentum and small changes in the spray cross sectional area vertical jet velocity v_y can be assumed to be equal to jet bulk velocity v_j. Thus the resultant local velocity is simply $VL = \frac{v_j}{\cos\Theta}$.

The results of Tables 29-34 show scatter which can be accounted for in many ways. High speed movies of the jet in the crossflow show that at times the entire jet shifts in the crossflow via a whipping mode. Although it has been reported that the frequency of this type

of movement is an order of magnitude less than the picture frame rate of the multi-exposure photographs that can still introduce some inaccuracies. The wave speed measurements were obtained from the time displacement difference of the waves obtained from the photographs. In order to accomplish this, several tasks has to be performed: a) the same waves had to be identified on the two photographs, b) the jet curvature was matched to an arc of a circle of known radius, c) the angle between the wave peaks and the injector surface were measured on each photograph, d) from the angles the wave displacements along the jet curvature were measured and finally from the displacement differences the wave speeds were calculated. As it can be realized the whole process is judgmental which can introduce inaccuracies. However, the errors should present themselves with the same magnitude in all measurements. It is believed that the data shows the trends accurately.

The data in each of the Tables clearly shows that the wave speed wv is always greater than the corresponding jet velocity, suggesting that the surface waves propagate downstream along the jet surface. The wvs entries are greater than the corresponding wv speeds at a given $\bar{q}$, suggesting that the disturbances accelerate downstream on the jet surface. The highest values correspond to the clump velocities. Increasing $\bar{q}$ first increases the clump velocities. Clump velocity is independent at $\bar{q}$ at high injection rates. This can be due to the fact that, at higher $\bar{q}$, penetration of the jet is greater and the liquid clumps are away from the flat plate and the boundary layer effects.

Fig. 45 illustrates the effects of surface tension and injection rate $\bar{q}$ on wave propagation velocity on the cohesive jet column. Three

injectants (water σ = 73.0 dyne/cm., water/alcohol σ = 33.5 dyne/cm., and Fluorinert σ = 15 dyne/cm.) were tested. It is readily observed that wave propagation velocity is independent of $\bar{q}$ for all three injectants. Water and water/alcohol injectants show the same wave propagation speed at roughly 78 meters/sec. A substantial decrease in surface tension of the injectant (Fluorinert, σ = 15 dyne/cm.) has increased the disturbance propagation speed to roughly 125 meters/sec.

The effects of injection rate $\bar{q}$ and surface tension of the injectant on the wave propagation speed near the sonic point on the jet cohesive body is shown in Fig. 46. Wave propagation speed is nearly constant across the $\bar{q}$ range for all three injectants. Water σ = 73.0 dyne/cm. and water/alcohol σ = 33.5 dyne/cm. show nearly equal wave propagation speed of 270 meters/sec. Fluorinert with surface tension of 15 dyne/cm. has a higher propagation velocity at nearly 300 meters/sec.

Fig. 47 shows the effects of $\bar{q}$ and injectant surface tension on the liquid clump velocity. It is evident that clump velocity for all three injectants is independent of $\bar{q}$. The water spray plume (σ = 73.0 dyne/cm.) has the lowest clump velocity of 420 meters/sec. The waves on water and water/alcohol spray plume showed nearly equal propagation velocities on the cohesive jet column and near the sonic point, however due to low surface tension water/alcohol spray breaks up rapidly and closer to the injector port. Therefore, the separated clumps have a longer residence time in the crossflow and accelerate to higher velocities (505 meters/sec.) within the same distance. Further reduction in surface tension of the injectant (Fluorinert, σ = 15 dyne/cm.)

increased the clump velocity to the highest value of 545 meters/sec.

Fig. 48 gives the effects of viscosity and injection rate $\bar{q}$ on the wave propagation velocity of the cohesive jet column waves. As before, wave propagation velocity is independent of $\bar{q}$. The waves of the water spray plume (μ = 1.0 centipoise) propagate downstream at 78 meters/sec. Increasing viscosity at first increases the wave propagation velocity. Water/glycerine (μ = 27.6 centipoise) has an average wave propagation speed of nearly 210 meters/sec. across the $\bar{q}$ range. Further increases in viscosity decrease the propagation speed. The more viscous water/glycerine spray (μ = 40.5 centipoise) shows an average wave propagation speed of 148 meters/sec. throughout the $\bar{q}$ range. Waves on the highest viscosity plume (water/glycerine, μ = 59.8 centipoise) propagate downstream at roughly 134 meter/sec.

Fig. 49 displays the effects of increasing viscosity on wave propagation speed near the sonic point. The propagation velocity is independent of $\bar{q}$. Increasing viscosity has reduced wave accelerations. All data for the higher viscosity injectants show that wave propagation is roughly 150 meter/sec. which is substantially lower than the wave propagation speed of water waves at the sonic point (270 meters/sec.). A comparison of Figs. 59 and 58 suggests that the waves of the viscous jets propagate downstream along the jet cohesive body with virtually no acceleration.

Fig. 50 shows the effects of injection rate $\bar{q}$ and injectant viscosity on the liquid clump velocity. It is clearly seen that clump velocity is independent of $\bar{q}$ for all injectants. Water (μ = 1.0 centipoise) has the highest clump velocity (420 meters/sec.). Increasing

viscosity decreases the clump velocity to 390 meters/sec. for the case of water/glycerine ($\dot{\mu}$ = 27.6 centipoise). The more viscous injectants (μ = 40.5 centipoise and μ = 59.8 centipoise) show nearly the same clump velocity at 290 meters/sec.

In summary it can be said that moderate changes in surface tension does not change the wave propagation velocity on the jet cohesive column or near the sonic point. Very low surface tension sprays exhibit waves with greater propagation velocity both on the cohesive jet column and near the sonic point on the spray plume. Liquid clump velocity increases with decreasing surface tension. Increasing viscosity (μ = 27.6 centipoise) at first increases wave propagation velocity of the cohesive jet column waves. Further increases in injectant viscosity decreases the wave propagation velocity. Increasing viscosity decreases wave propagation velocity at the sonic point. Increasing viscosity decreases liquid clump velocity. Wave propagation velocity on the jet column and at the sonic point and liquid clump velocity are independent of injection rate $\bar{q}$.

References

1. Sherman, A., "Investigation into Breakup of Liquid Sheets and Jets in a Supersonic Gas Stream", Ph.D. Thesis, Univ. of Maryland, 1969.

2. Scherman, A. and J. A. Schetz, "Breakup of Liquid Sheets and Jets in a Supersonic Gas Stream", Paper No. 70-89 AIAA 9th Aerospace Sciences Meeting, New York, Jan., 1970.

3. Kush, E., "Decomposition of a Liquid Jet Injected Normal to a Supersonic Airstream", Ph.D. Thesis, Virginia Polytechnic Institute and State Univ., 1972.

4. Kush, E. and Schetz, J., "Liquid Jet Injection into a Supersonic Flow", AIAA Paper No. 72-1180 AIAA/SAE 8th Joint Propulsion Specialist Conference, New Orleans, La., Nov. - Dec., 1972.

5. Rayleigh, Lord, "On the Instability of Jets, Proc. of London Math Soc.", x, 4, 1878.

6. Rayleigh, Lord, "On the Instability of Cylindrical Fluid Surfaces", Phil. Mag. xxxiv, 59, 1892.

7. Weber, C., "Zum Zerfall eines Flussigkeitsstrahles", Ztsehr. f. angew Math. und. Mech., Vol. 2, 1931.

8. Tomstika, S., "On the Instability of a Cylindrical Thread of a Liquid Surrounded by Another Viscous Fluid", Proc. of Royal Soc. of London, A, 150, 322, 1935.

9. Castleman, R., "The Mechanics of Atomization of Liquids", J. of Research of the Bureau of Standards, b, 369, 1931.

10. Castleman, R., "The Mechanics of Atomization Accompanying Solid Injection", NACA Report 440, 1932.

11. Dunne, B. and Cassen, C., "Some Phenomena Associated with Supersonic Liquid Jets", Jour. of Appl. Phys., 25, 5, 1954.

12. York, J. L., ASME, pp. 1279-1286, Oct. 1953.

13. Yuen, M. C., "Correlation of Experimental Data on Disintegration of Liquid Jets", Industrial Eng. Chem. 47, 9, 1955.

14. Nayef, A. H., "Nonlinear Stability of Liquid Jets", Phys. of Fluids, 13, 841, April 1970.

15. Kelvin, Lord, "Influence of Wind on Capillary Waves in Water Suppressed Frictionless", Mathematical and Physical Papers, Cambridge V. Press, 1910, IV.

16. Jeffreys, H., "On the Formation of Water Waves by Wind", Proc. of Royal Soc. of London, 107, 189, 1925.

17. Lighthill, M. J., "Physical Interpretation of the Mathematical Theory of Wave Generation by Wind; Jour. Fluid Mech., 14, 384, 1962.

18. Lighthill, M. J., "Comm. Pure Appl. Math., xx, 1967.

19. Chang, I. D. and Russell, D., "Stability of a Liquid Layer Adjacent to a High-Speed Gas Stream", Phys. of Fluids, 8, 1018, June 1965.

20. Adelberg, M., "Mean Drop Size Resulting From the Injection of a Liquid Jet into a High Speed Gas Stream", AIAA Journal, Vol. 6, June 1968, pp. 1143-1147.

21. Mayer, E., "Theory of Liquid Atomization in High Velocity Gas Streams", Proc. of the 12th Int. Astronautical Congress, Academic Press, 731, 1950.

22. Joshi, P. and Schetz, J., "Effects of Injector Shape on Penetration and Spread of Liquid Jets", AIAA Paper No.74-1156 AIAA Journal, Vol. 13, No. 9, Sept. 1975, pp. 1137-1138.

23. Chelko, L. J., NACA RM E50F21, 1950.

24. Ingebo, R. D. and Foster, H. H., "Drop Size Distribution for Cross-current Breakup of Liquid Jets in Airstreams", NACA, TN 4087, 1957.

25. Schetz, J. McVey, W., Padhye, A., Munteanu, F., "Studies of Transverse Liquid Fuel Jets in High Speed Airstream", AFOSR-TR-76-1168, July 1976.

26. Weiss, C. and Warsham, C., "Atomization in High Velocity Airstream", ARS Journal, Vol. 29, No. 4, April 1959, p. 252.

27. Clark, B., "Breakup of a Liquid Jet in a Transverse Flow of Gas", NASA TN-D-2424, 1964.

28. Frode, J., Molder, S. and Szpiro, J., "Secondary Liquid Injection into a Supersonic Airstream", Journal of Spacecraft and Rockets, Vol. 3, No. 8, August 1966, pp. 1173-1176.

29. Reichenbach, R. and Horn, K., "Investigation of Injectant Properties on Jet Penetration in a Supersonic Stream", AIAA Journal, Vol. 9, No. 3, March 1971, pp. 469-472.

30. Horn, and Reichenbach, R., "Further Experiments on Spreading of Liquids Injected into a Supersonic Flow", AIAA Journal, Vol. 7, No. 2, Feb., 1969, pp. 358-359.

31. Shaikhuldinov, Z. G., Klevanskii, V. M., "Penetration and Mixing of Liquid Injected into Supersonic Transverse Gas Stream", Izvestiya vuz, Aviatsionnaya Tckhnika, Vol. 19, No. 1, pp. 99-108, 1976.

32. Chin, J. H., Sliepeevich, C. M. Tribus, M., "Particle Size Distribution in Polydispersed Systems by Means of Measurements of Angular Variation of Intensity of Forward - Scattered Light at Very Small Angles", Journal of Phys. Chem., No. 59, pp. 845-848, 1955.

33. Gumprecht, R. O. and Sliepeevich, C. M., "Scattering of Light by Large Spherical Particles", Journal of Phys. Chem., No. 57, pp. 90-95, 1953.

34. Dobbins, R. A., Crocco, L. and Glassman, I., "Measurements of Mean Particle Sizes of Sprays From Diffractively Scattered Light", AIAA Journal, Vol. 1, No. 8, Aug. 1963, pp. 1882-1886.

35. Mugele, R. A. and Evans, H. D., "Droplet Size Distribution in Sprays", Ind. Engr. Chem. 43, 1951, pp. 1317-1324.

36. Roberts, J. H. and Webb, M. J., "Measurement of Droplet Size for Wide Range Particle Distribution", AIAA Journal, Vol. 2, No. 3, Mar., 1964, pp. 583-585.

37. Gooderum, P. B. and Bushnell, D. M., "Atomization, Dropsize, and Penetration for Cross-stream Water Injection at High Altitude Reentry Conditions with Application to RAMC-1 and C-III Flights", NASA-TNO-6747, July 1972.

38. Birton, M. D., "Atomization of Liquids by Supersonic Air Jets, Journal of Ind. Eng. Chem., Vol. 47, No. 1, Jan., 1955, pp. 23-28.

39. Kurzious, S. and Raab, F., "Measurement of Droplet Size in Liquid Jets Atomized in Low Density Supersonic Streams", Report TP152, Aerochem Research Labs., March 1967.

40. Nejad, A., Schetz, J. and Jakubowski, A. K., "Mean Droplet Diameter Resulting from Atomization of a Transverse Liquid Jet in a Supersonic Airstream", AIAA-80-0899, May 6, 1980.

FIGURES

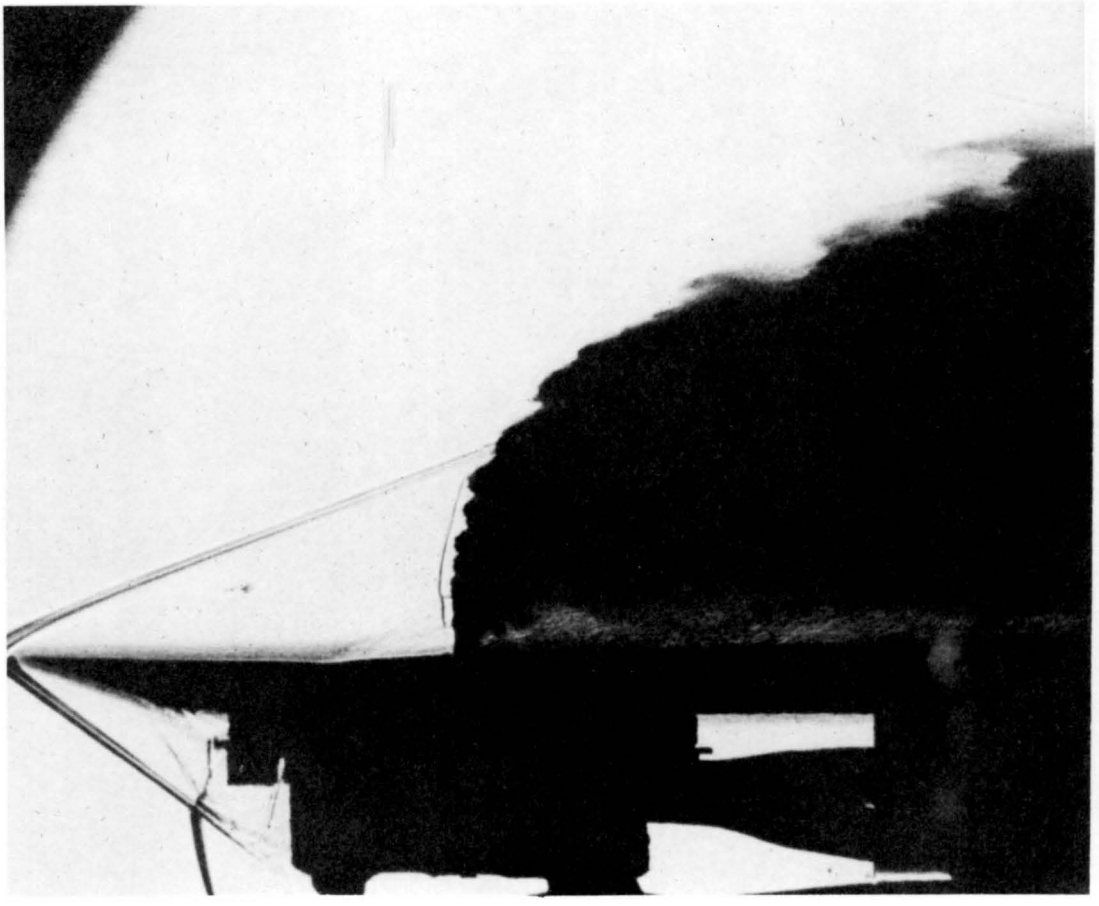

Fig. 1: Wide-view Spark Photograph of Transverse Liquid Jet Injection from a Flat Plate at M=3.0.

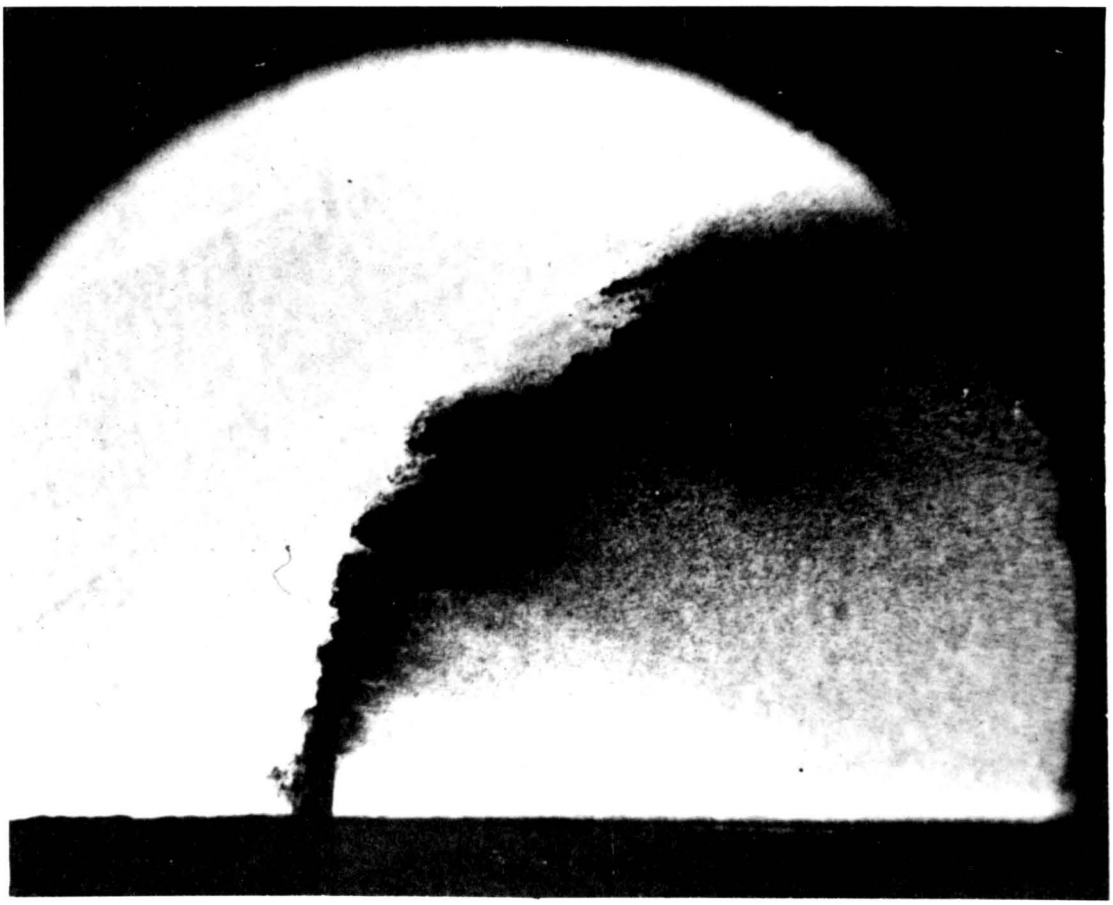

Fig. 2: Close-up, Nanosecond Photograph of Transverse Liquid Jet Atomization Process.

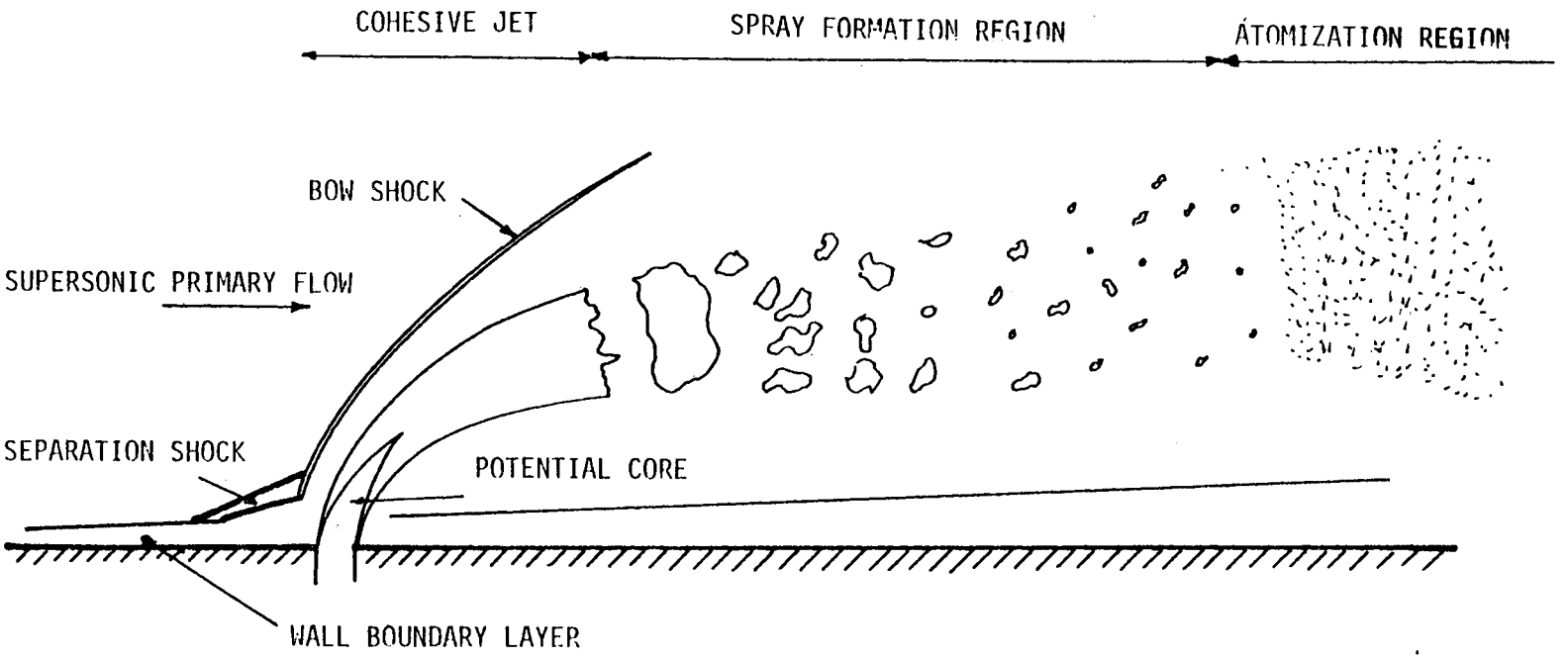

FIG. 3 SCHEMATIC OF NORMAL LIQUID JET IN SUPERSONIC FLOW

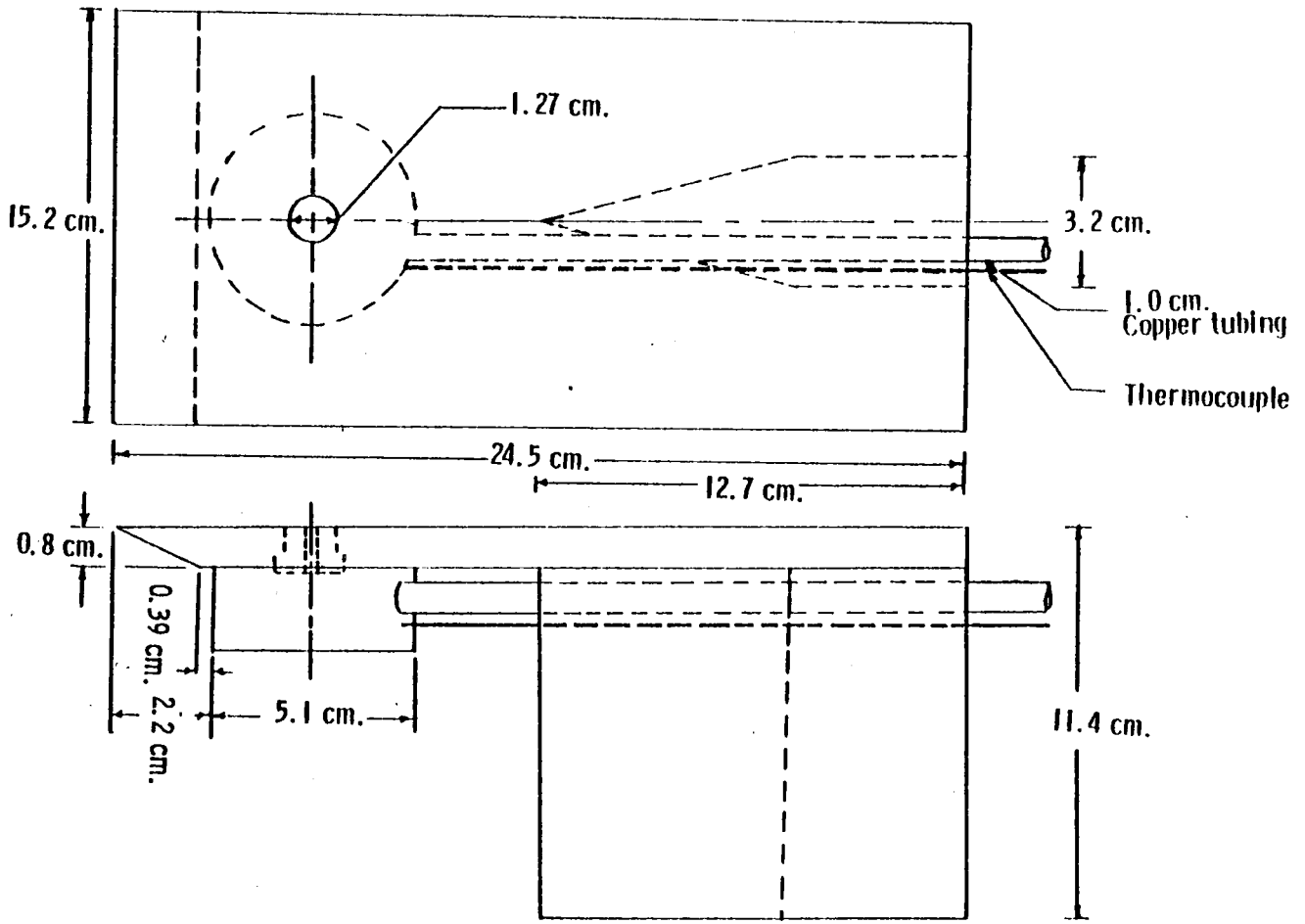

FIG. 4 SCHEMATIC OF FLAT PLATE MODEL

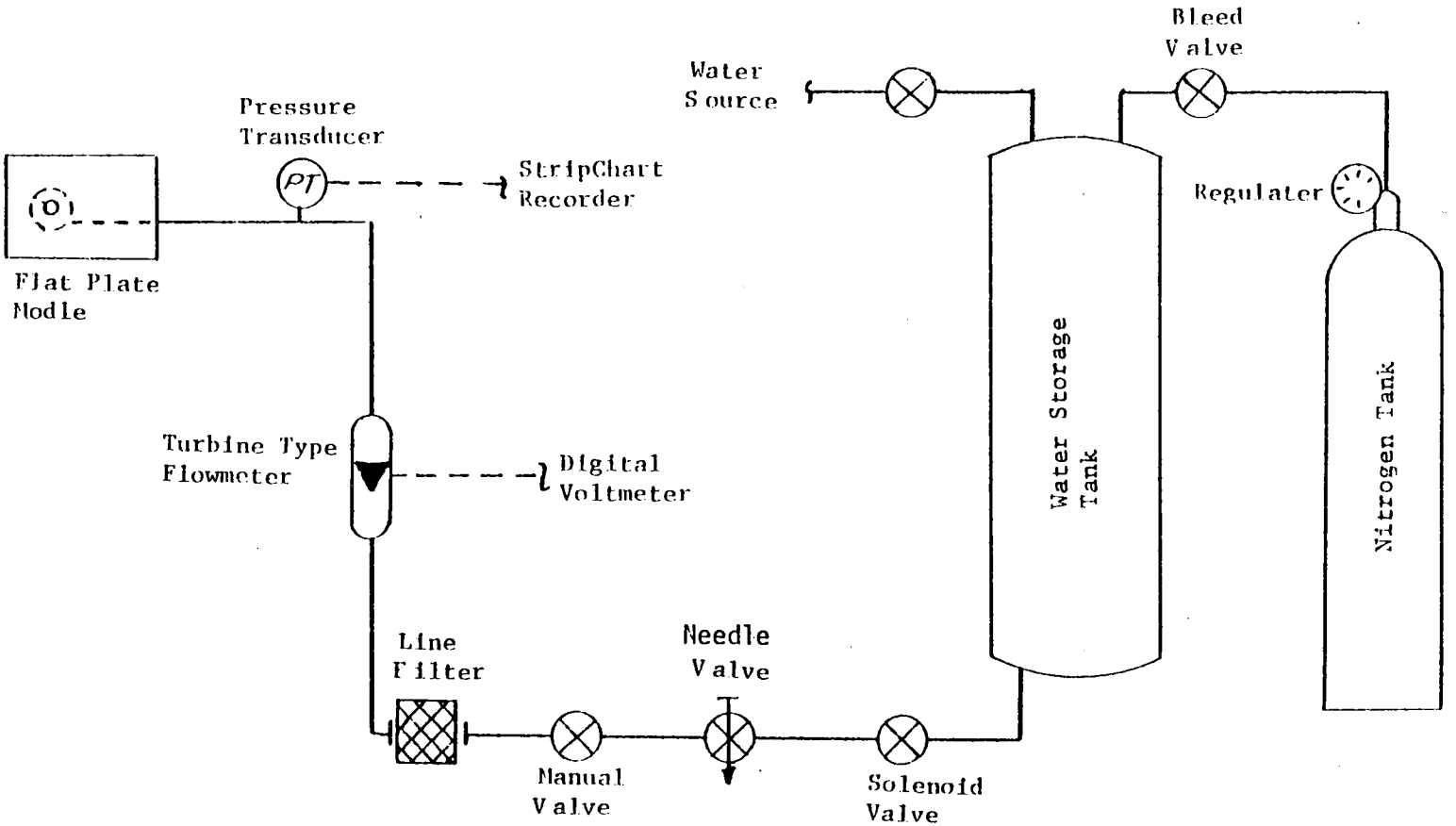

FIG. 5 SCHEMATIC OF THE LIQID INJECTION SYSTEM

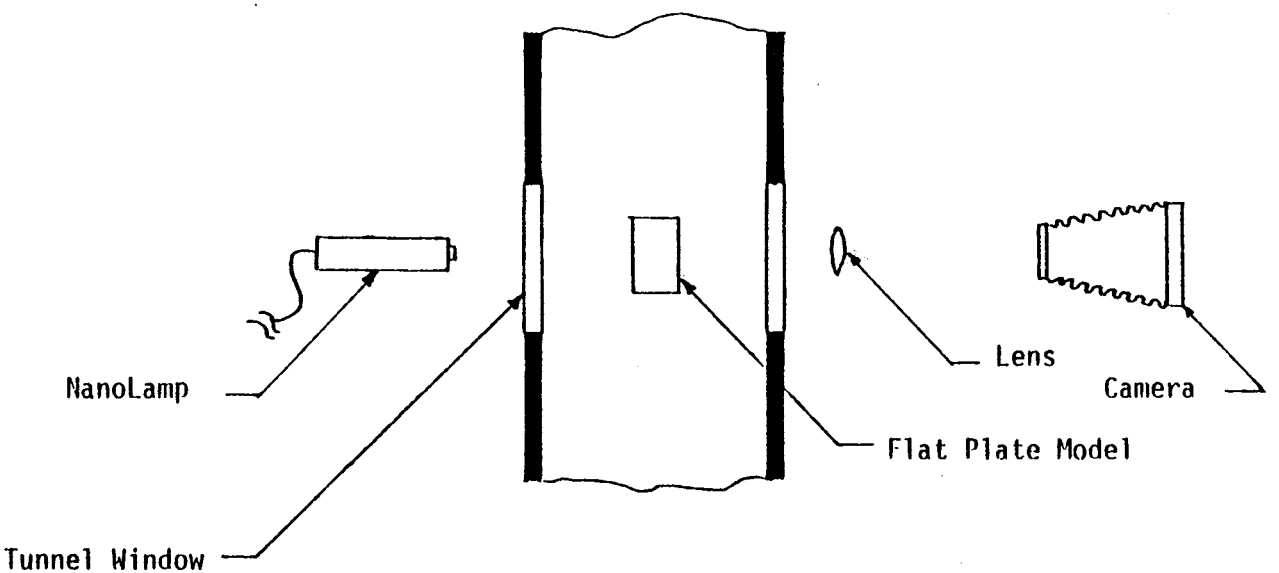

FIG. 6 SEHEMATIC OPTICAL SETUP FOR STOP ACTION PICTURES

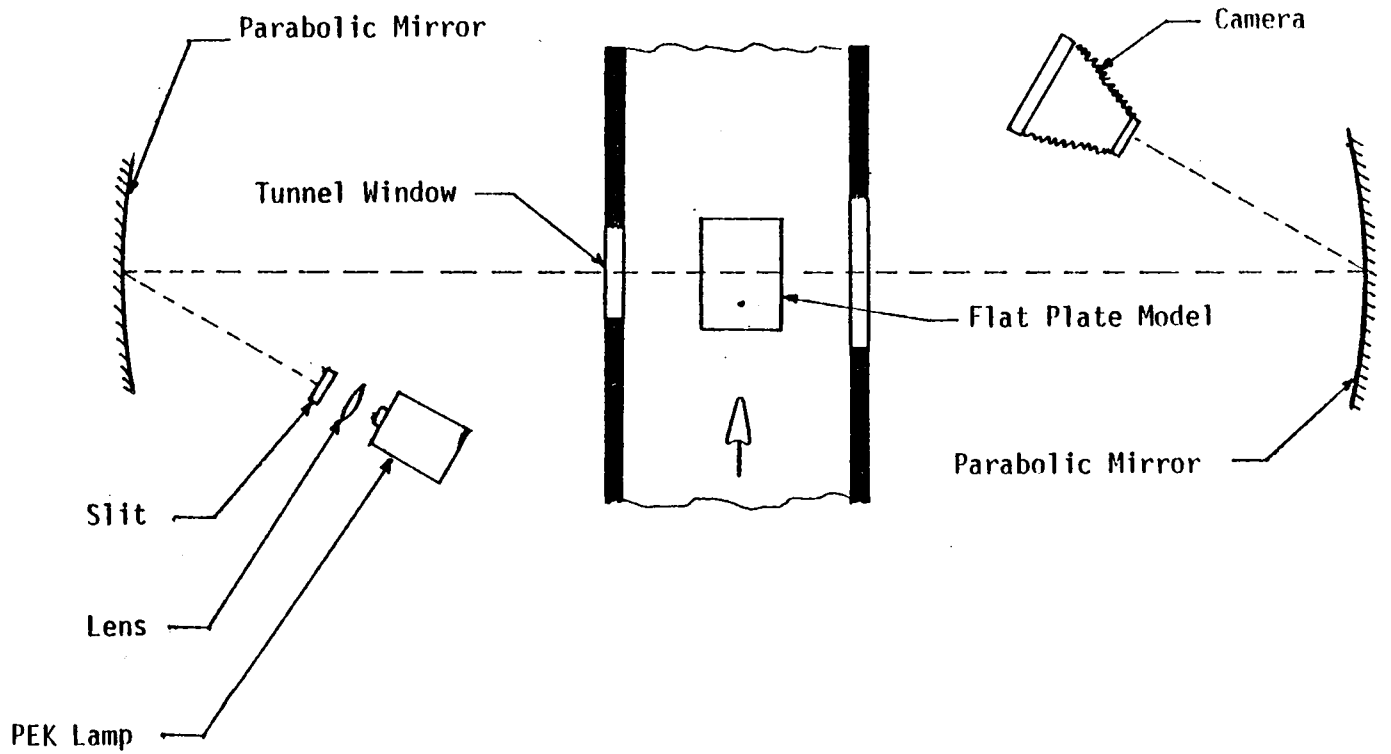

FIG. 7 SCHEMATIC OPTICAL SETUP FOR STREAK PICTURES

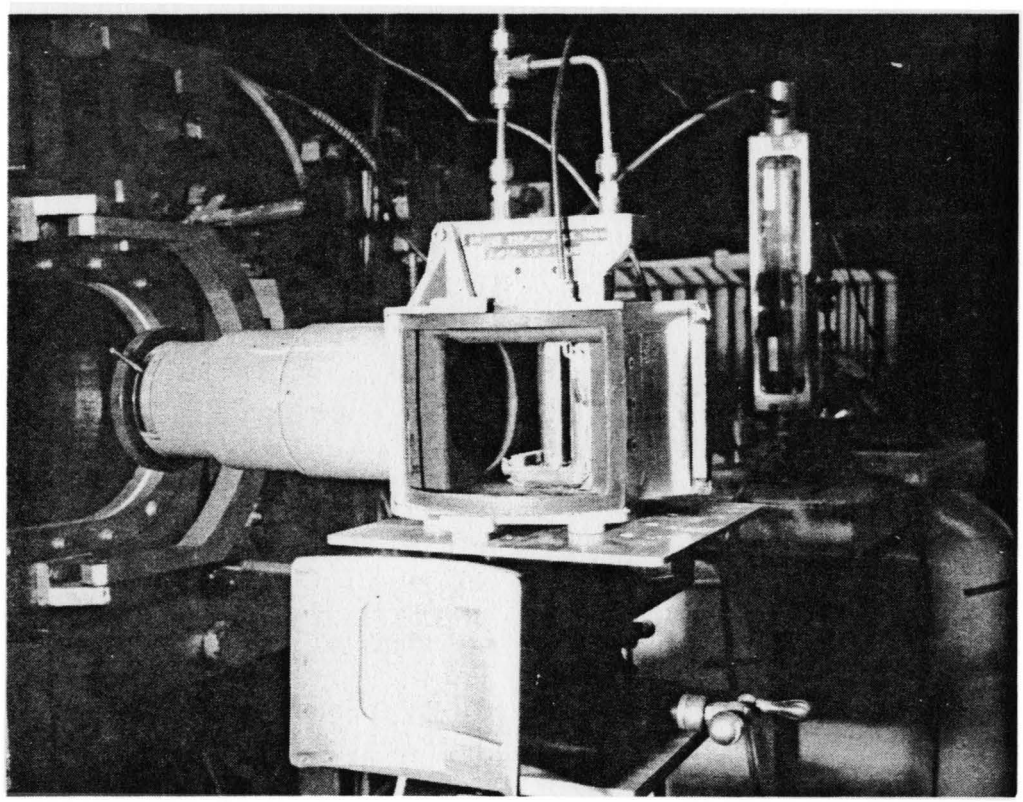

FIG. 8 PHOTOGRAPH OF ROTATING MIRROR CAMERA

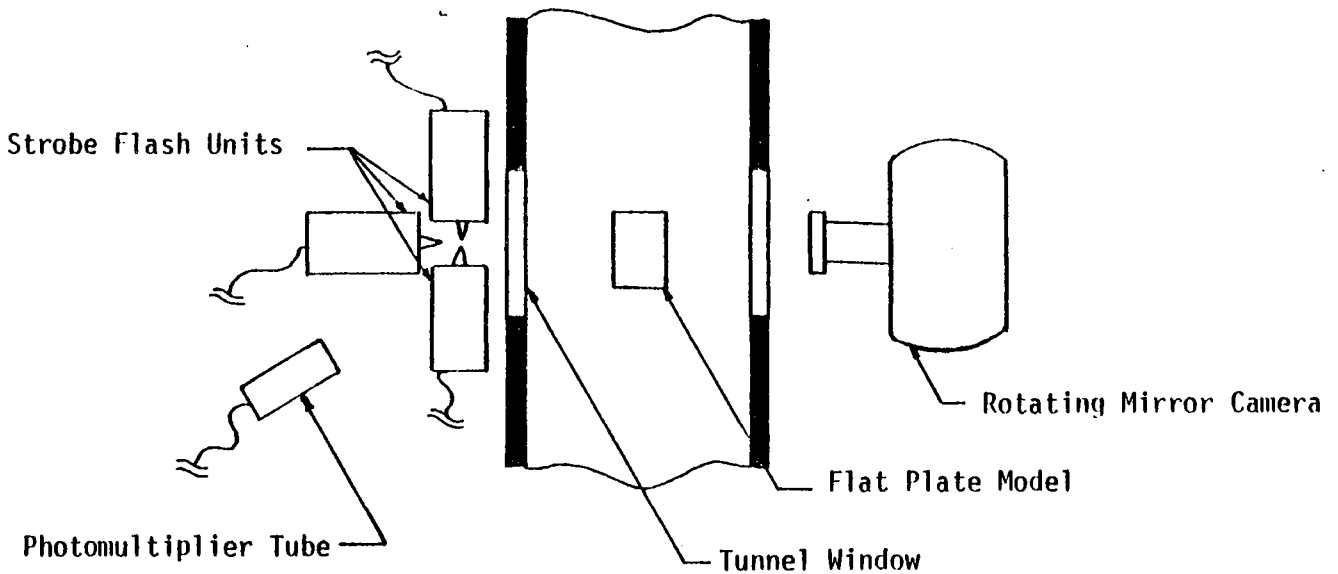

FIG. 9 LIGHTING ARRANGEMENT FOR ROTATING MIRROR CAMERA PICTURES

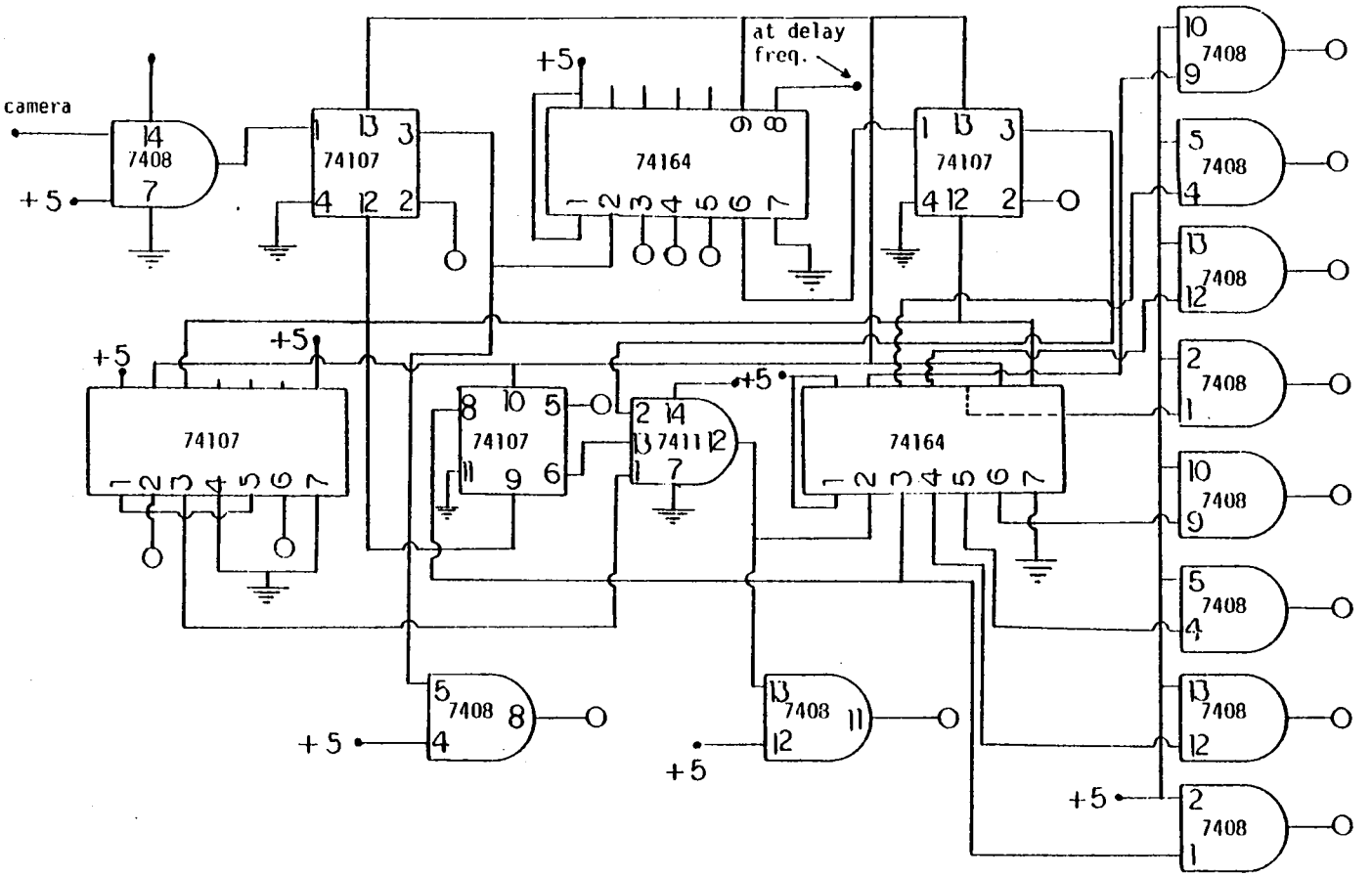

Fig. 10 SCHEMATIC OF THE (TTL) TRIGGERING CIRCUIT

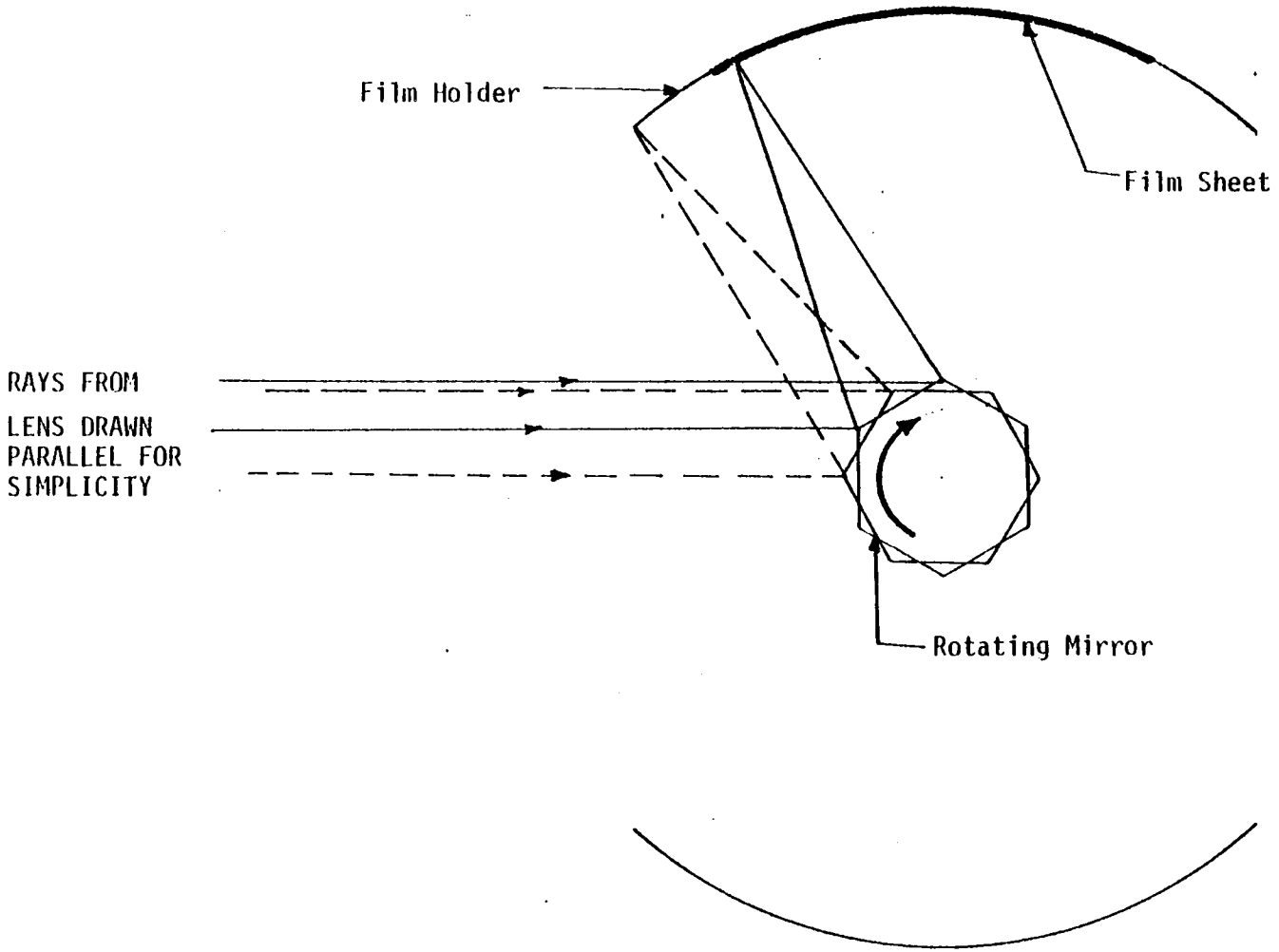

FIG. 11 OPTICS DIAGRAM SHOWING SYNCHRONIZATION TIME NECESSARY

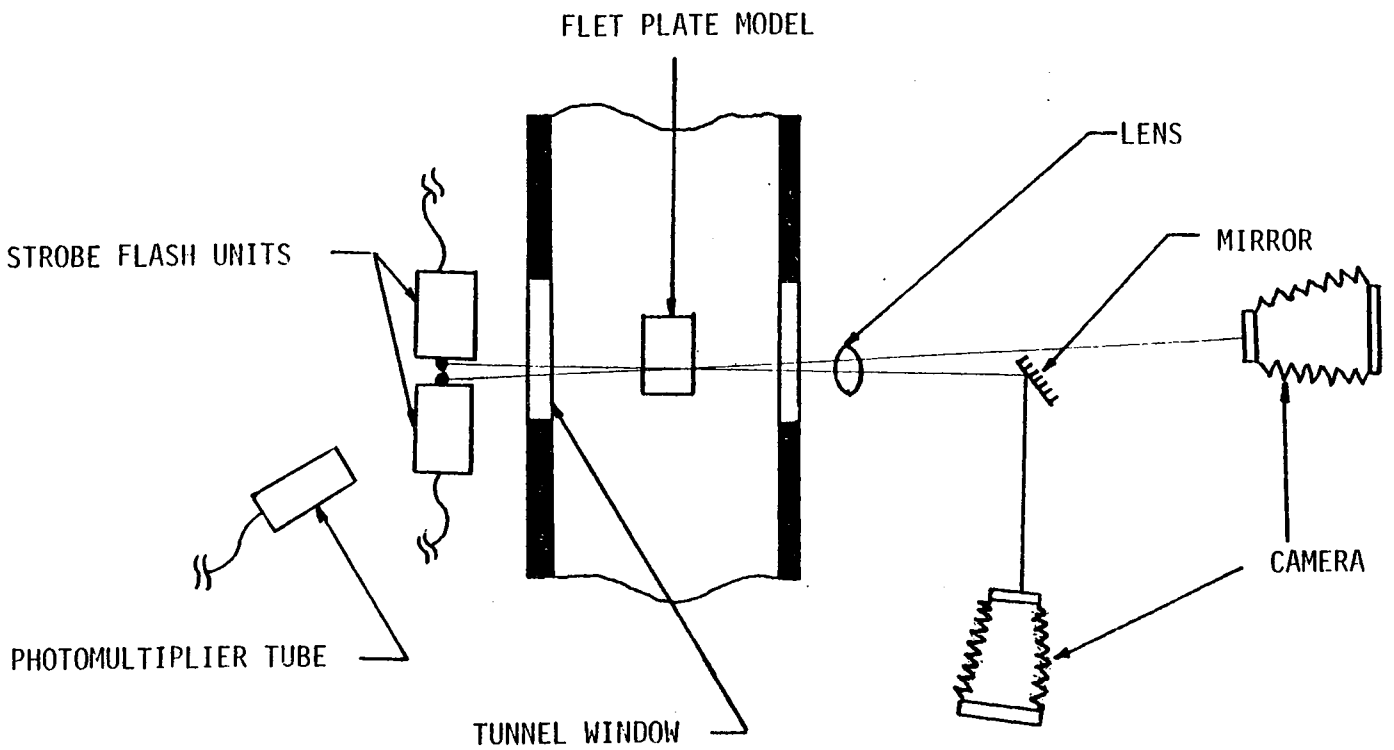

Fig. 12 SCHEMATIC OF MULTI EXPOSURE (FIXED MIRROR) SETUP

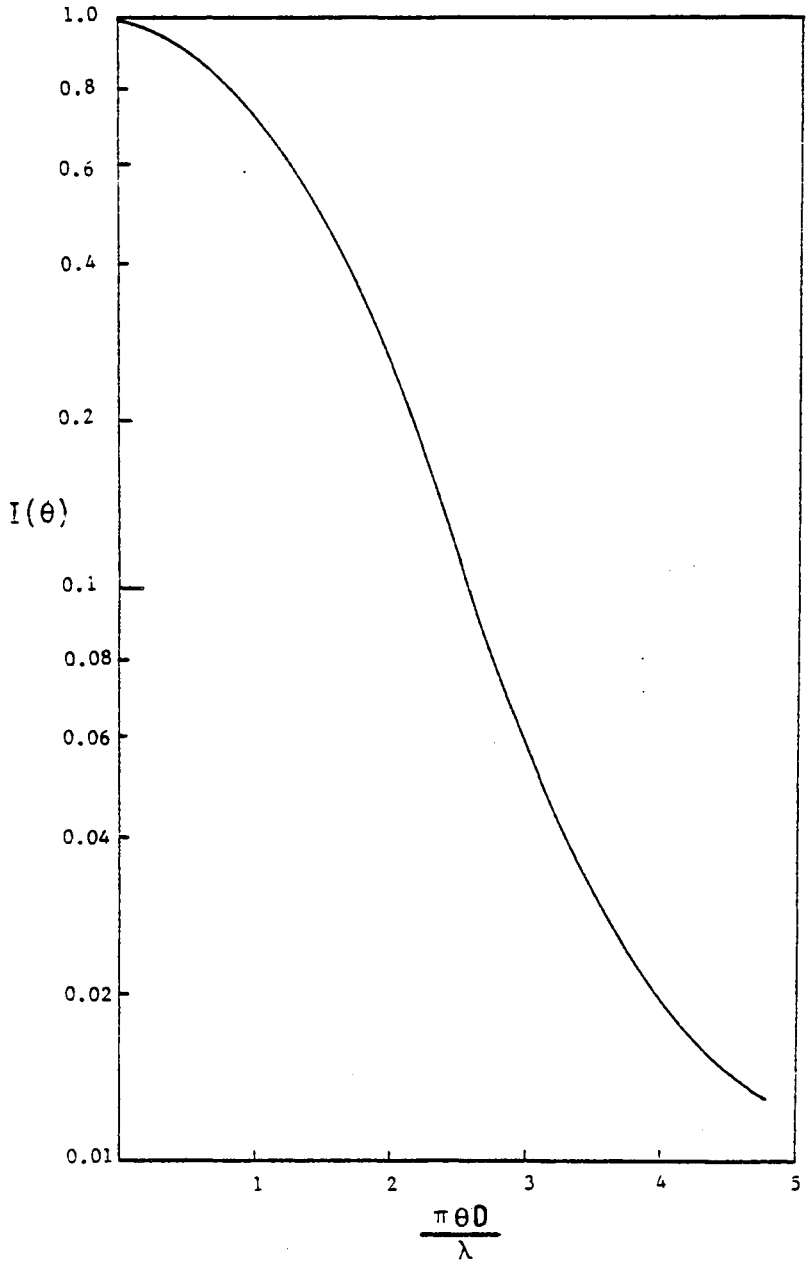

Fig. 13 MEAN THEORETICAL ILLUMINATION PROFILE

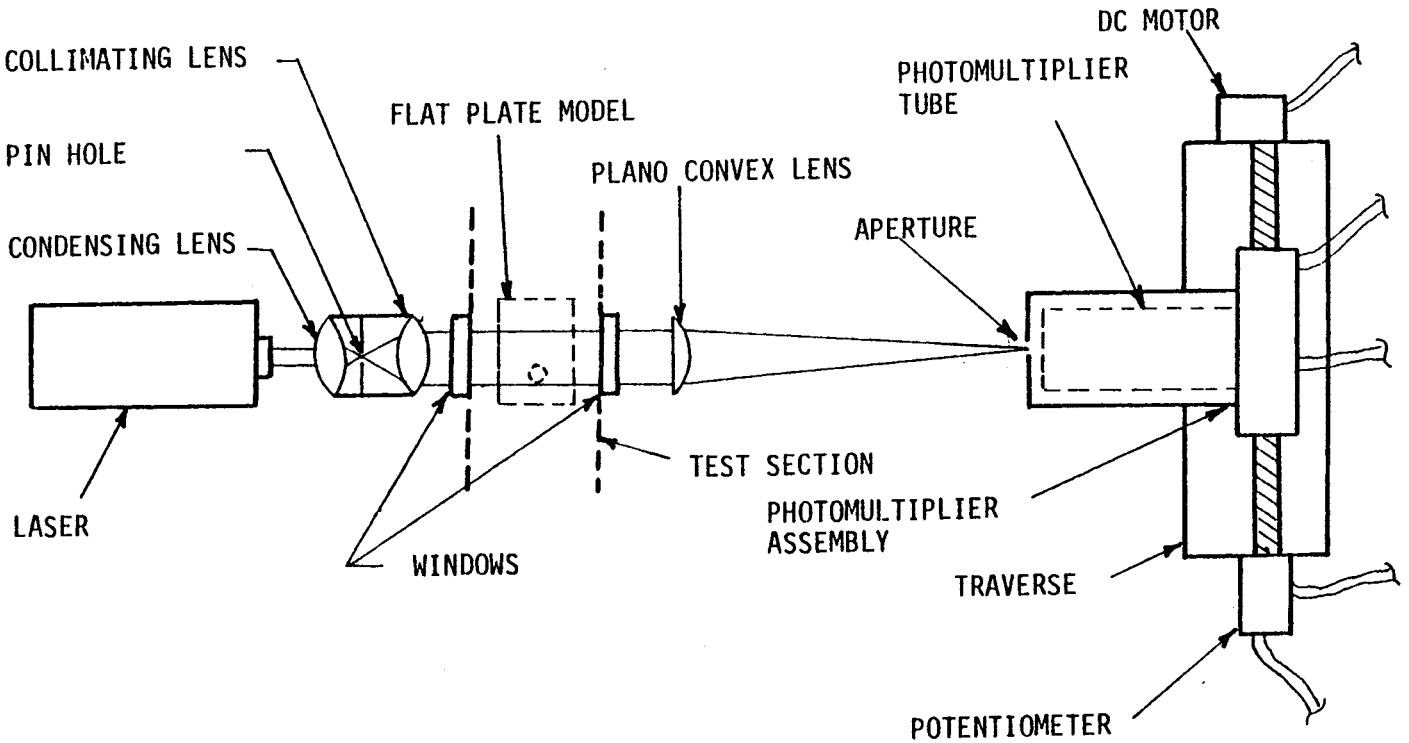

FIG. 14 SCHEMATIC OF LIGHT SCATTERING OPTICAL SETUP

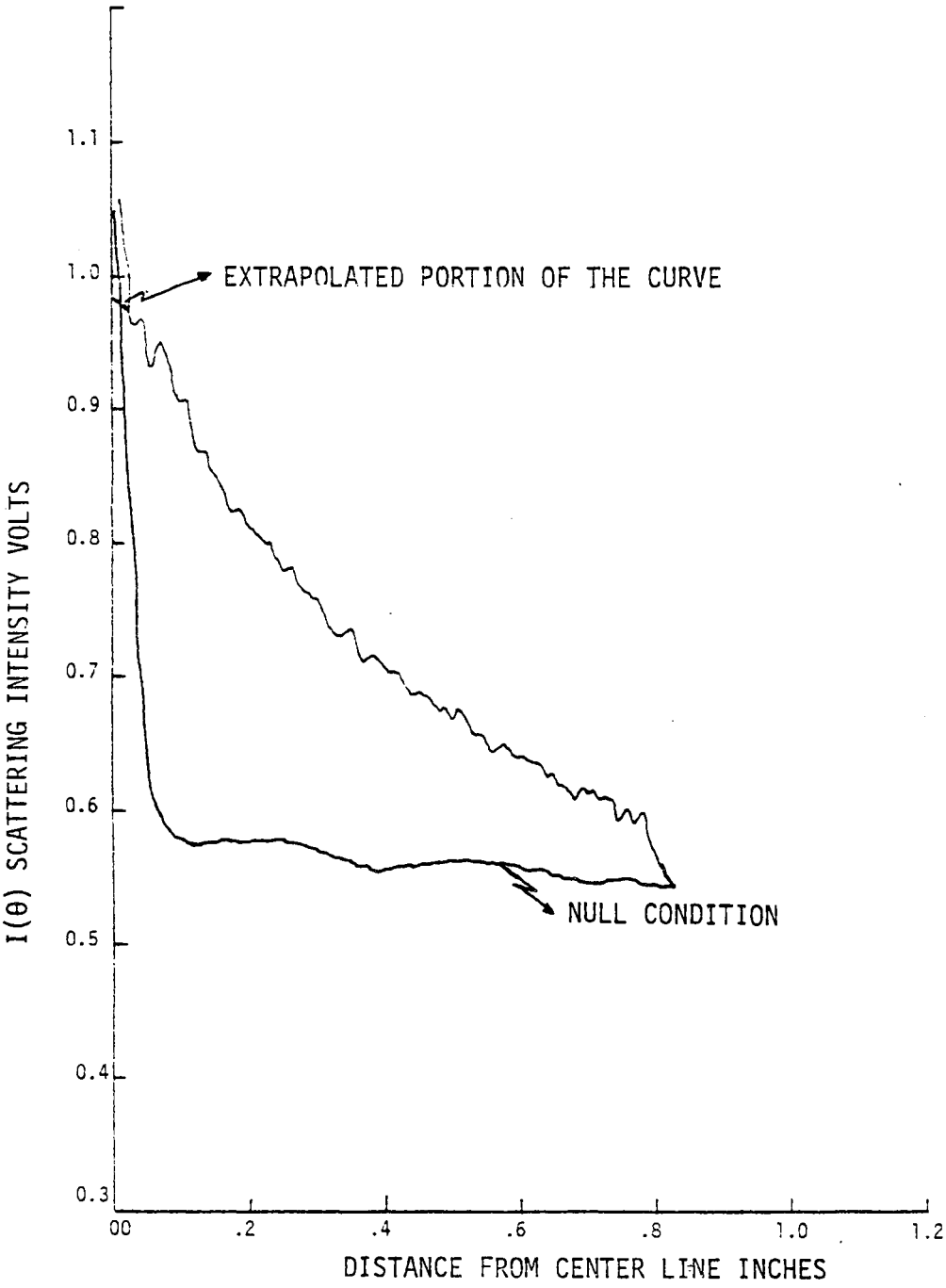

FIG. 15 TYPICAL SCATTERING INTENSITY SIGNAL

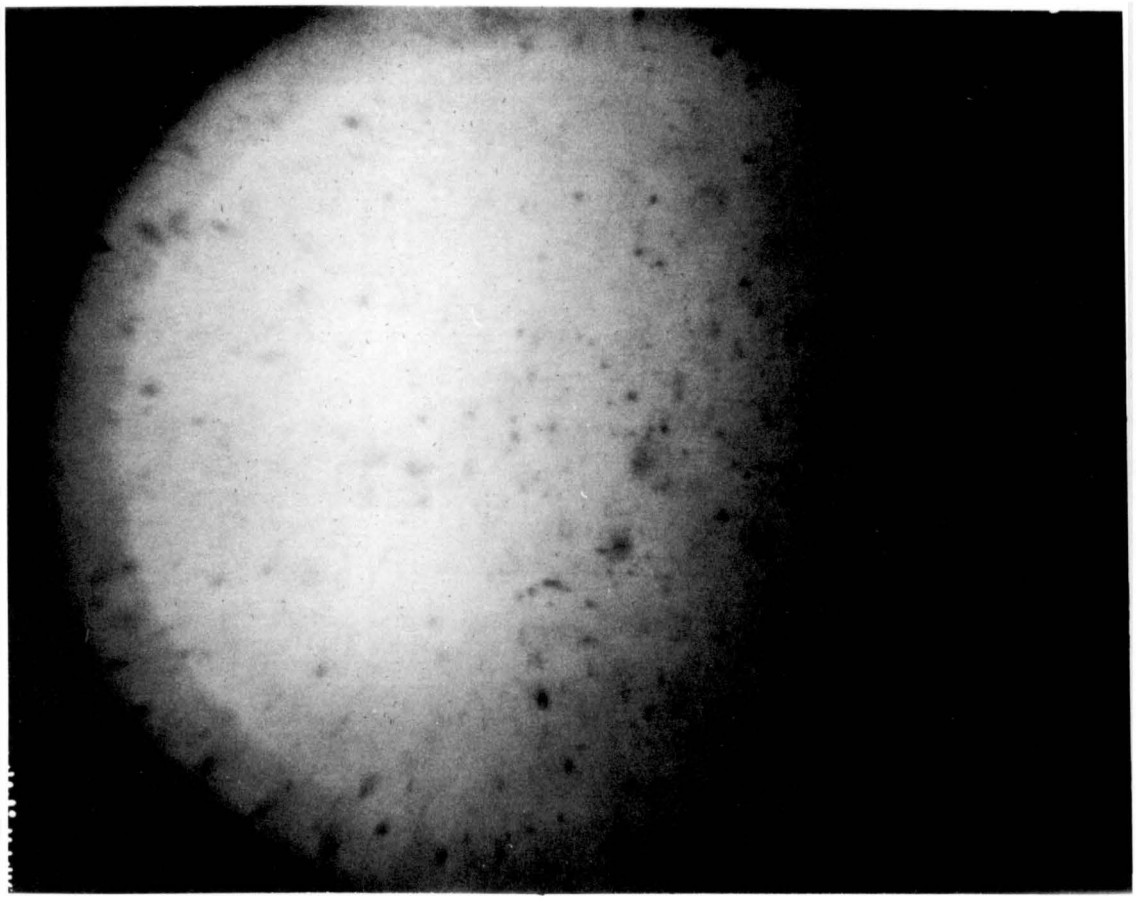

Fig. 16: High Magnification Photograph of Spray Particles in Mach 3 Crossflow.

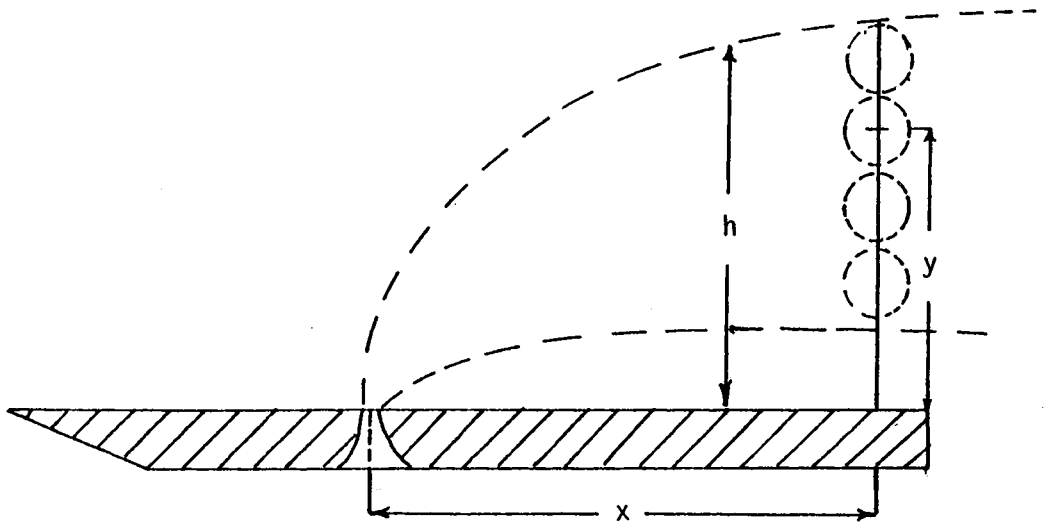

Fig. 17 SCHEMATIC OF BEAM LOCATION IN THE PLUME

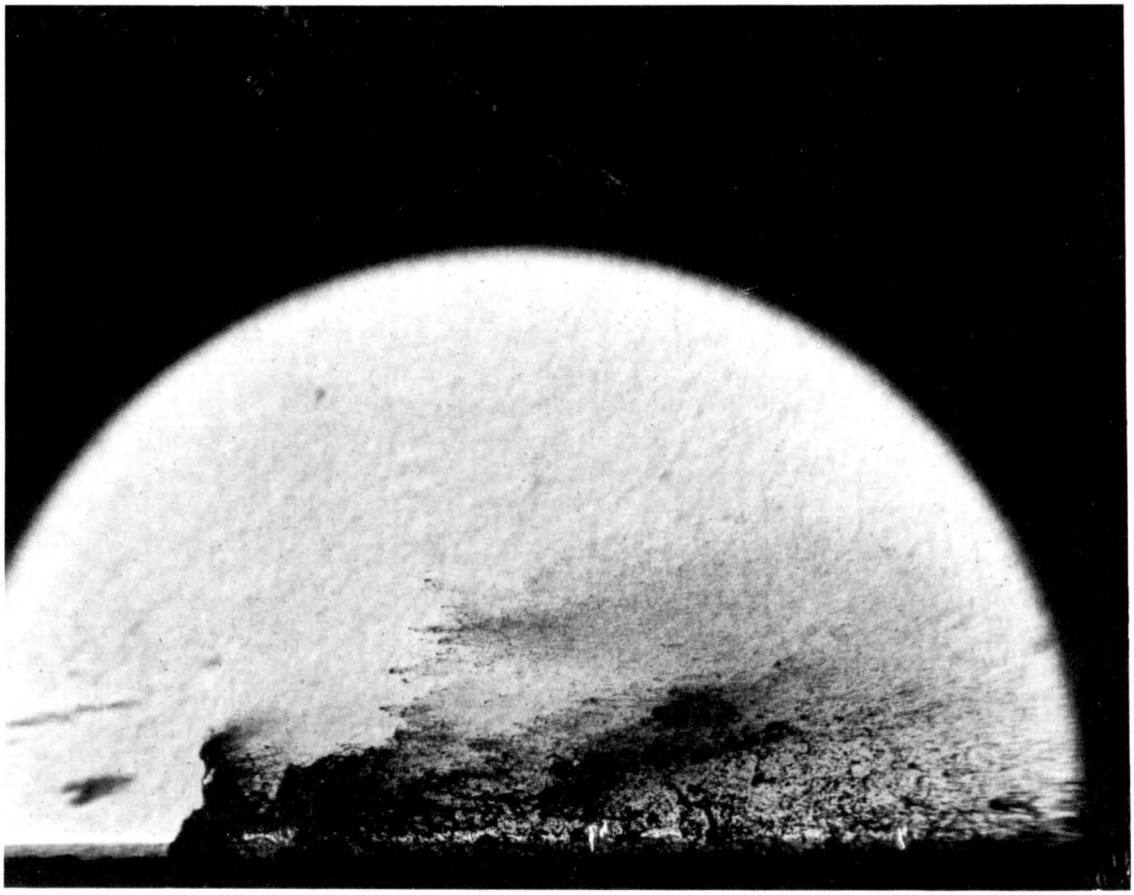

Fig. 18: Spray Plume in Mach 3 Crossflow.

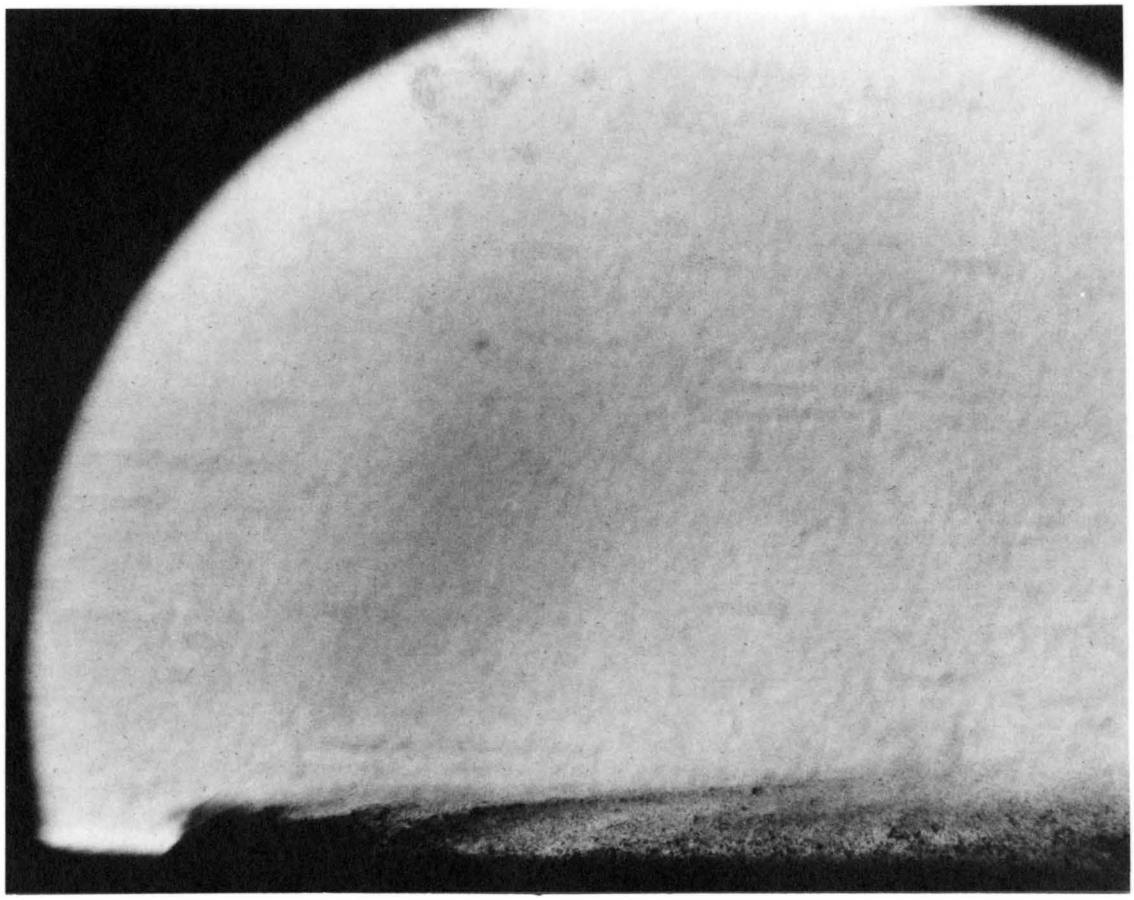

Fig. 19: Example of Regime 1 Injection, Fluorinert.

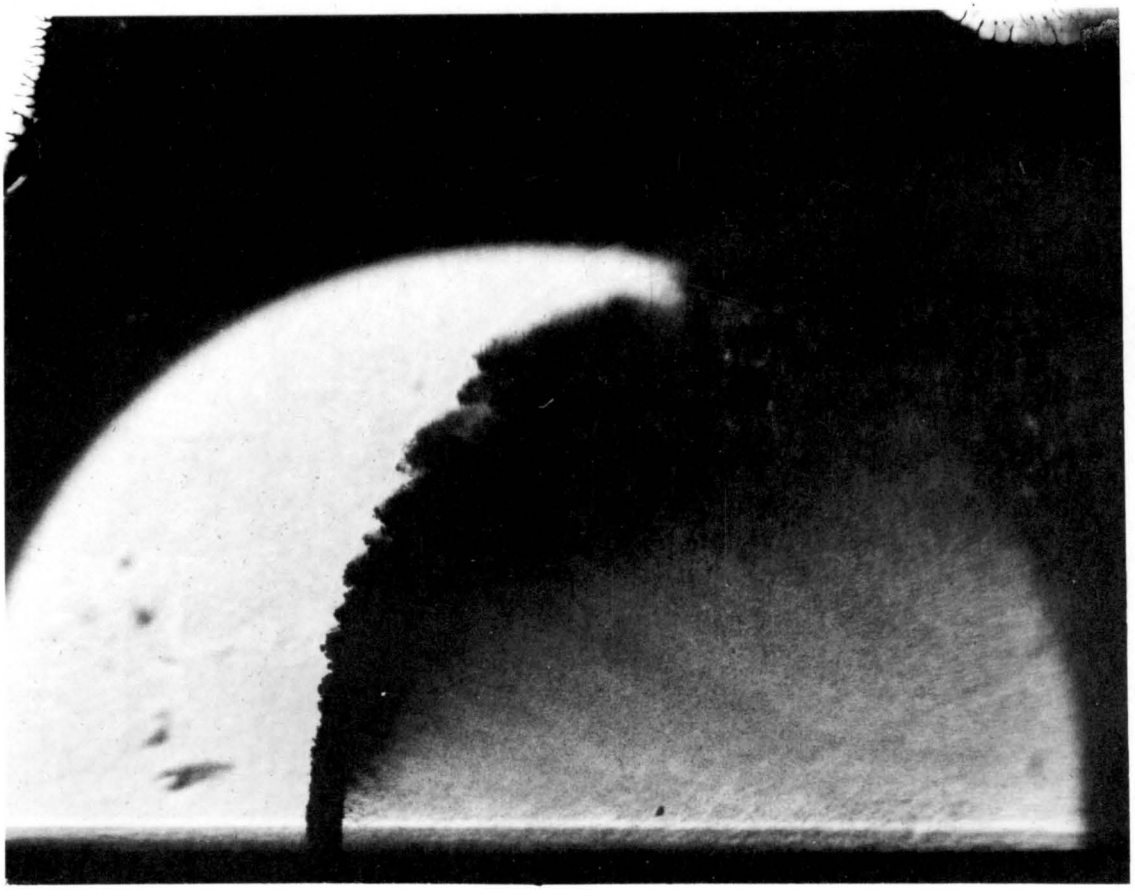

Fig. 20: Example of Regime 2 Injection, Water/Alcohol.

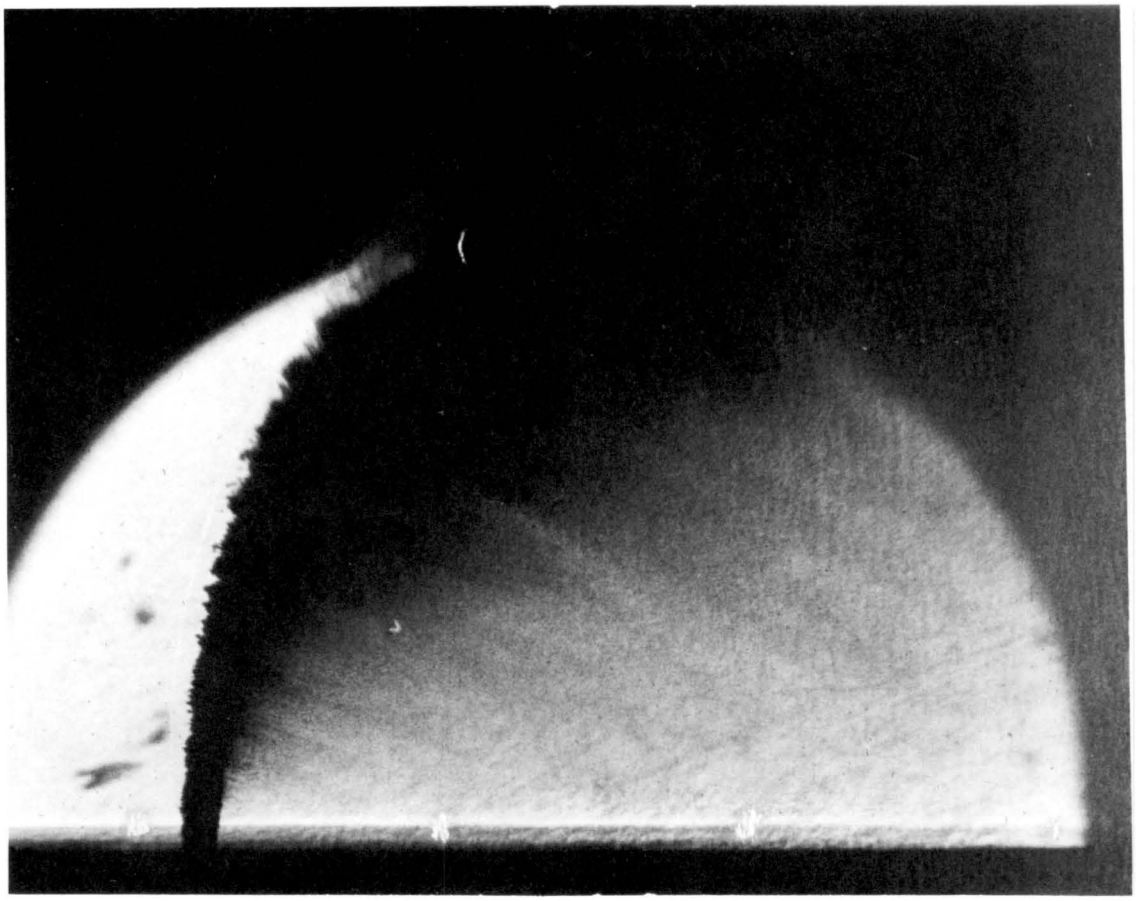

Fig. 21: Example of Regime 3 Injection, Water/Alcohol.

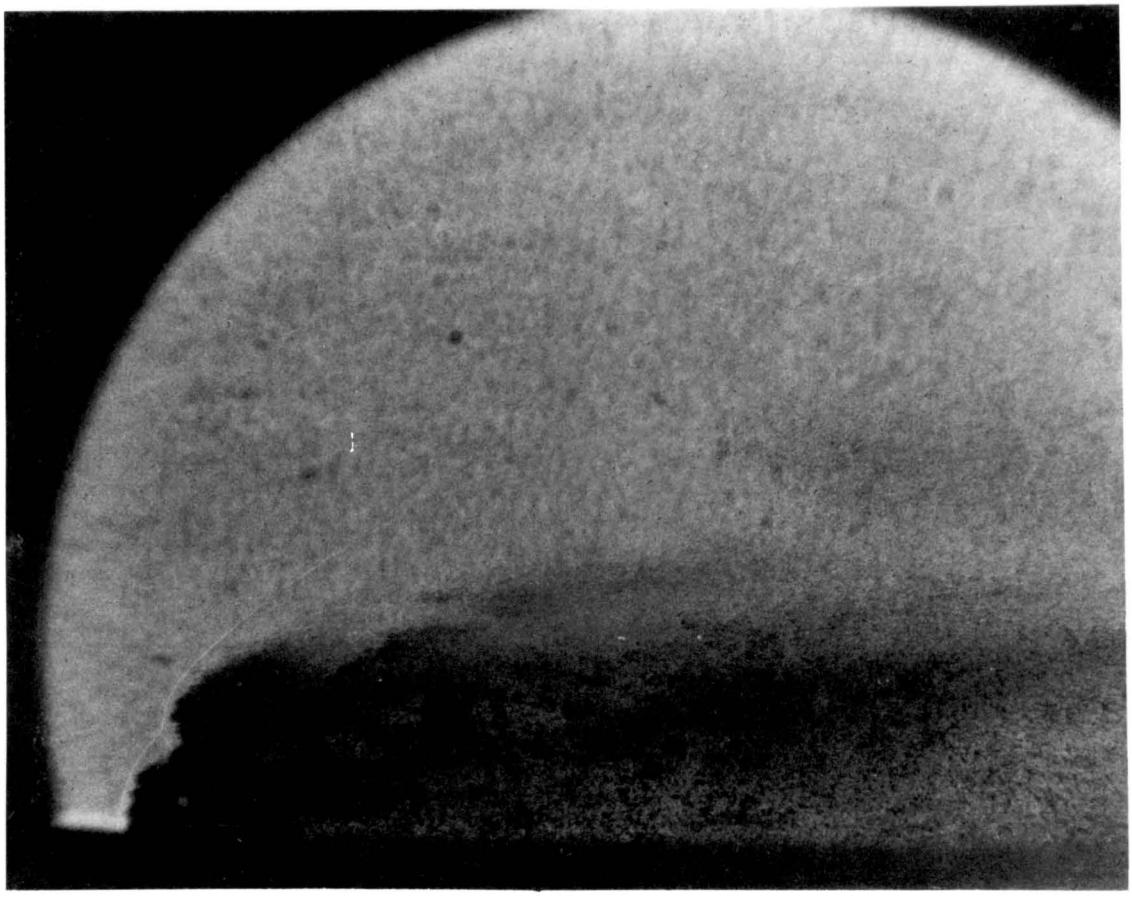

Fig. 22a: Regime 1 Injection

Water

μ = 1.0 Centipoise

σ = 73.0 dyne/cm.

$\bar{q}$ = 2

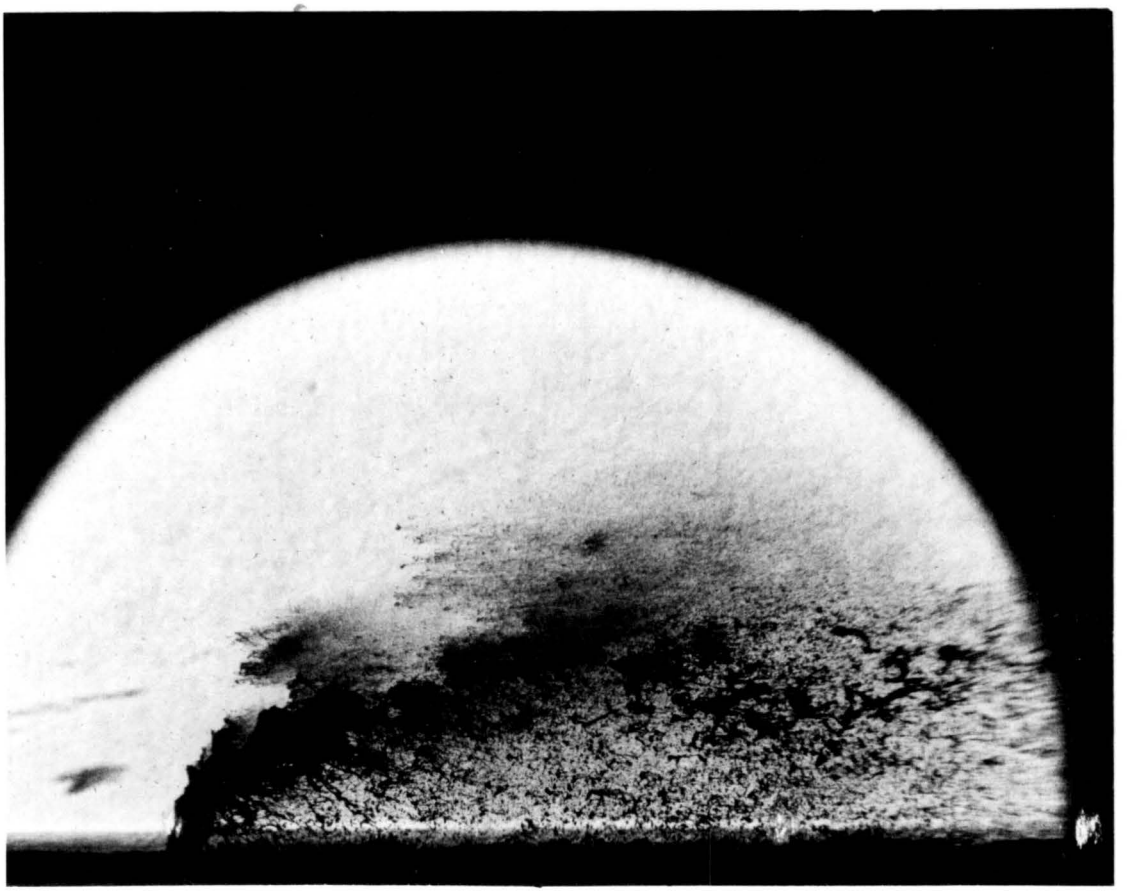

Fig. 22b: Regime 1 Injection

Water/Glycerine

μ = 10.5 Centipoise

σ = 73.0 dyne/cm.

$\bar{q}$ = 2

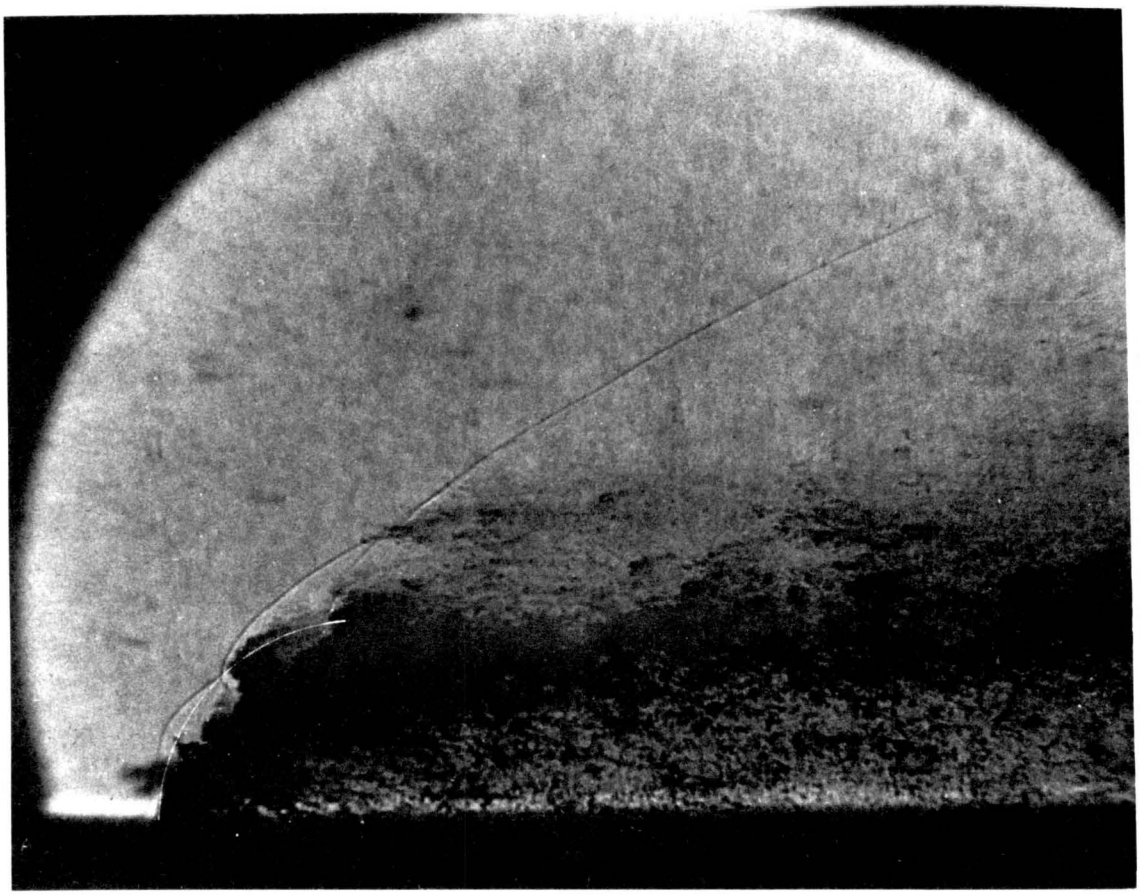

Fig. 22c: Regime 1 Injection

Water/Glycerine

μ = 18.4 Centipoise

σ = 73.0 dyne/cm.

$\bar{q}$ = 2

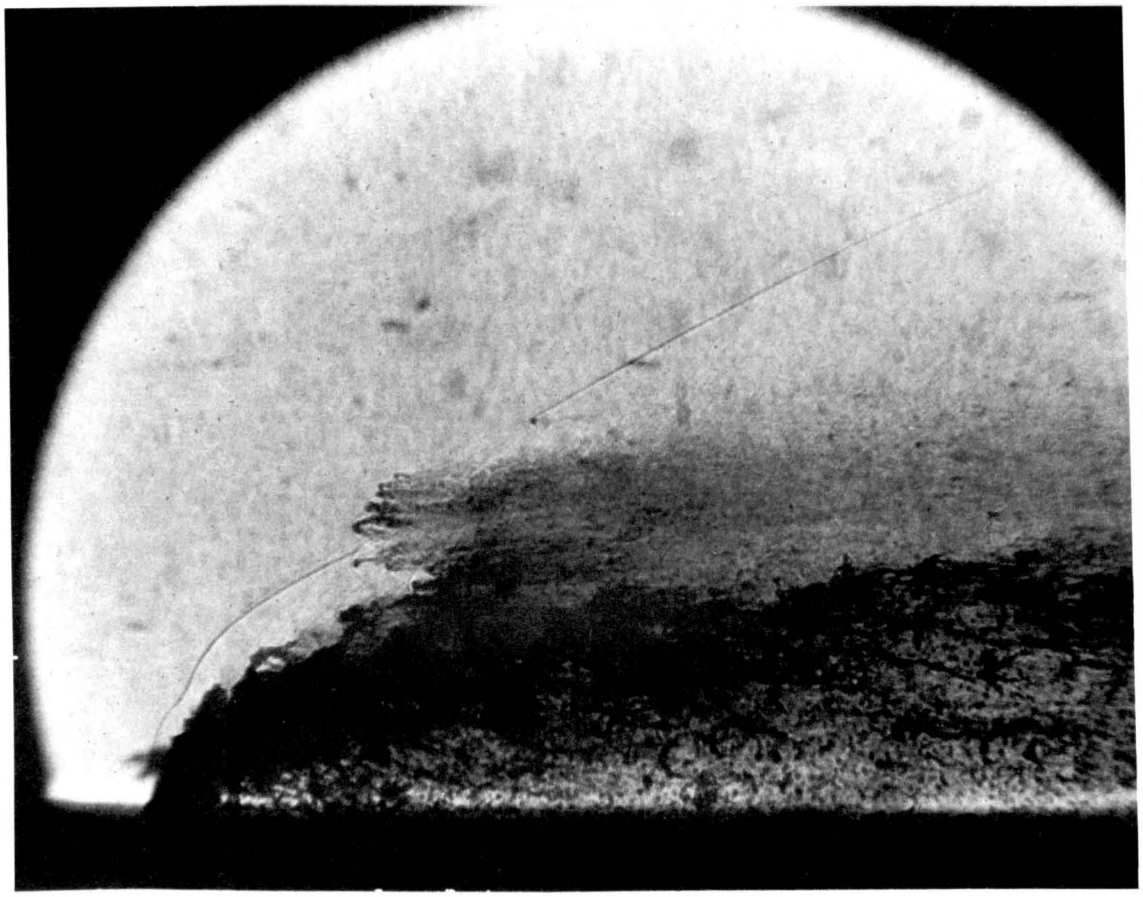

Fig. 22d: Regime 1 Injection

Water/Glycerine

μ = 27.6 Centipoise

σ = 73.0 dyne/cm.

$\bar{q}$ = 2

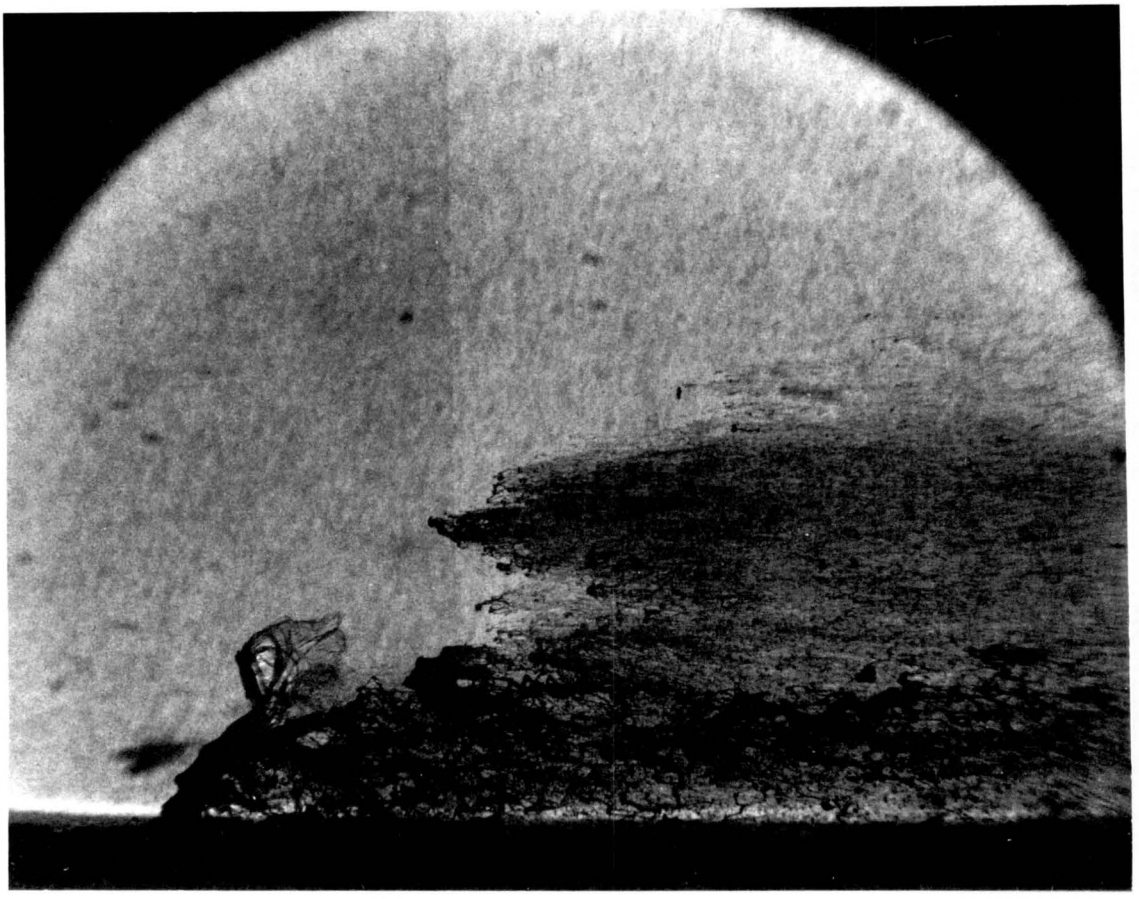

Fig. 22e: Regime 1 Injection

Water/Glycerine

μ = 40.5 Centipoise

σ = 73.0 dyne/cm.

$\bar{q}$ = 2

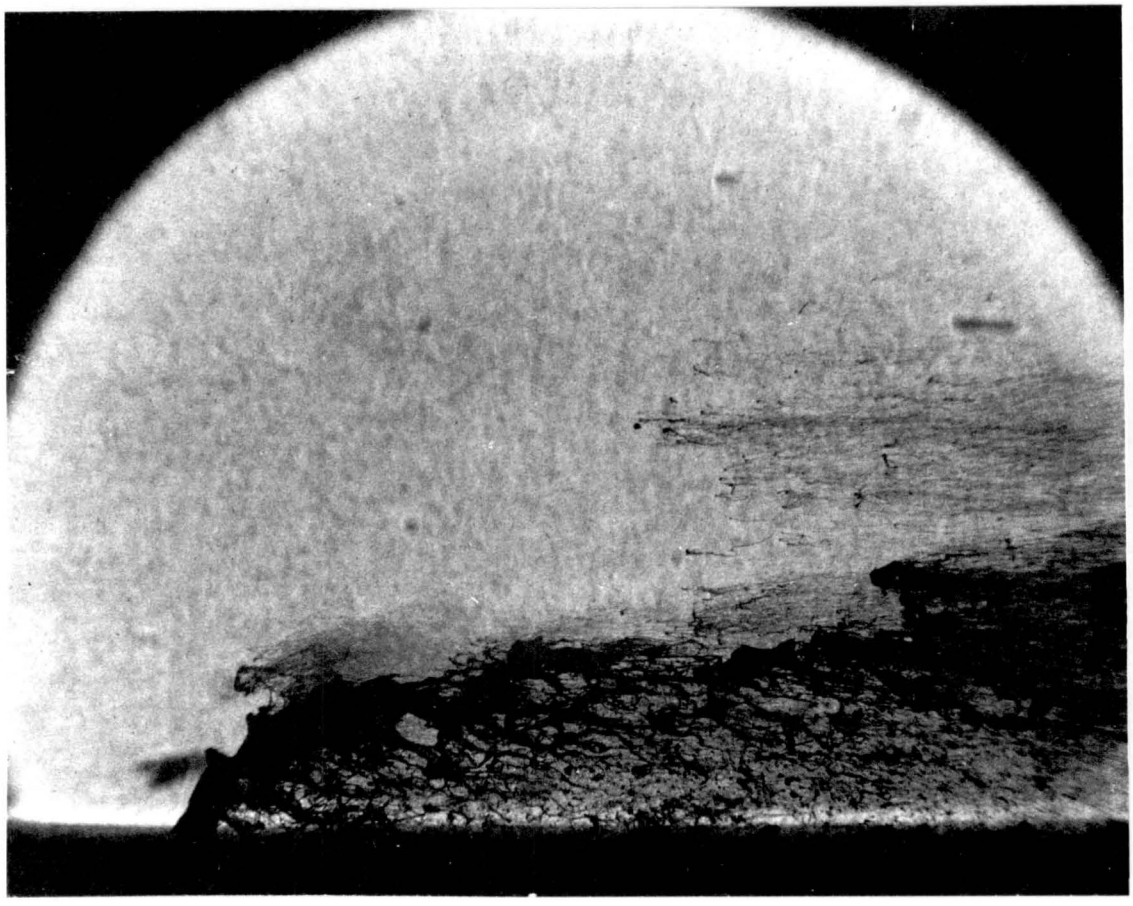

Fig. 22f: Regime 1 Injection

Water/Glycerine

μ = 59.3 Centipoise

σ = 73.0 dyne/cm.

$\bar{q}$ = 2

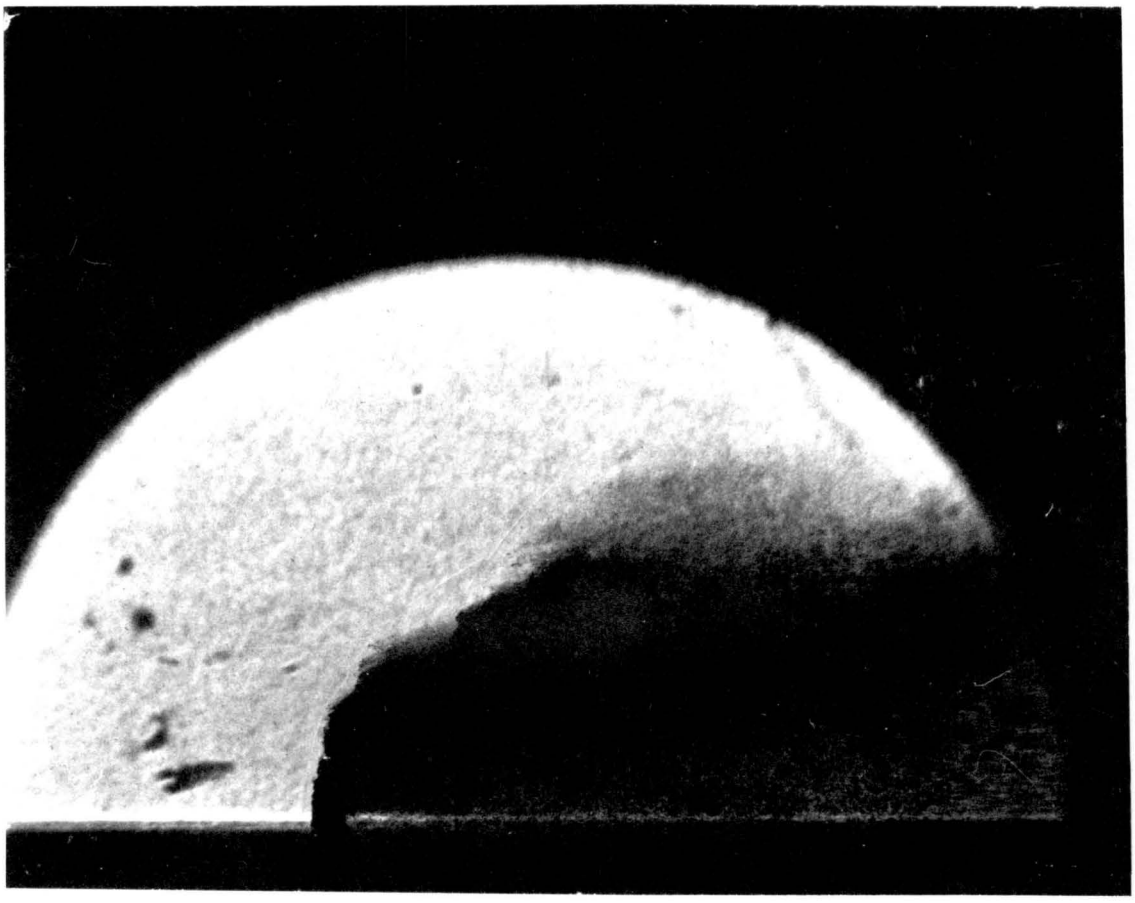

Fig. 22g: Regime 1 Injection

Water/Alcohol

μ = 1.0 Centipoise

σ = 33.5 dyne/cm.

$\bar{q}$ = 2

Fig. 22h: Regime 1 Injection

Flourinert

μ = 1.5 Centipoise

σ = 1 5 dyne/cm.

$\bar{\bar{q}}$ = 2

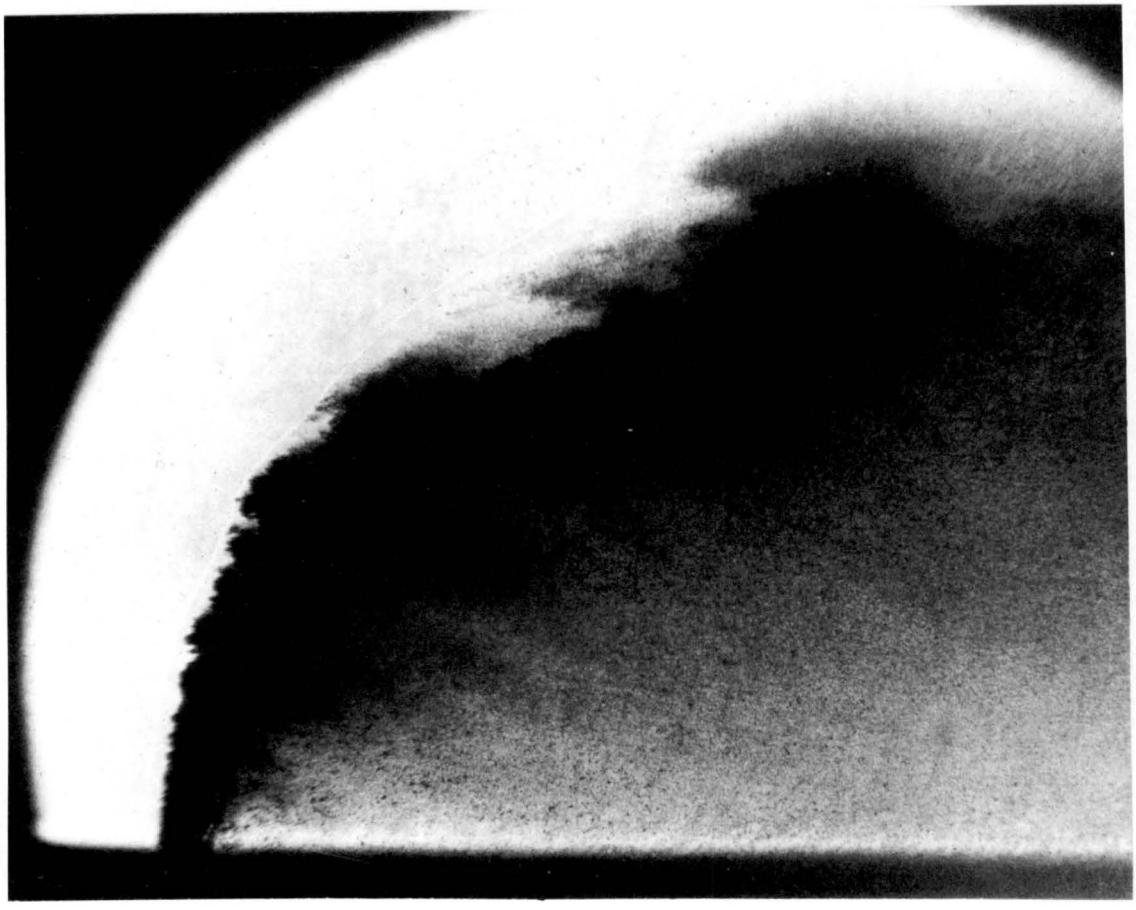

Fig. 23a: Regime 2 Injection

Water

μ = 1.0 Centipoise

σ = 73.0 dyne/cm.

$\bar{q}$ = 8

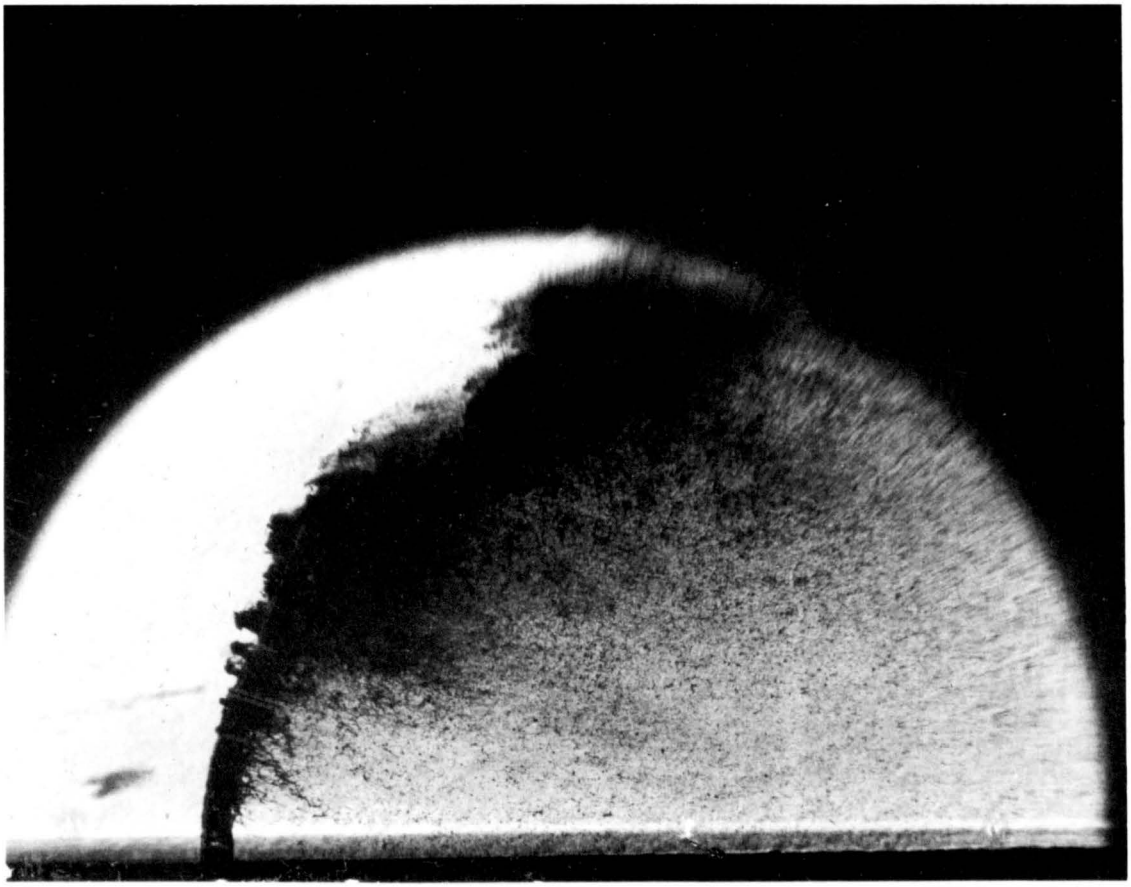

Fig. 23b: Regime 2 Injection

Water/Glycerine

μ = 10.5 Centipoise

σ = 73.0 dyne/cm.

$\bar{q}$ = 8

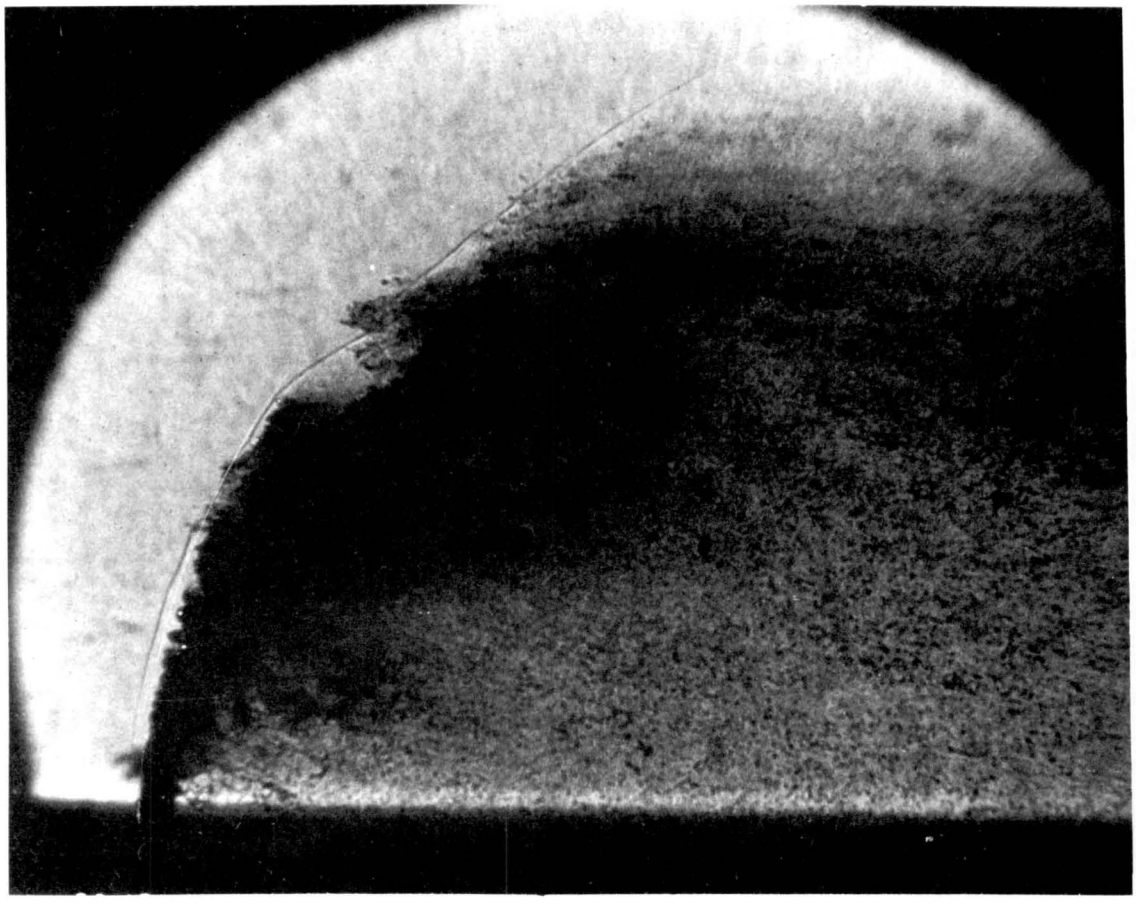

Fig. 23c: Regime 2 Injection

Water/Glycerine

μ = 18.4 Centipoise

σ = 73.0 dyne/cm.

$\ddot{q}$ = 8

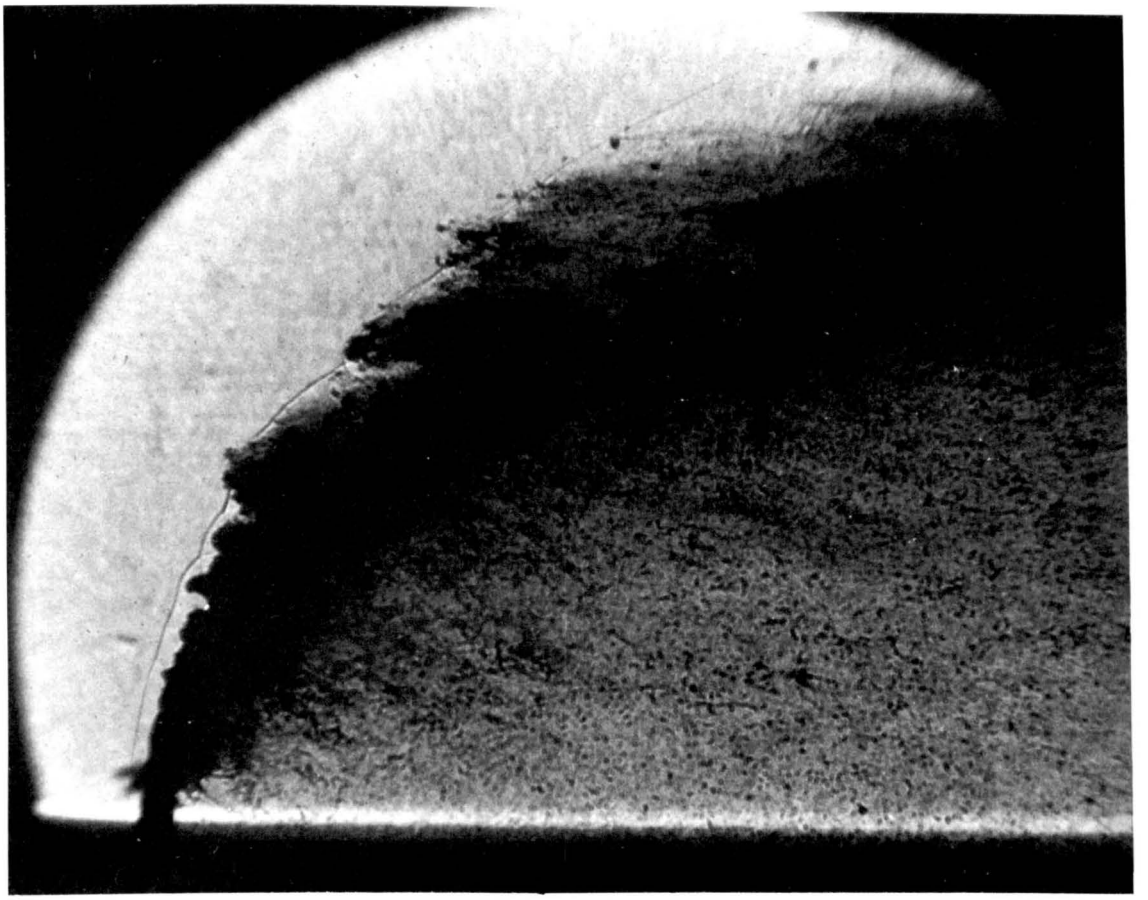

Fig. 23d. Regime 2 Injection

Water/Glycerine

μ = 27.6 Centipoise

σ = 73.0 dyne/cm.

$\bar{q}$ = 8

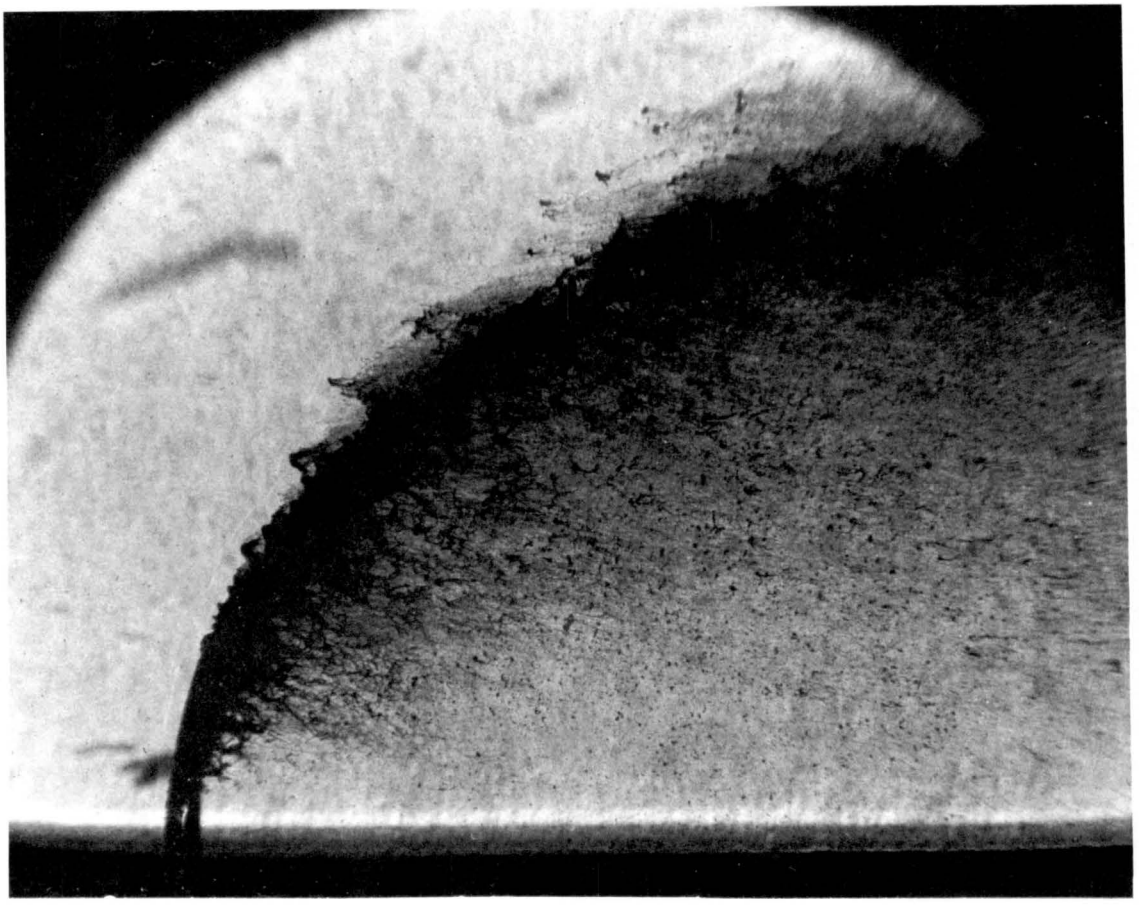

Fig. 23e: Regime 2 Injection

Water/Glycerine

μ = 40.5 Centipoise

σ = 73.0 dyne/cm.

$\bar{q}$ = 8

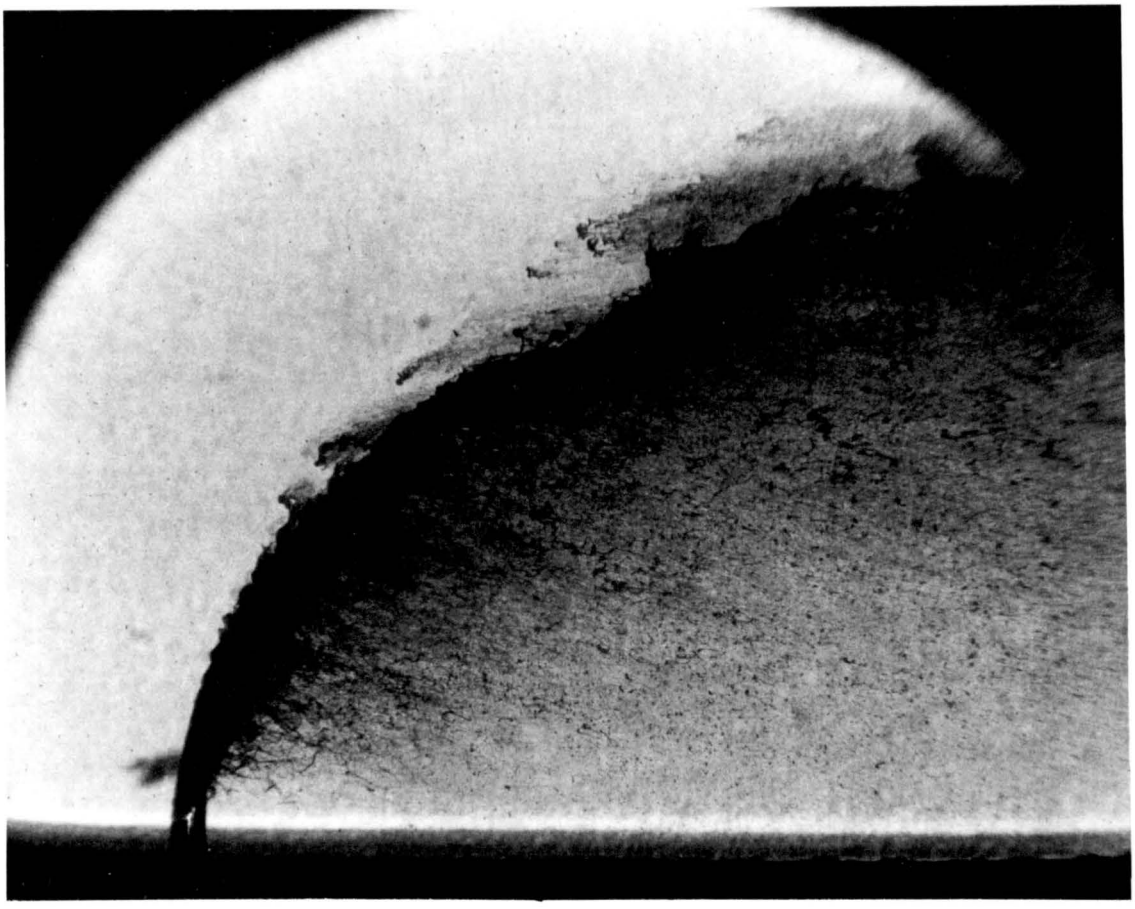

Fig. 23f: Regime 2 Injection

Water/Glycerine

μ = 59.8 Centipoise

σ = 73.0 dyne/cm.

$\bar{q}$ = 8

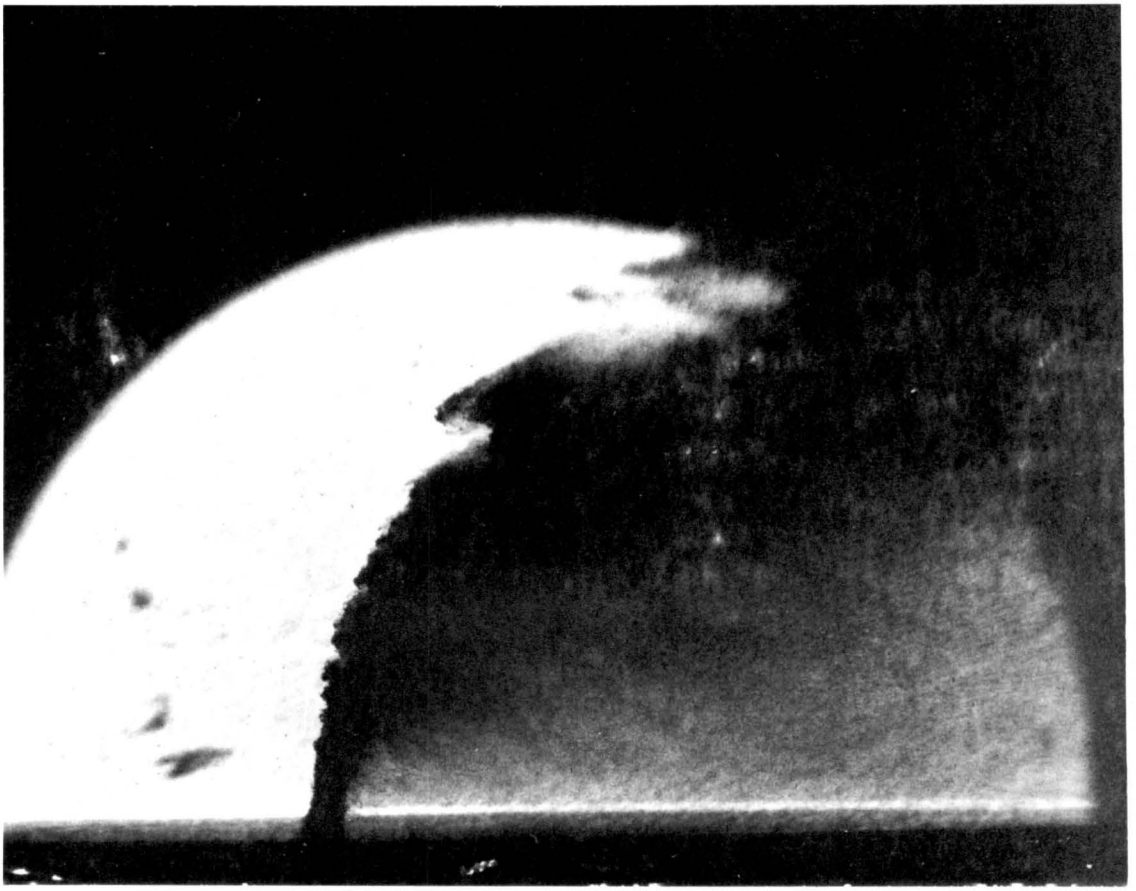

Fig. 23y: Regime 2 Injection

Water/Alcohol

μ = 1.0 Centipoise

σ = 33.5 dyne/cm.

$\bar{q}$ = 8

Fig. 23h: Regime 2 Injection

Fluorinert

μ = 1.5 Centipoise

σ = 15 dyne/cm.

$\bar{q}$ = 8

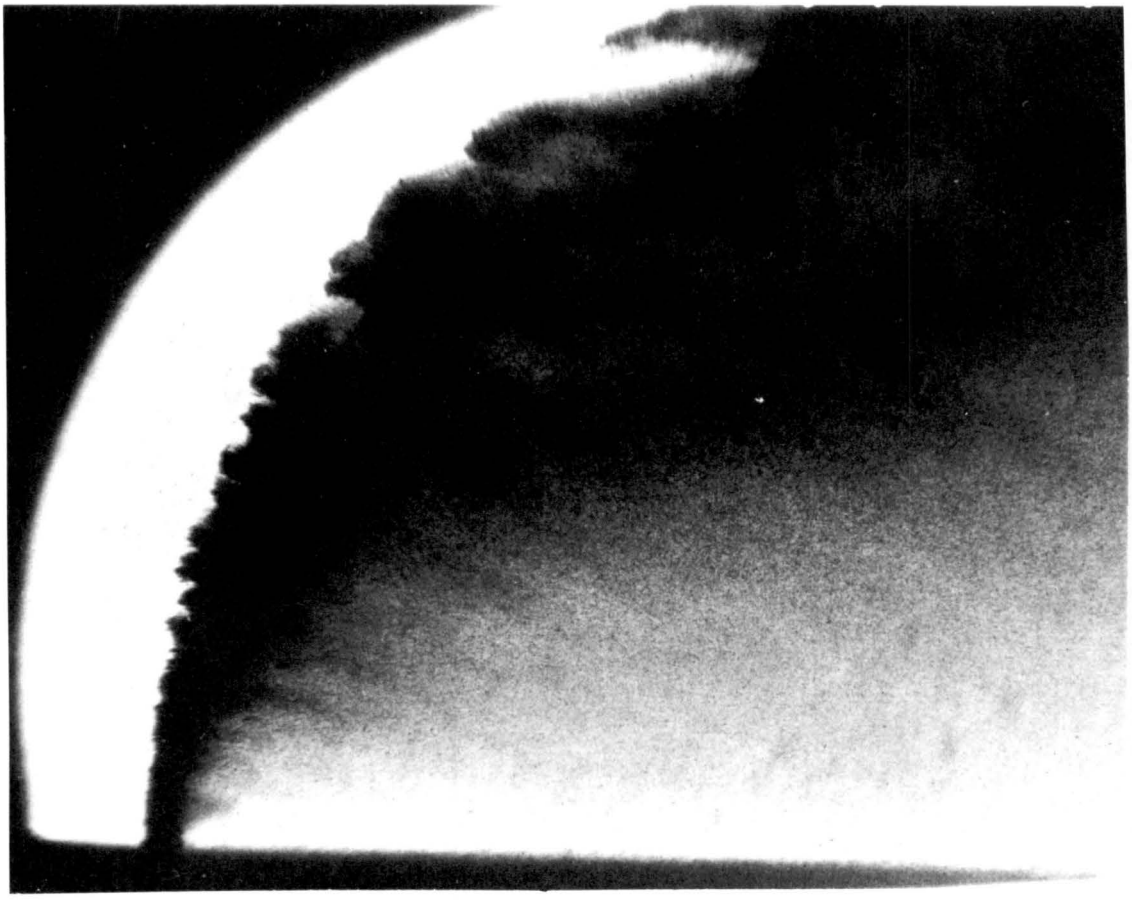

Fig. 24a: Regime 3 Injection

Water

μ = 1.0 Centipoise

σ = 73.0 dyne/cm.

$\bar{q}$ = 14

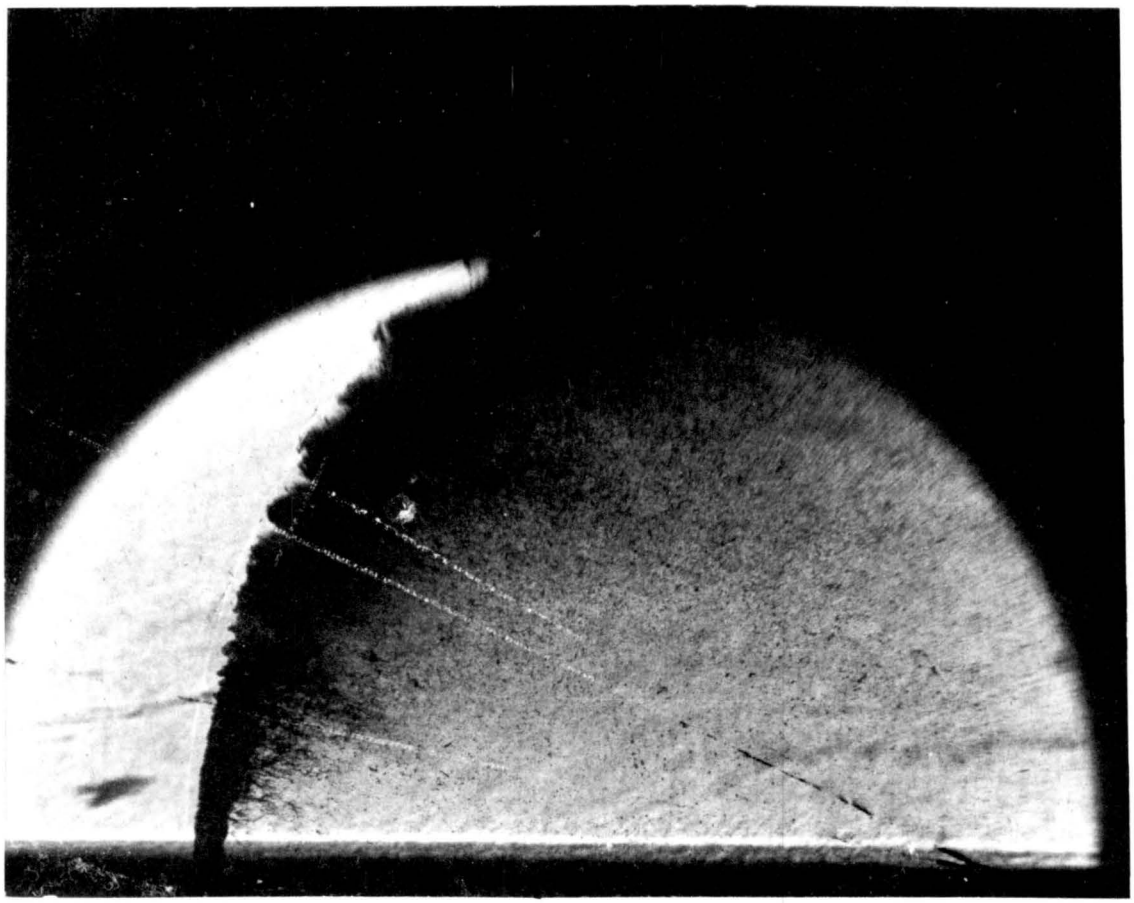

Fig. 24b: Regime 3 Injection

Water/Glycerine

μ = 10.5 Centipoise

σ = 73.0 dyne/cm.

$\bar{q}$ = 14

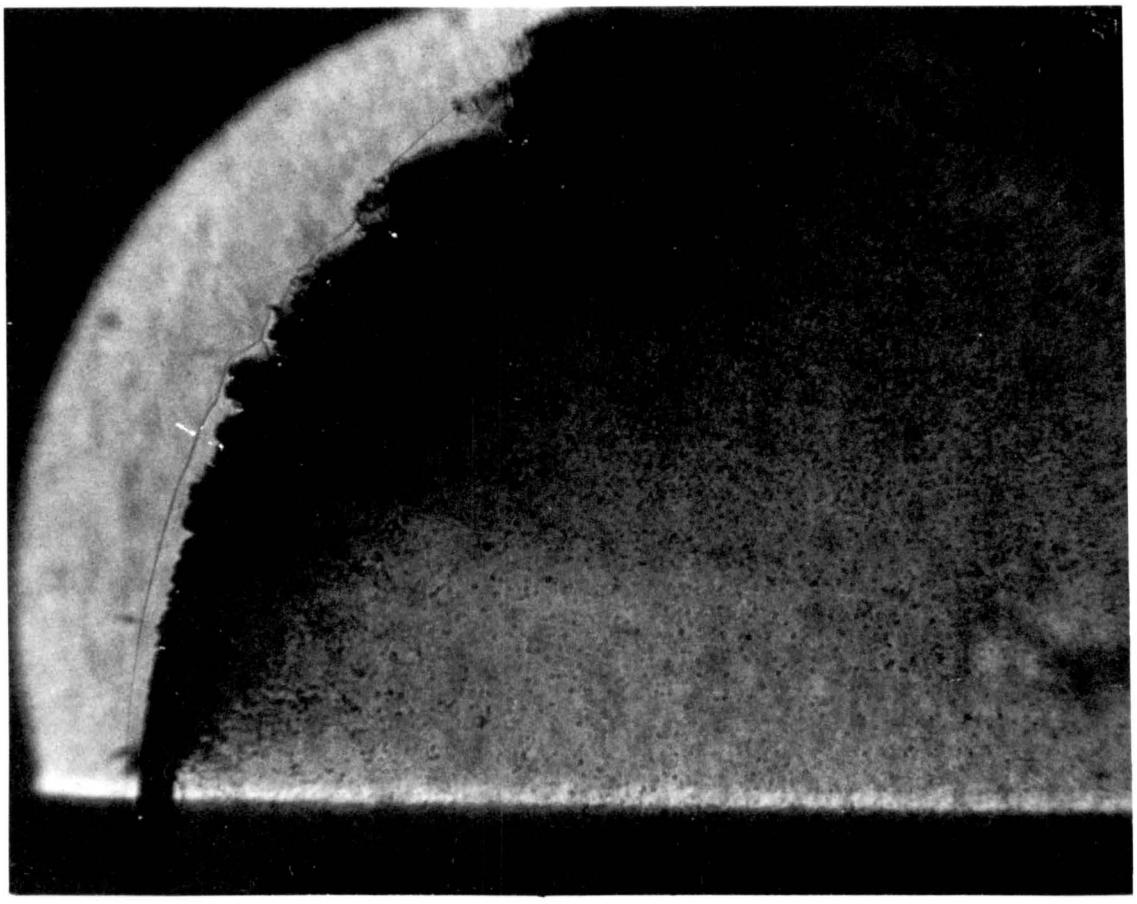

Fig. 24c: Regime 3 Injection

Water/Glycerine

μ = 18.4 Centipoise

σ = 73.0 dyne/cm.

$\bar{q}$ = 14

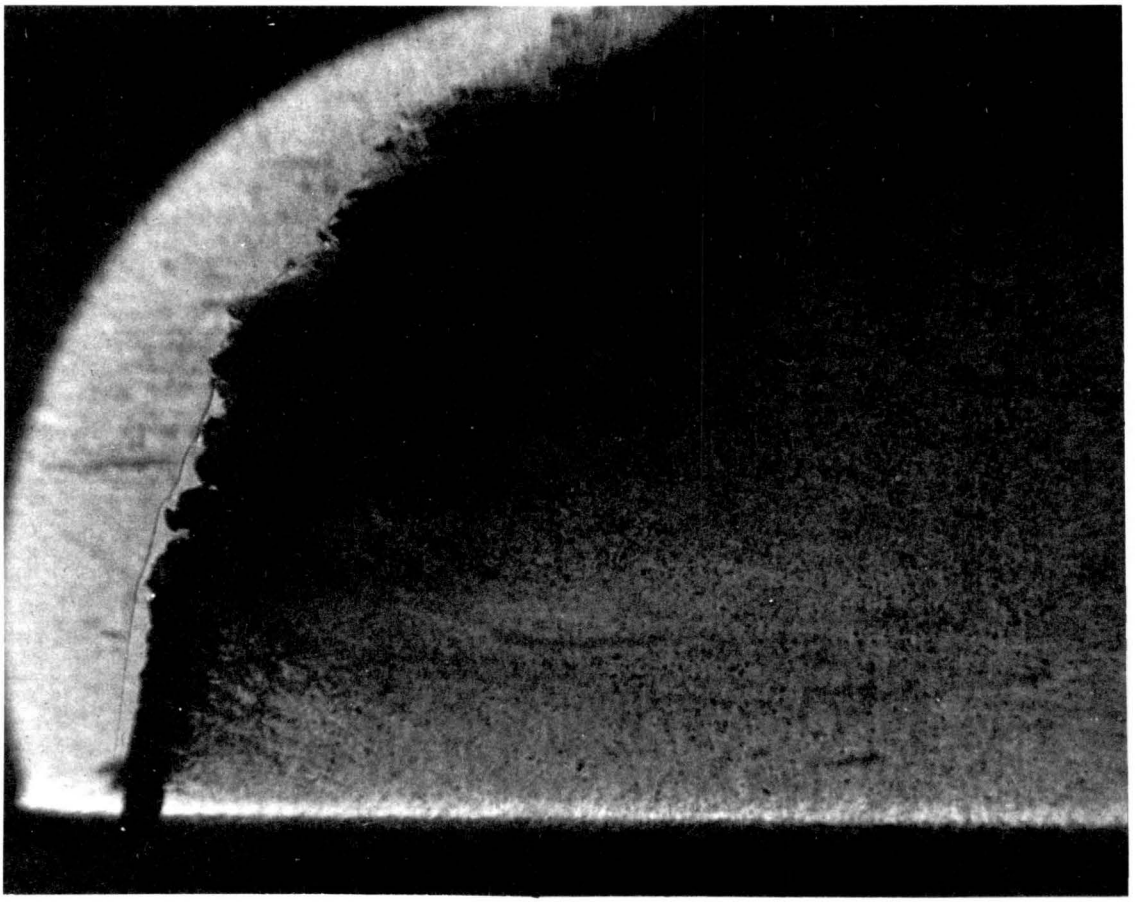

Fig. 24d. Regime 3 Injection

Water/Glycerine

μ = 27.6 Centipoise

σ = 73.0 dyne/cm.

$\bar{q}$ = 14

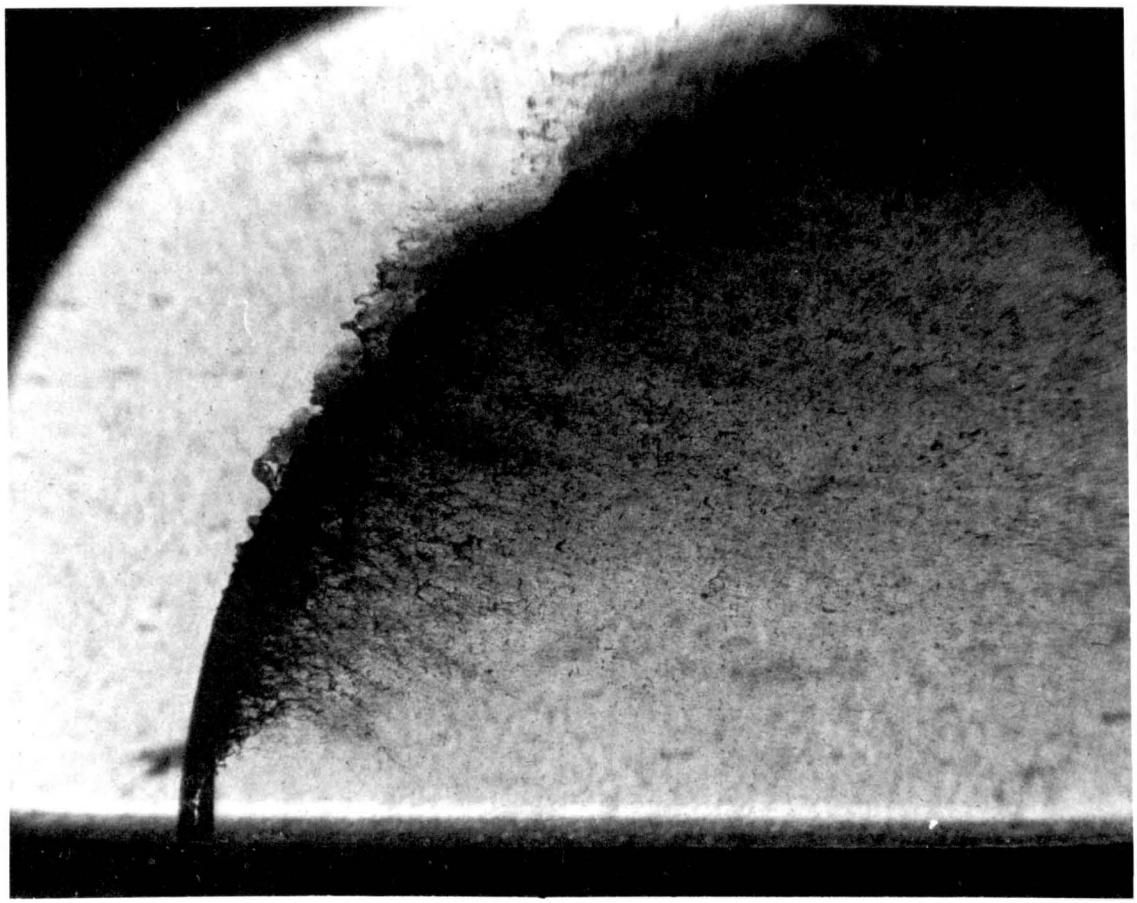

Fig. 24e: Regime 3 Injection

Water/Glycerine

μ = 40.5 Centipoise

σ = 73.0 dyne/cm.

$\bar{q}$ = 14

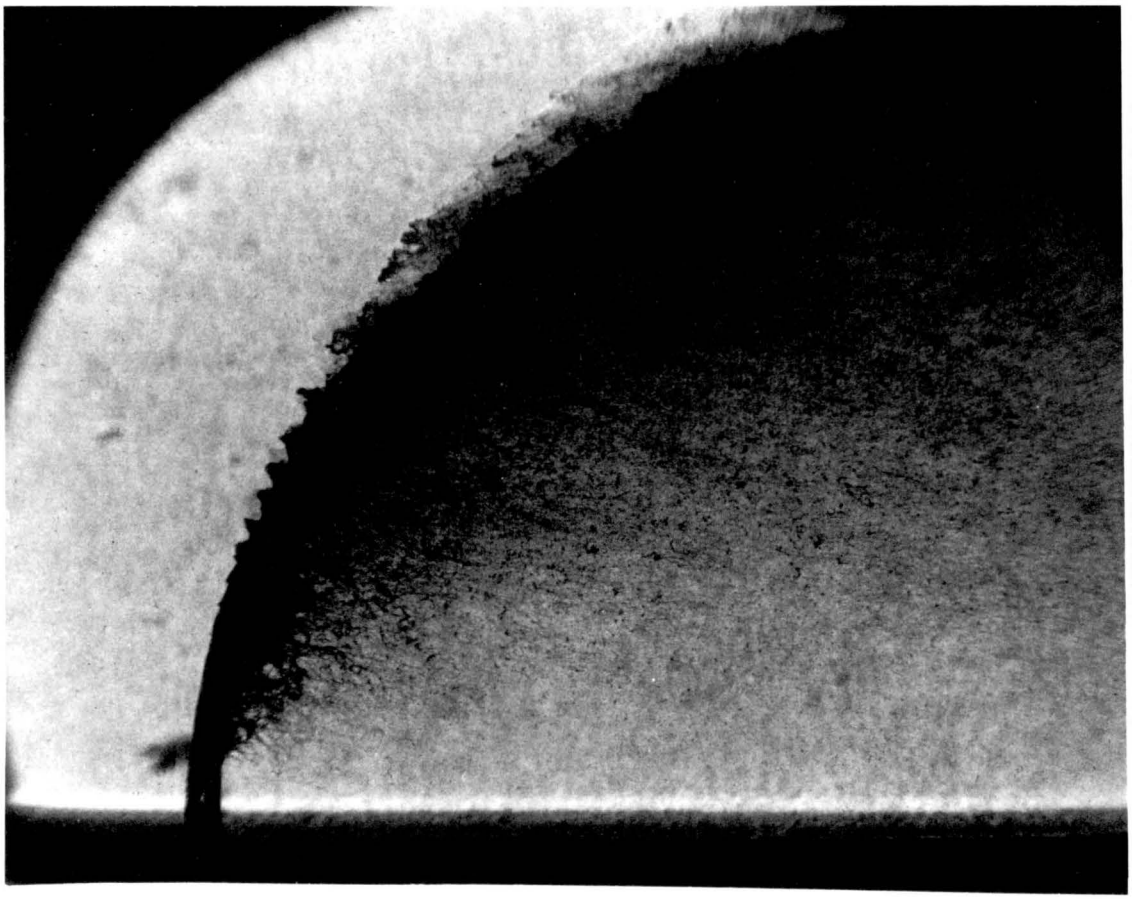

Fig. 24f: Regime 3 Injection

Water/Glycerine

μ = 59.8 Centipoise

σ = 73.0 dyne/cm.

$\bar{q}$ = 14

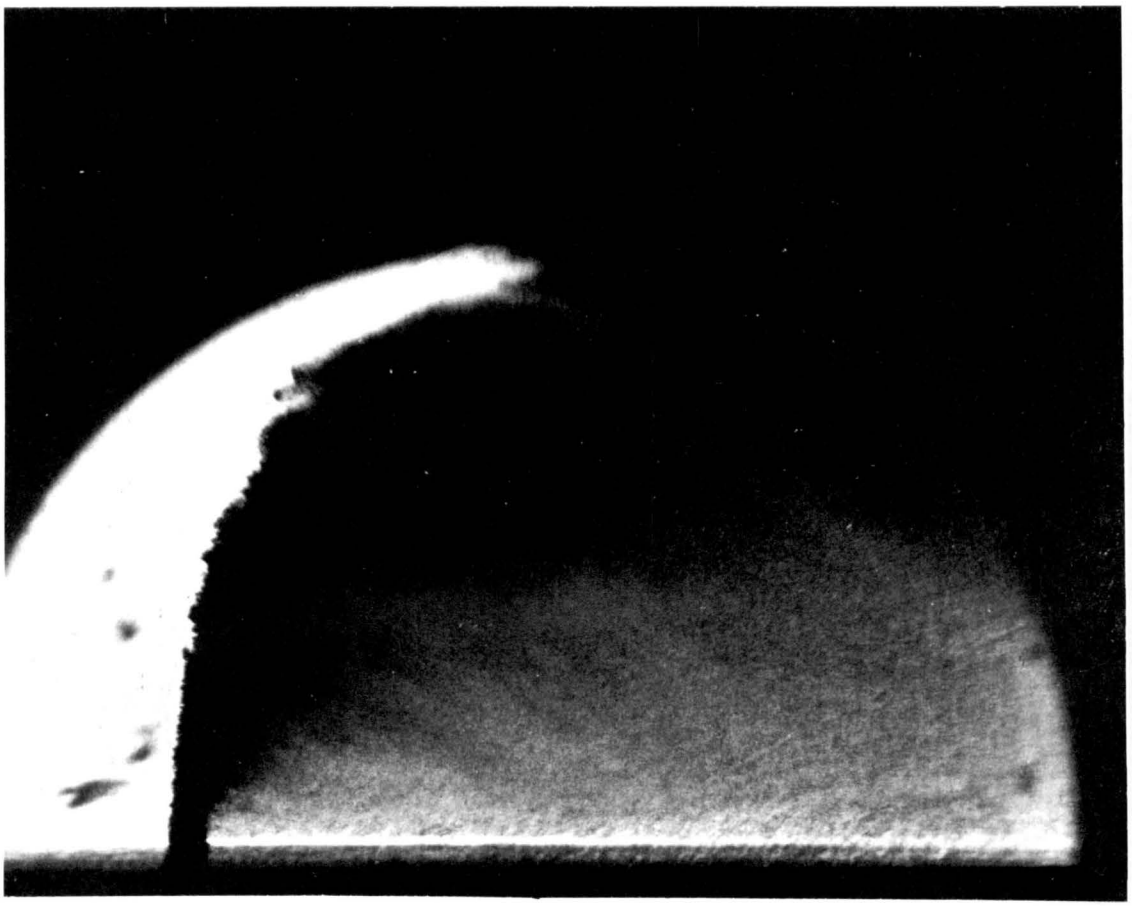

Fig. 24g: Regime 3 Injection

Water/Alcohol

μ = 1.0 Centipoise

σ = 33.5 dyne/cm.

$\bar{q}$ = 14

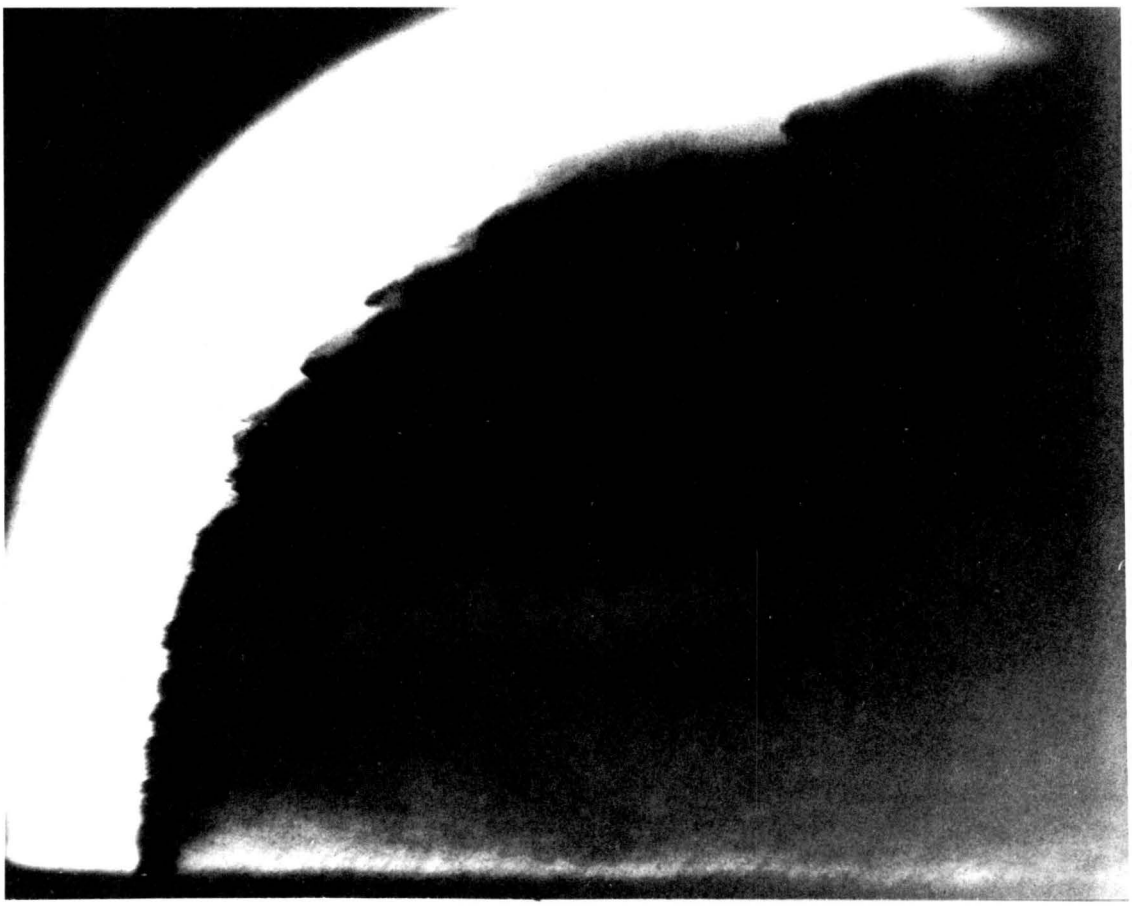

Fig. 24h: Regime 3 Injection

Fluorinert

μ = 1.5 Centipoise

σ = 15 dyne/cm.

$\bar{q}$ = 14

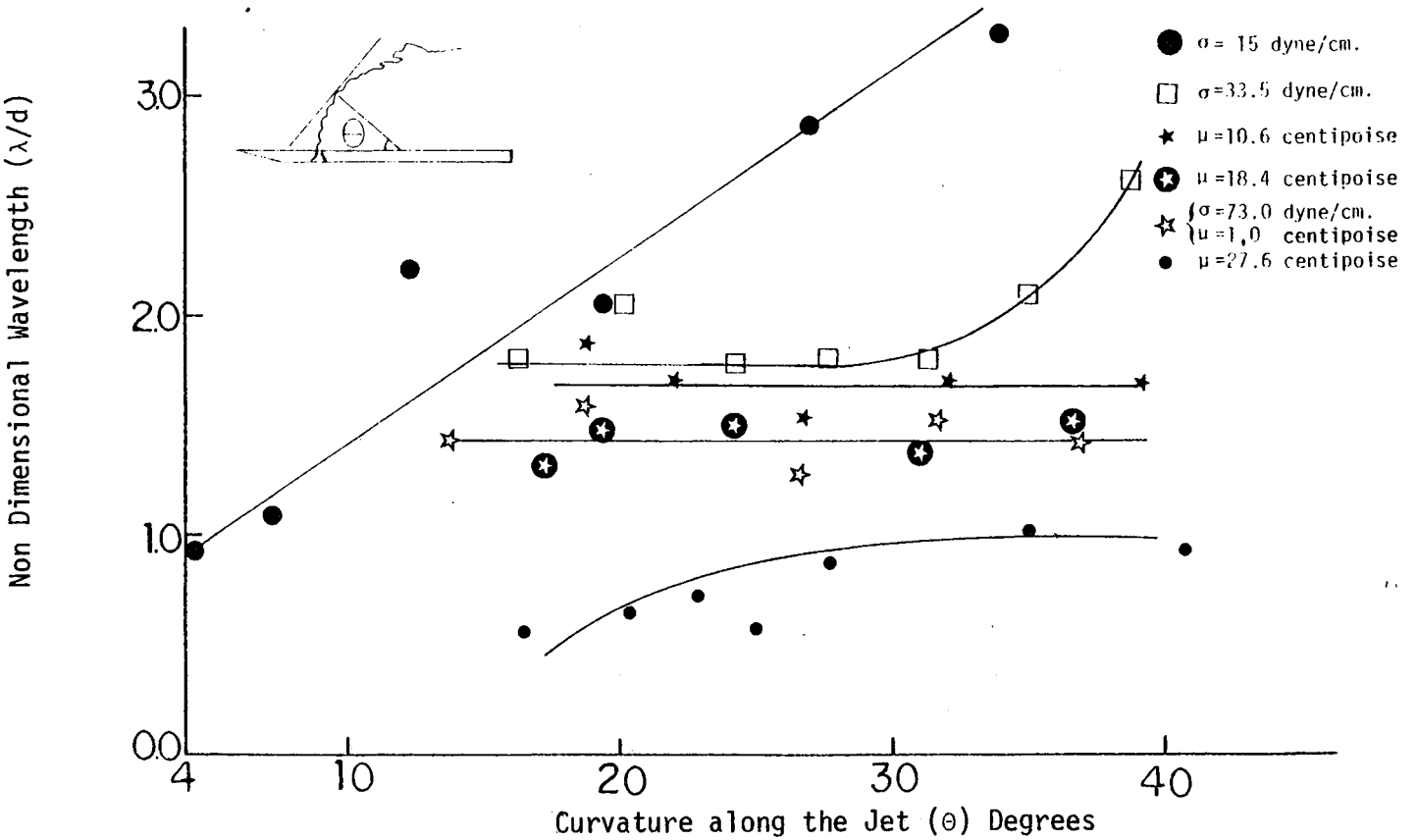

FIG. 25 EFFECTS OF VISCOSITY AND SURFACE TENSION ON WAVELENGTH ALONG THE JET COHESIVE BODY ($\bar{q}$=8)

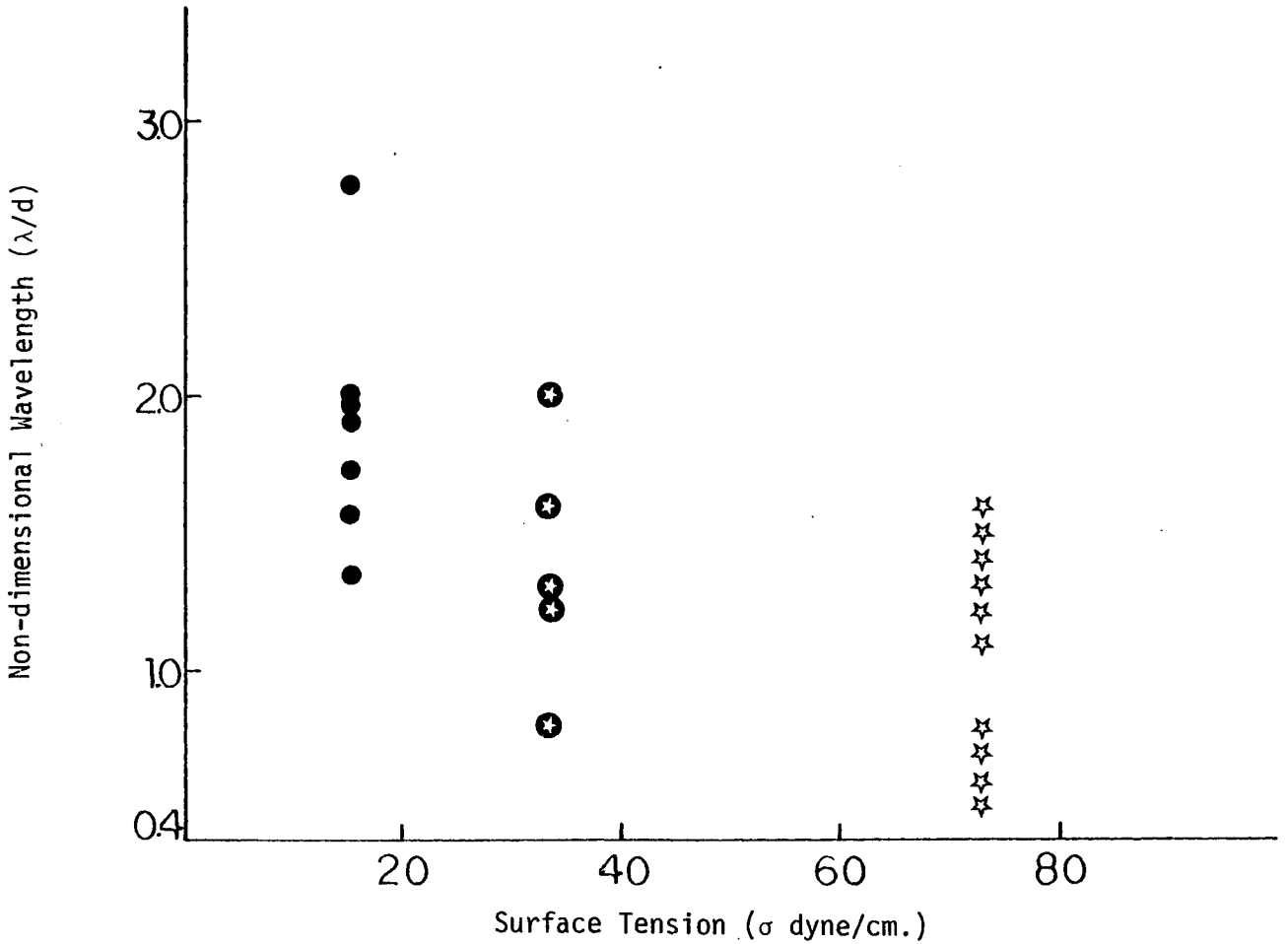

FIG. 26 WAVELENGHT ON THE COHESIVE BODY VS. INJECTANT SURFACE TENSION, DIFFERENT $\bar{q}$'S

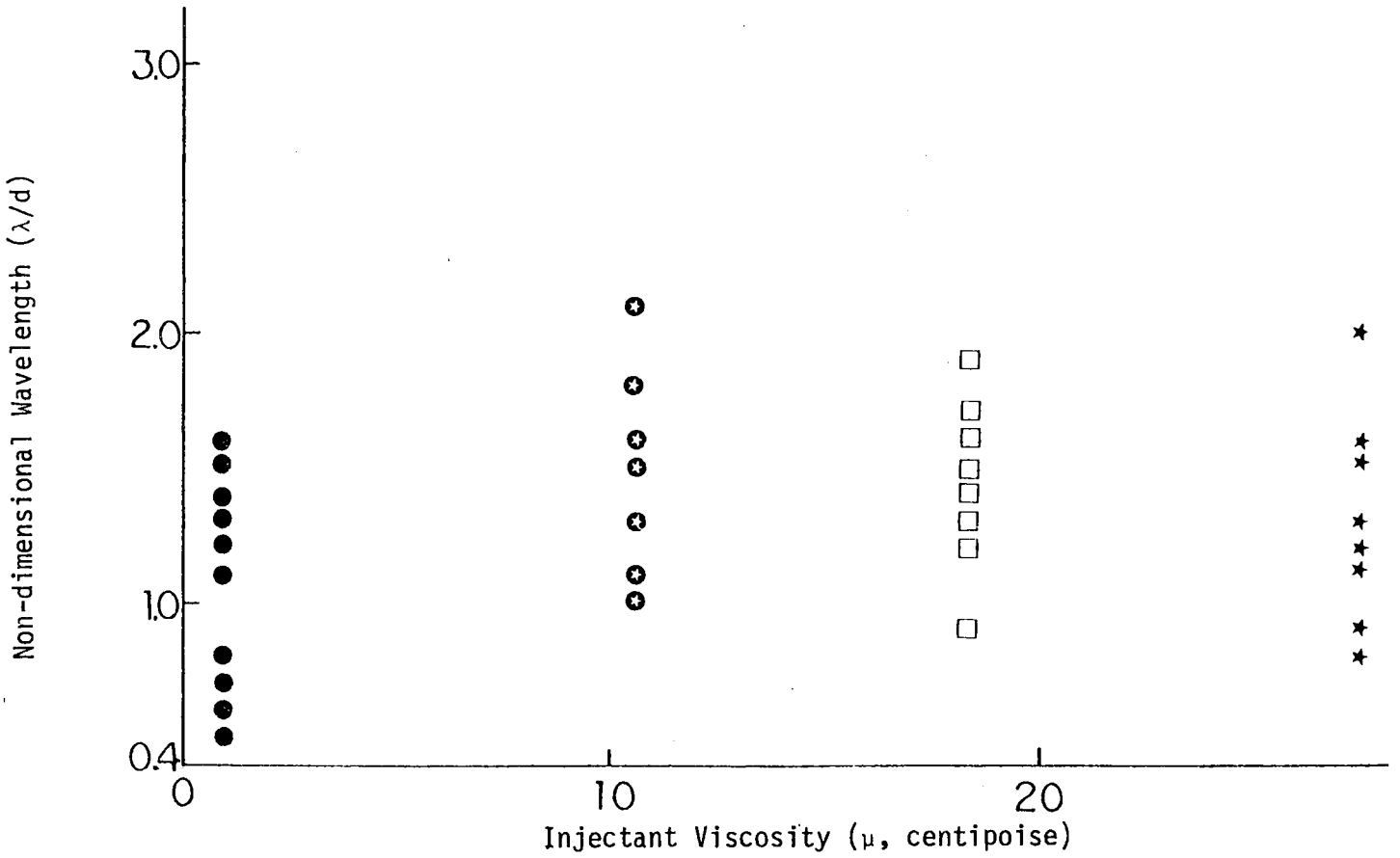

FIG. 27 WAVELENGTH ON THE COHESIVE JET BODY VS. INJECTANT VISCOSITY, DIFFERENT, $\bar{q}$'s

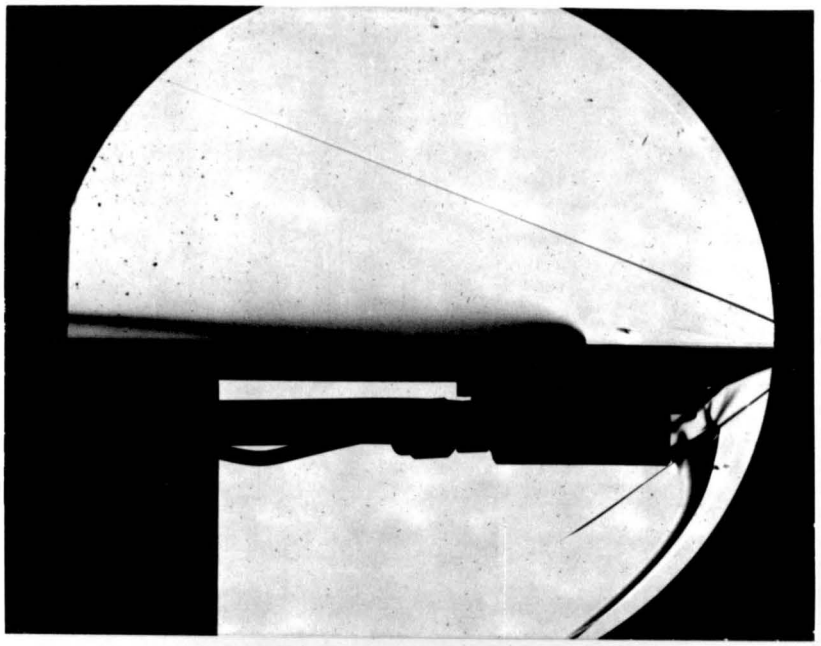

$\bar{q} = 1$

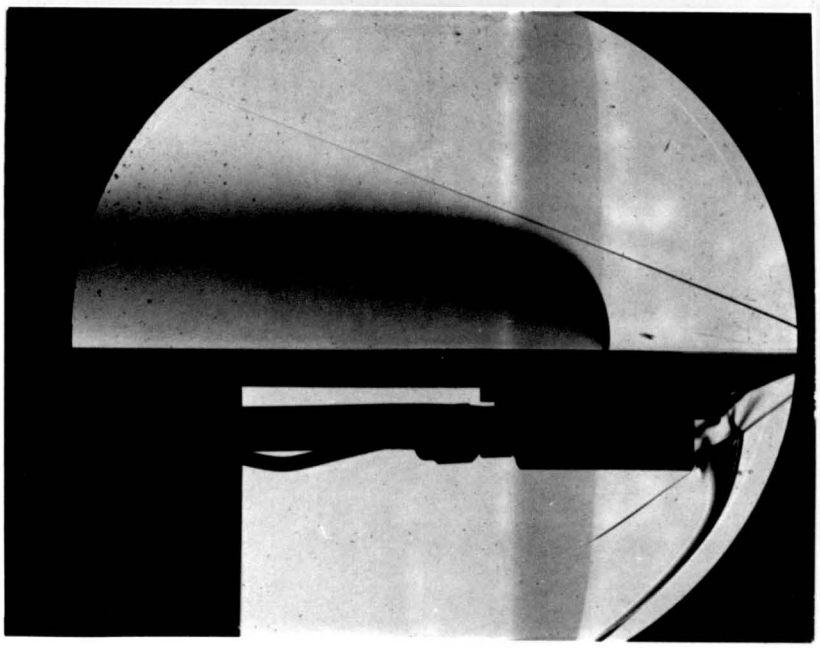

$\bar{q} = 20$

Fig. 28: Examples of Streak Type Photographs.

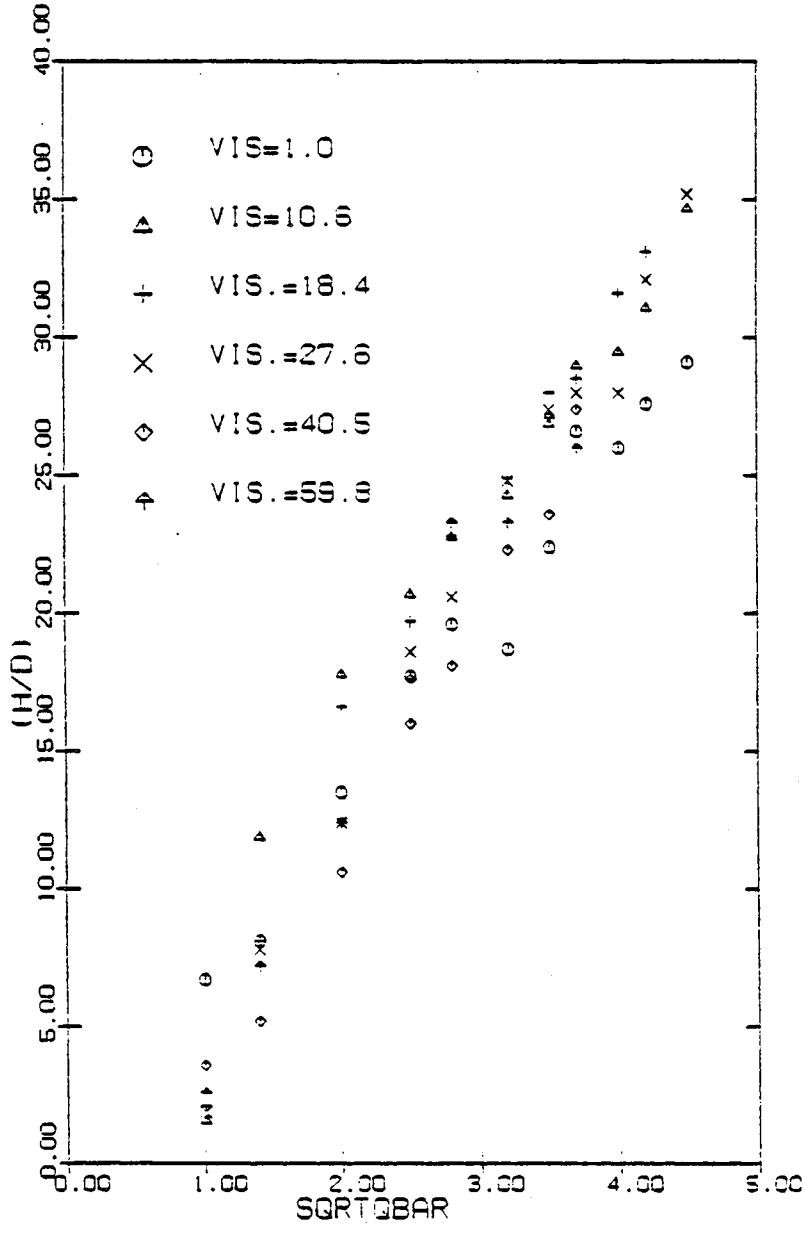

FIG. 29 PENETRATION VS. DYNAMIC PRESSURE RATIO (X/D=26)

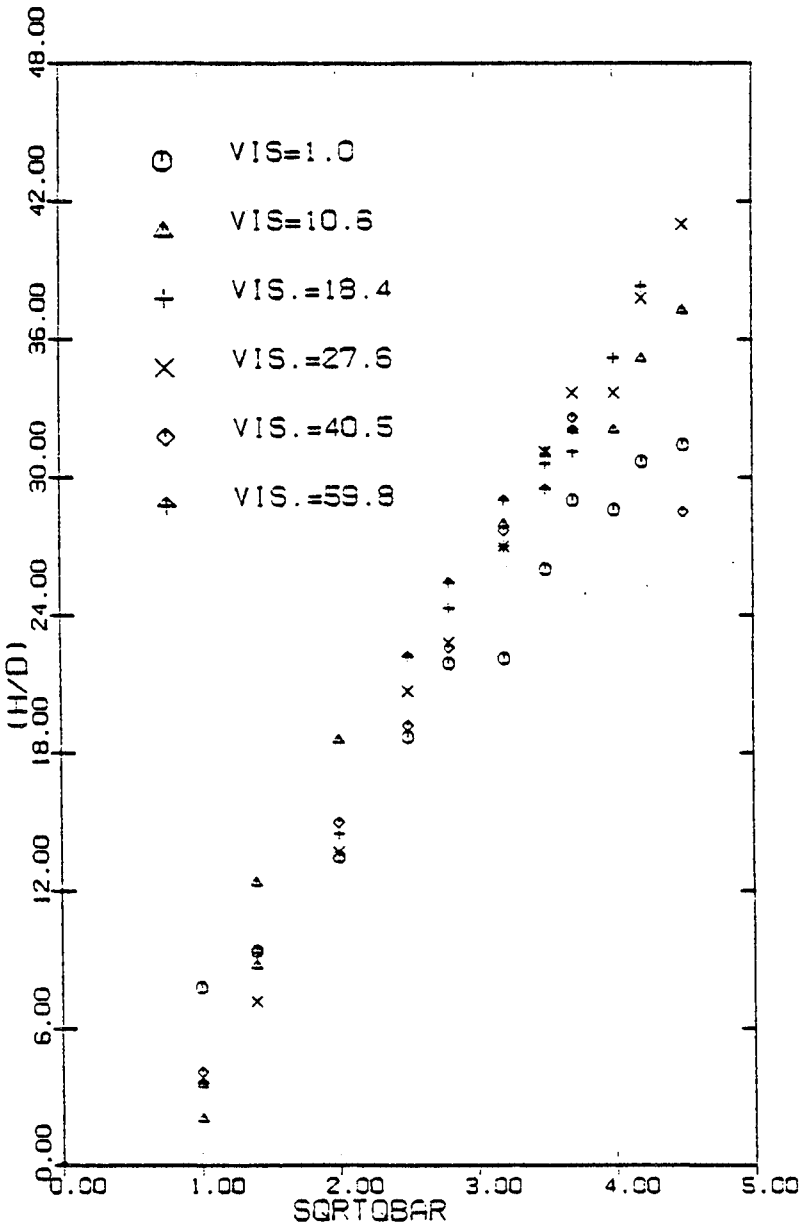

FIG 30 PENETRATION VS. DYNAMIC PRESSURE RATIO (X/D=52)

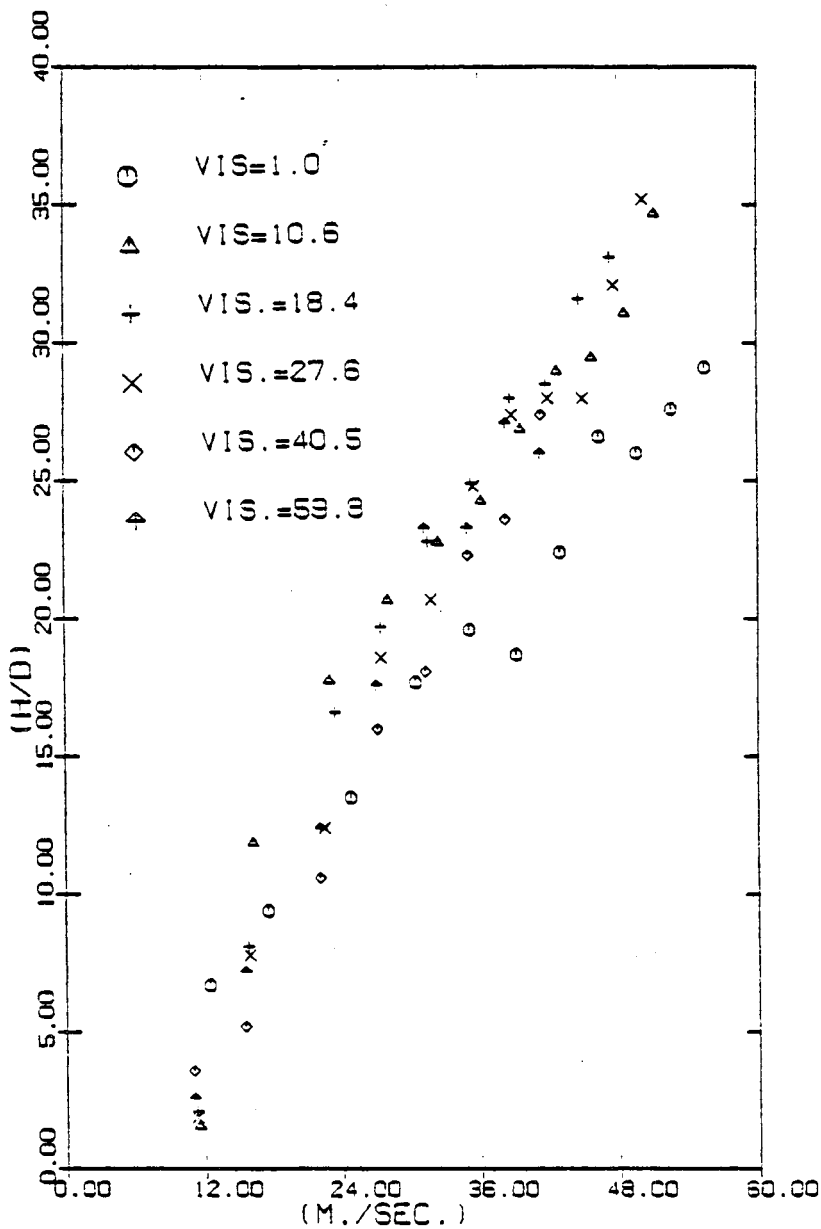

FIG. 31 PENETRATION VS. JET VELOCITY (X/D=26)

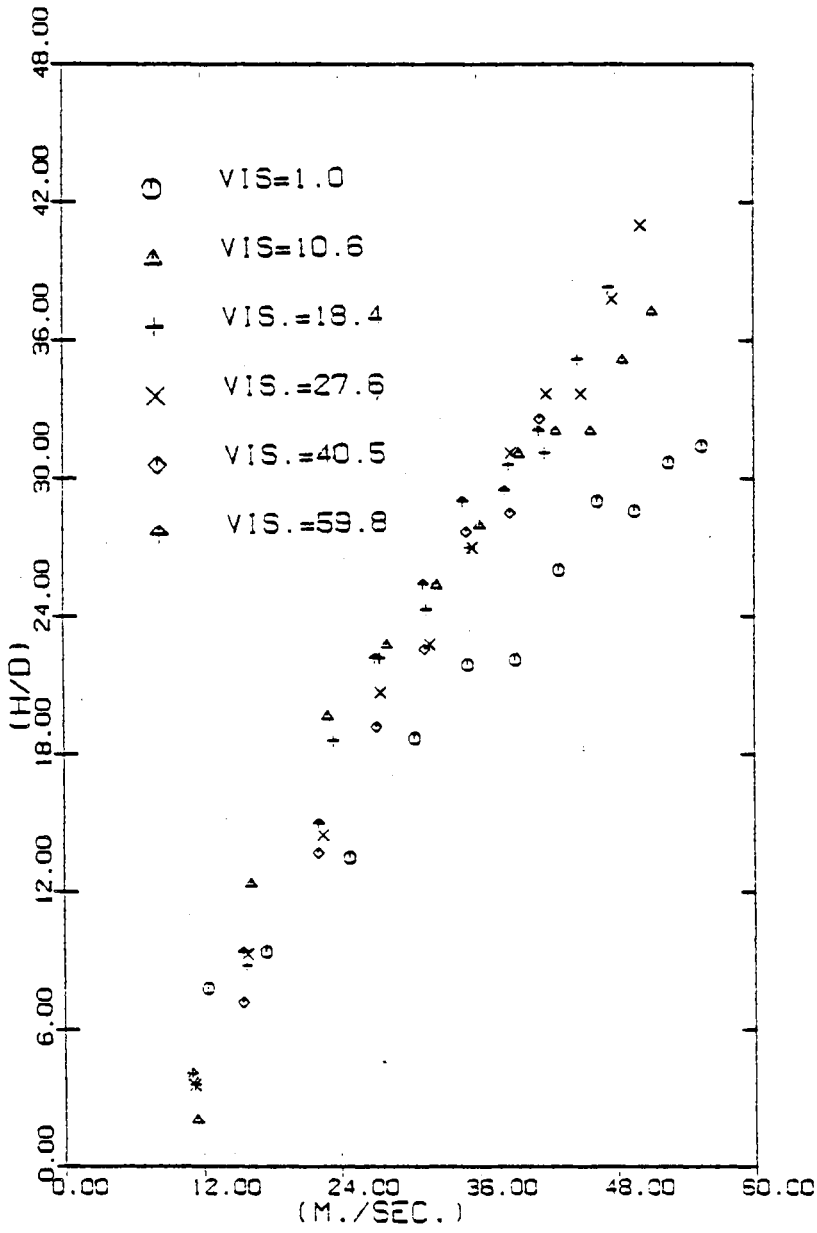

FIG. 32 PENETRATION VS. JET VELOCITY (X/D=52)

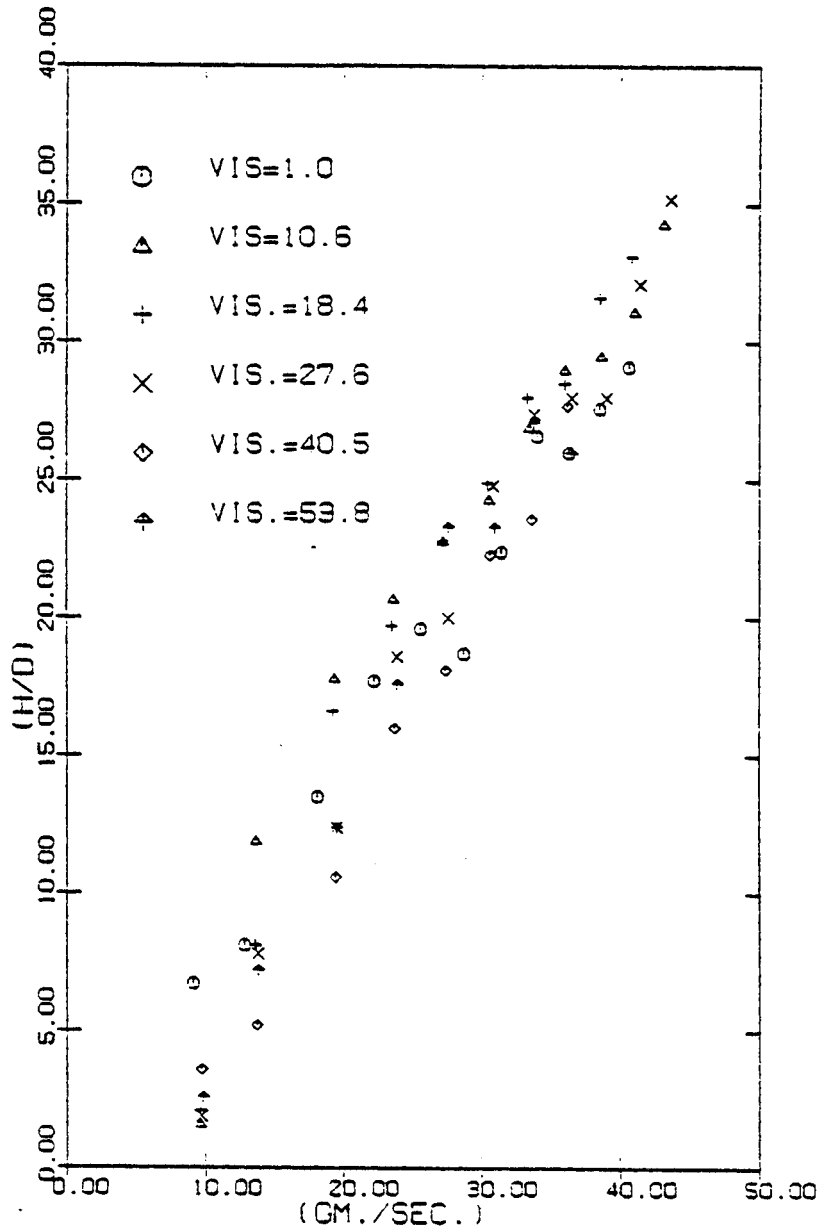

FIG. 33 PENETRATION VS. MASS FLOW RATE (X/D=26)

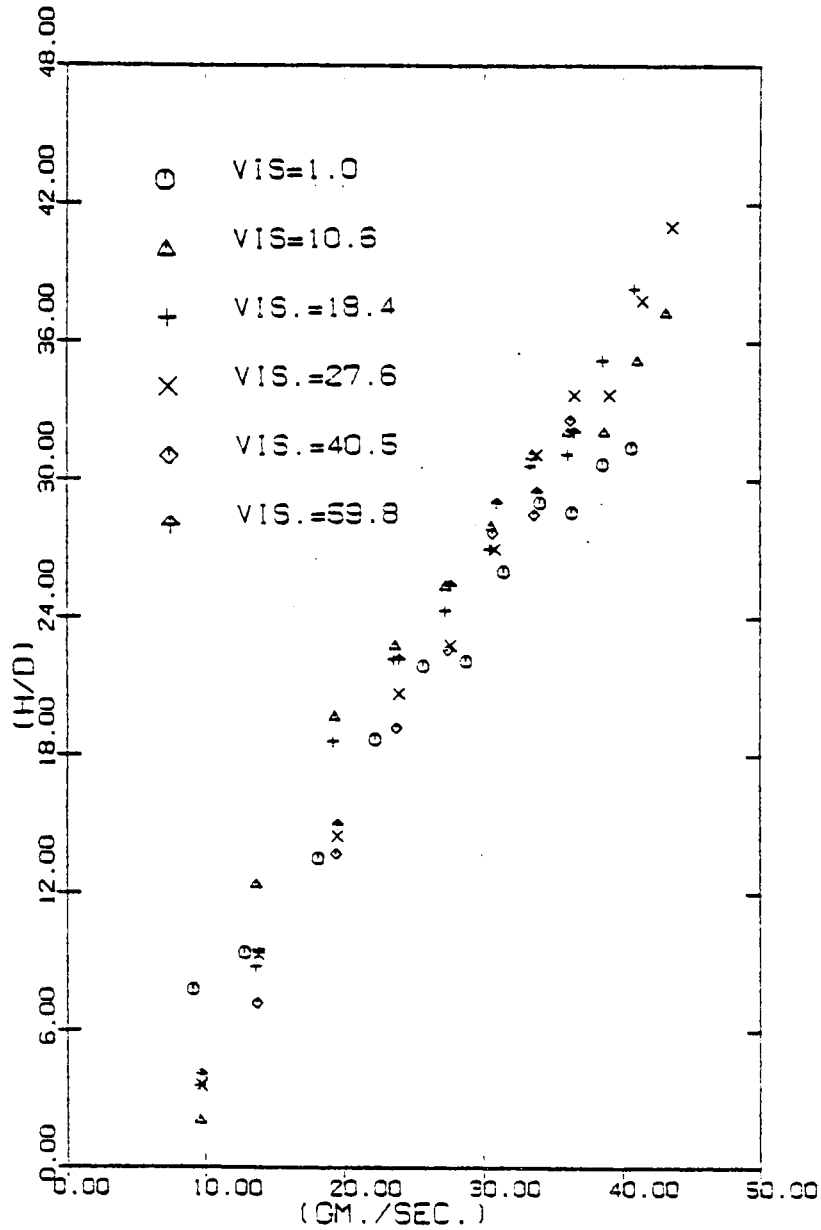

FIG. 34 PENETRATION VS. MASS FLOW RATE (X/D=52)

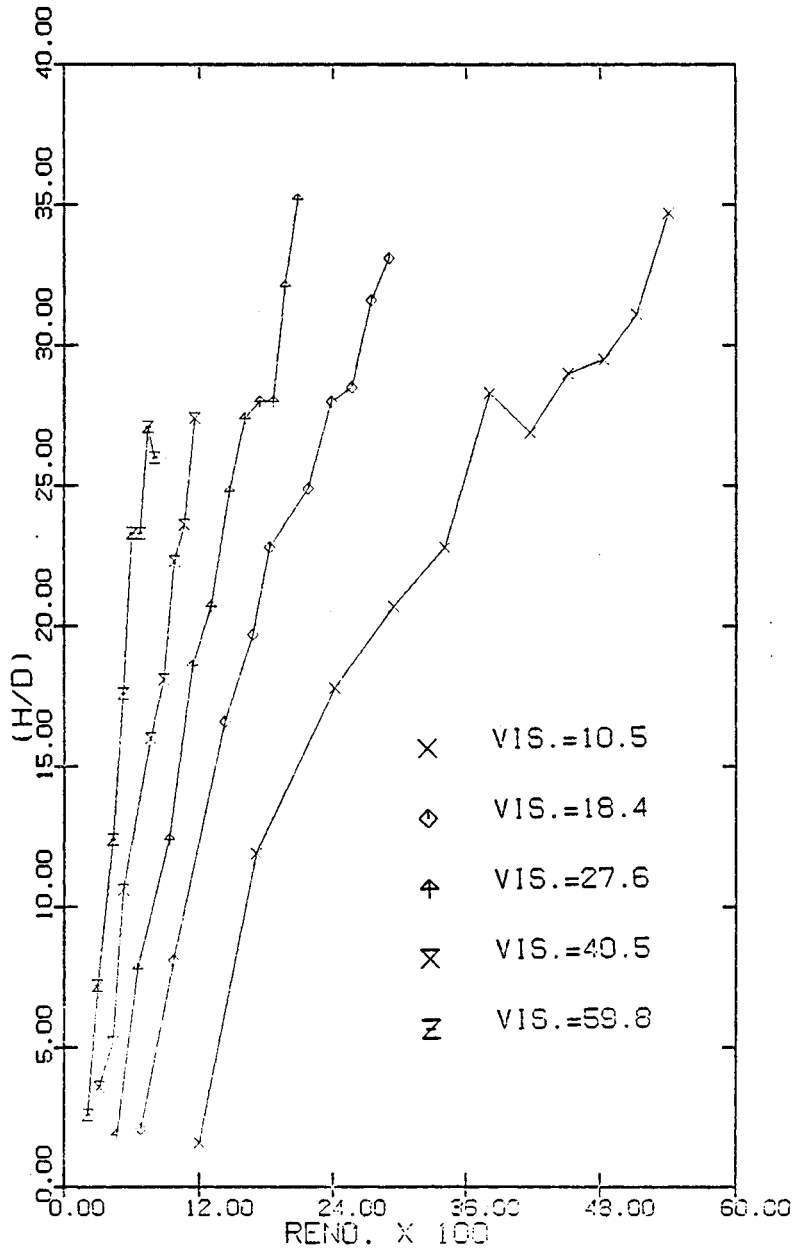

FIG. 35 PENETRATION VS. REYNOLDS NUMBER (X/D=26)

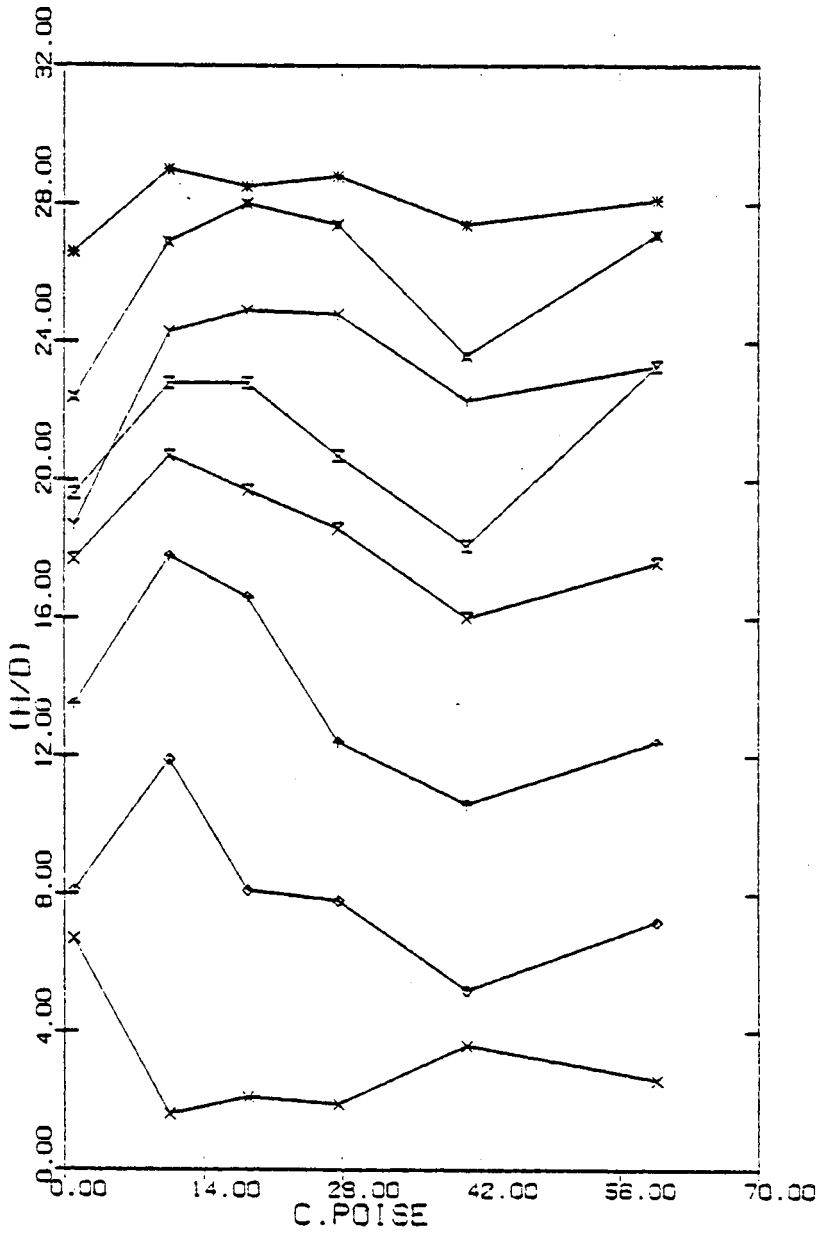

FIG. 36 PENETRATION VS. VISCOSITY (X/D=26)

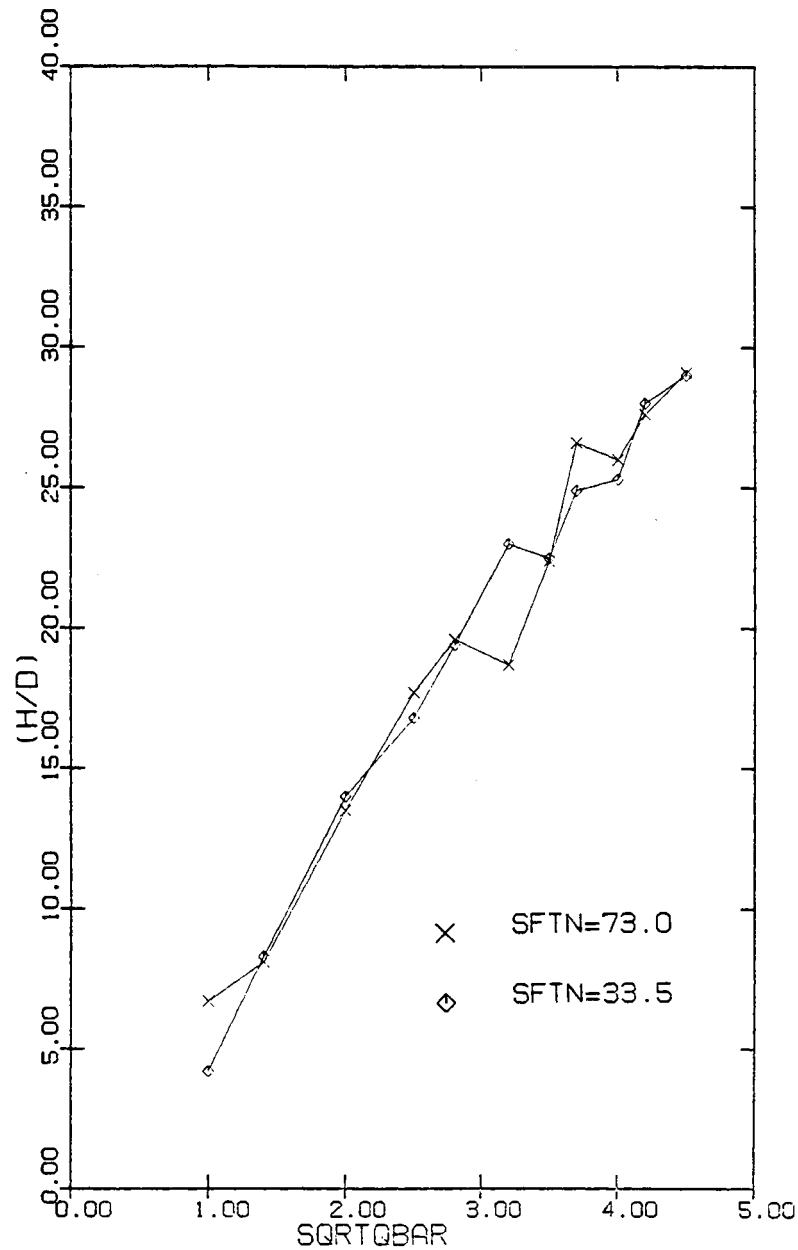

FIG. 37 PENETRATION VS. DYNAMIC PRESSURE RATIO (X/D=26)

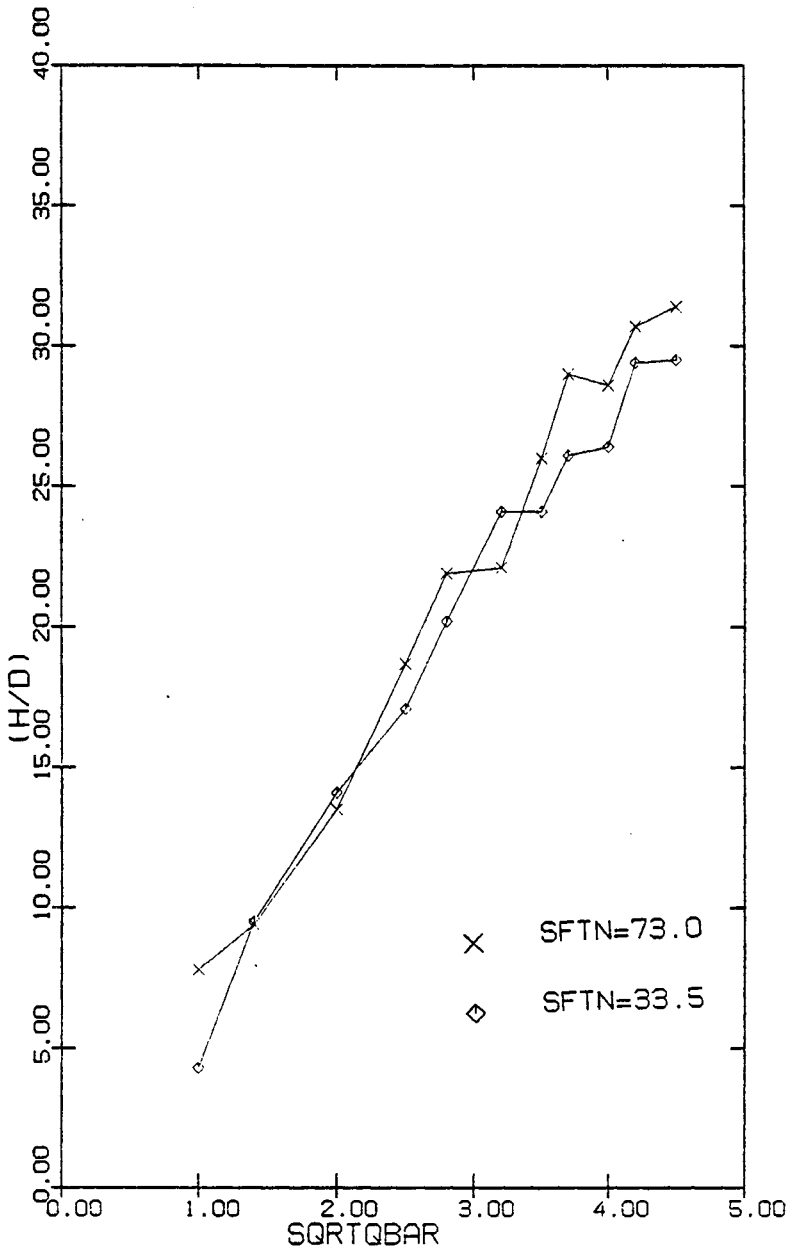

FIG. 38 PENETRATION VS. DYNAMIC PRESSURE RATIO (X/D=52)

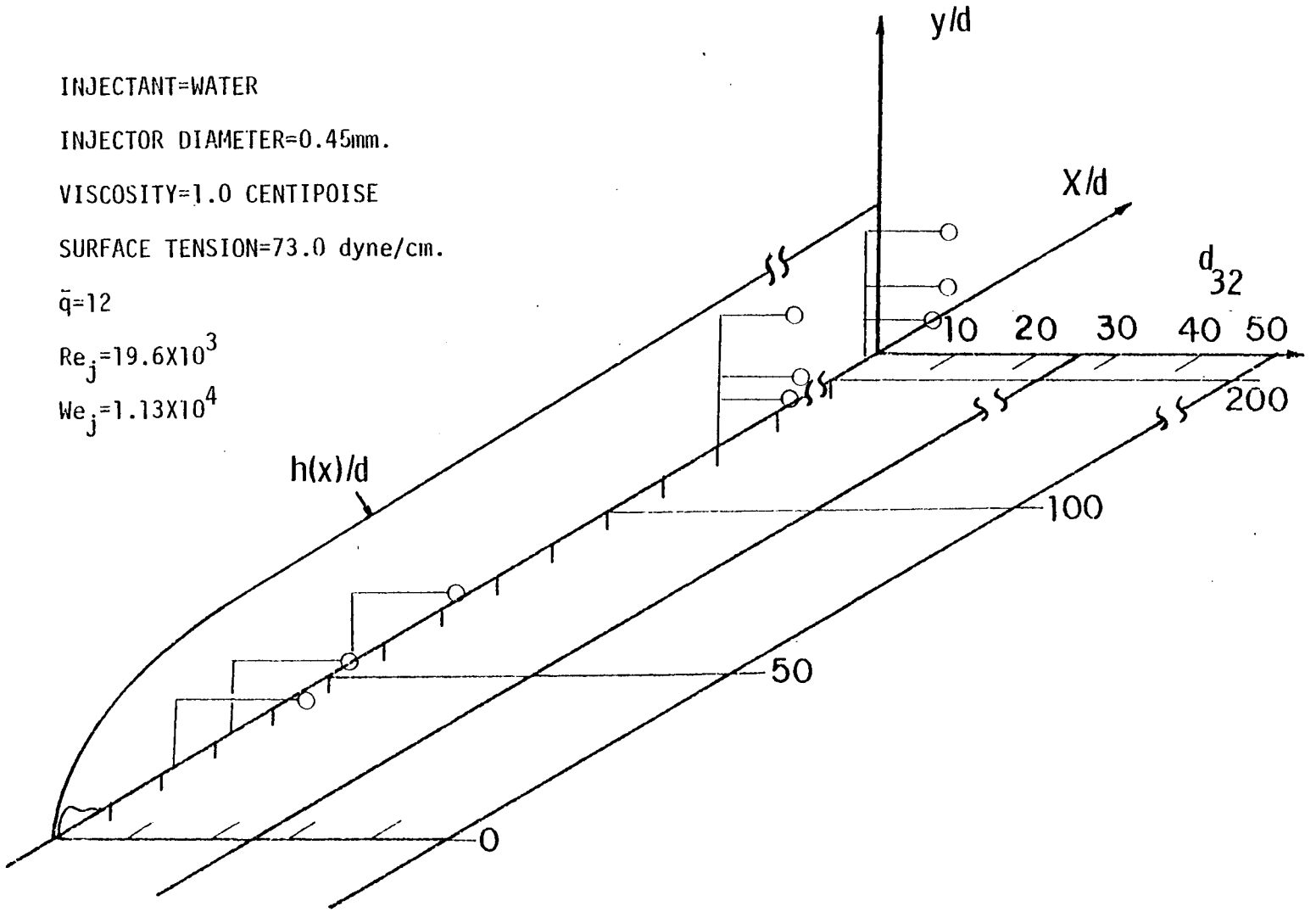

Fig. 39a MEAN DROPLET DIAMETER VARIATION IN THE PLUME FOR WATER INJECTION

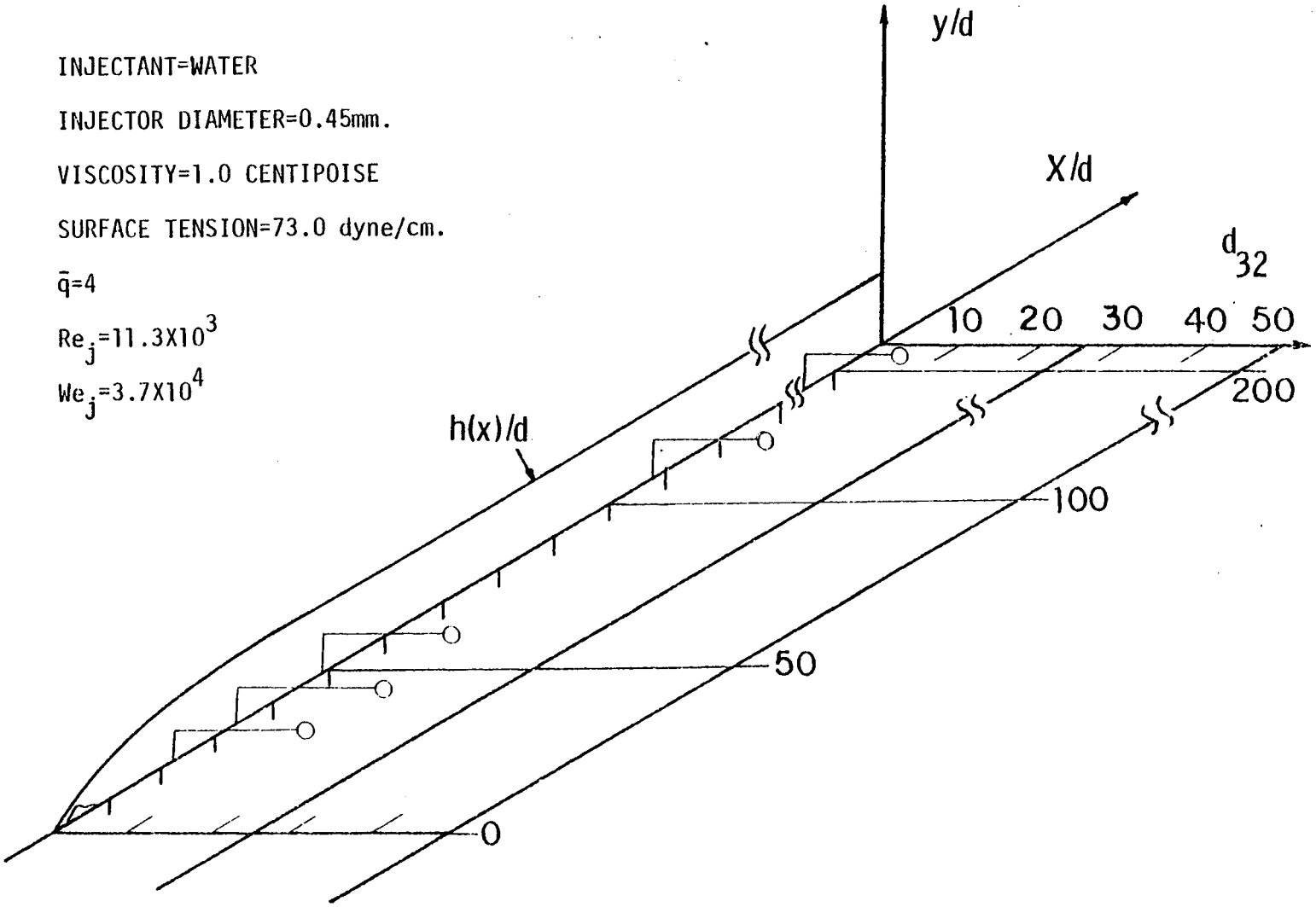

Fig. 39b MEAN DROPLET DIAMETER VARIATION IN THE PLUME FOR WATER INJECTION,CONTINUED

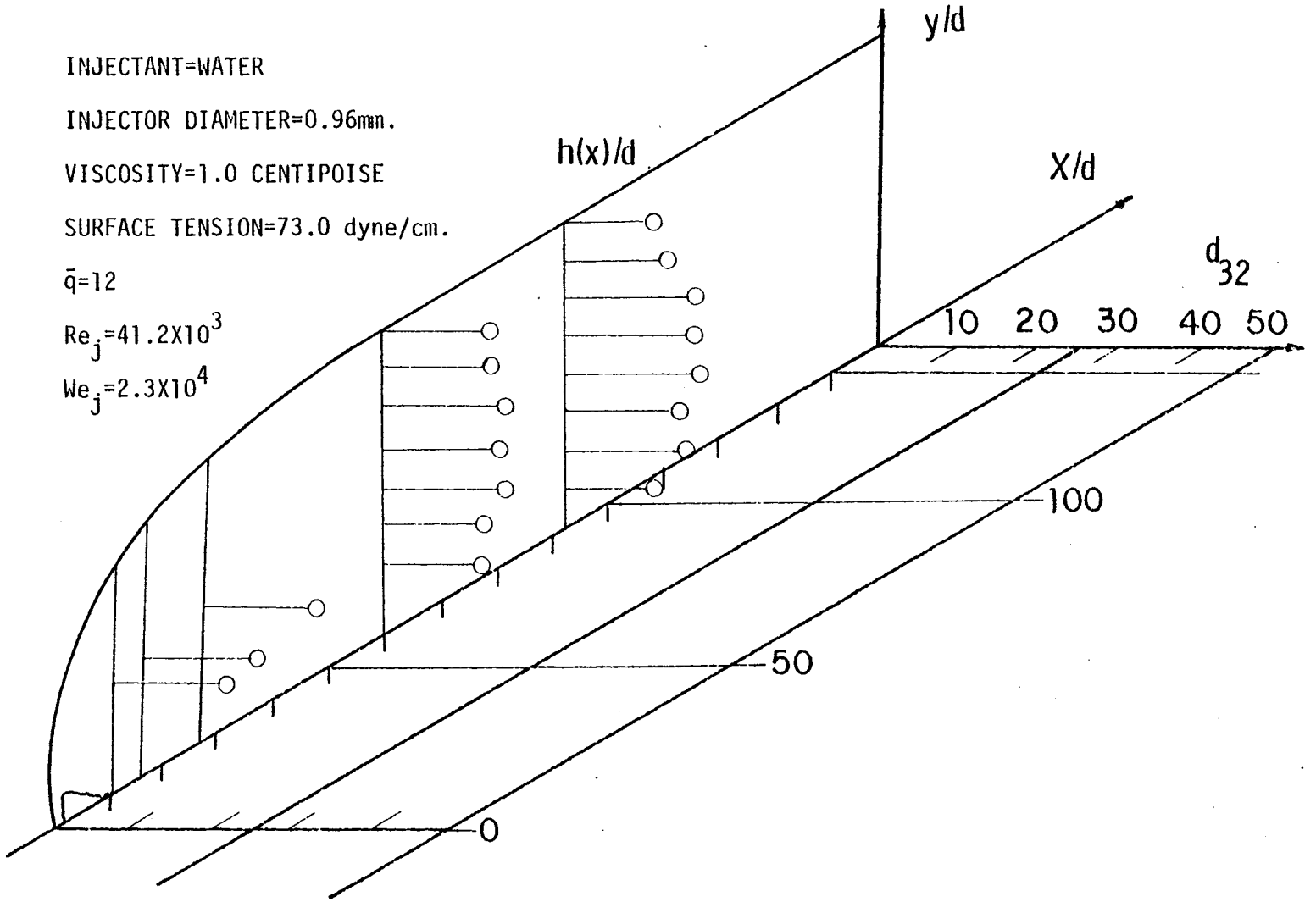

Fig. 39c MEAN DROPLET DIAMETER VARIATION IN THE PLUME FOR WATER INJECTION, CONTINUED

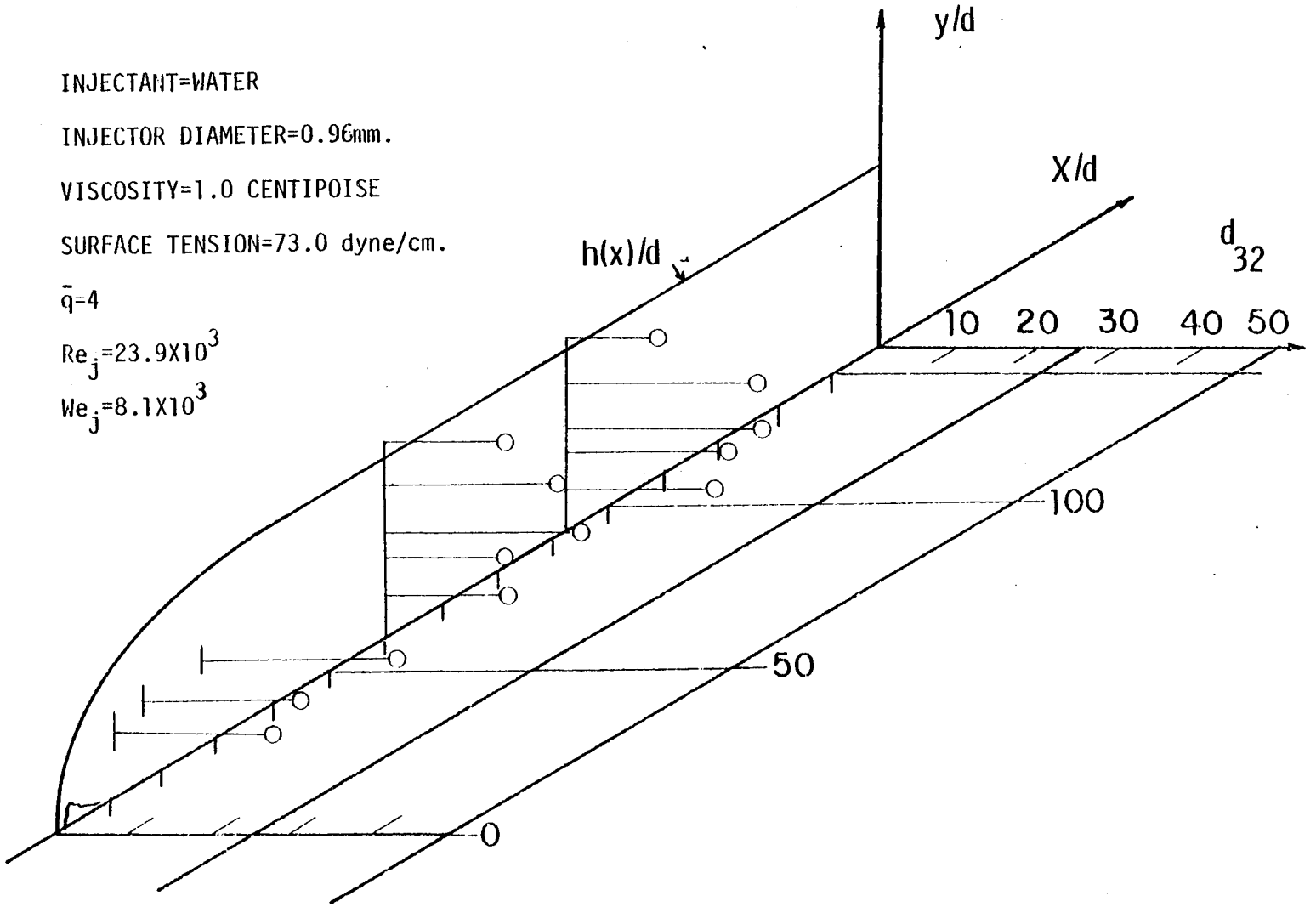

Fig. 39d MEAN DROPLET DIAMETER VARIATION IN THE PLUME FOR WATER INJECTION, CONTINUED

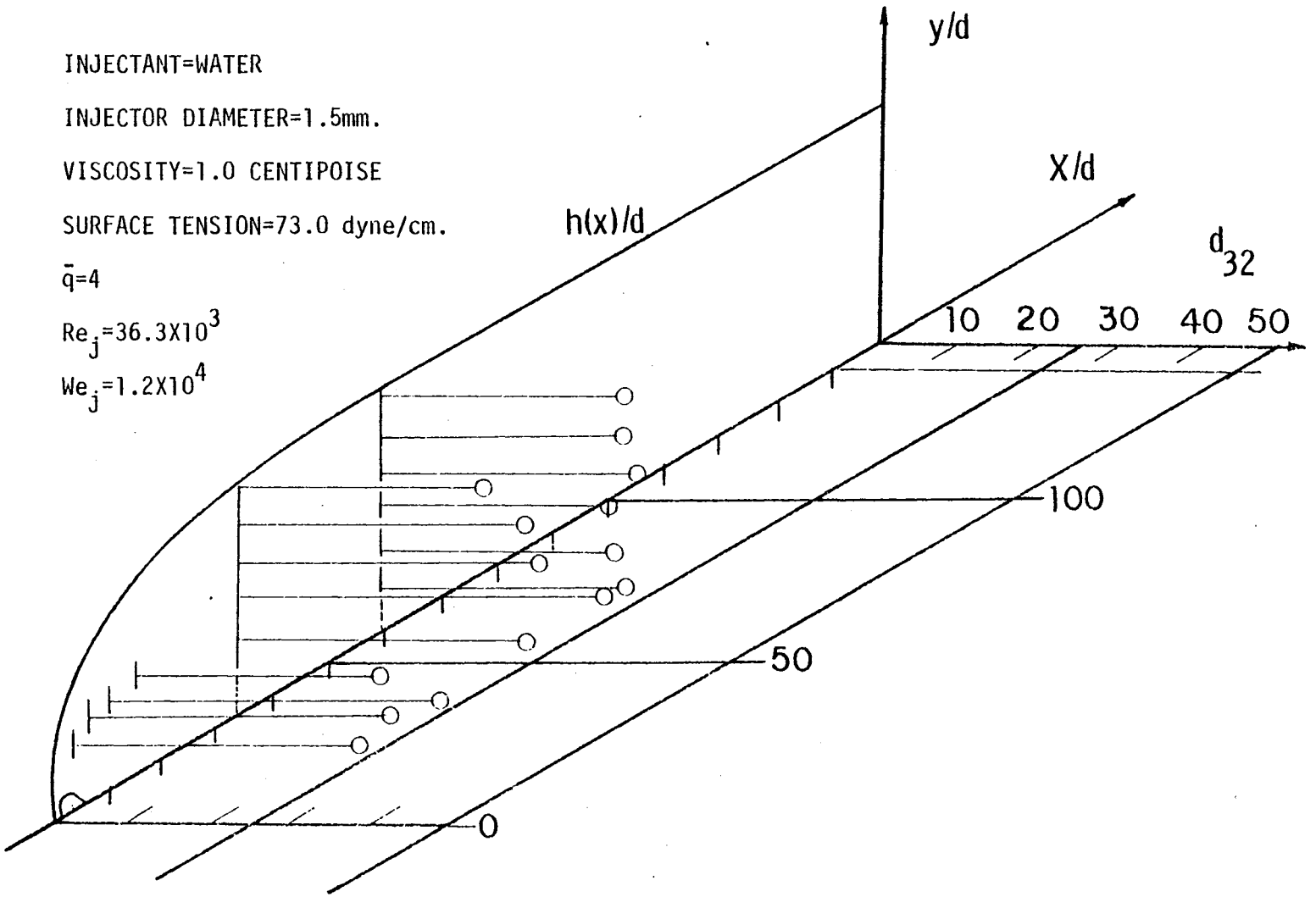

Fig. 39e MEAN DROPLET DIAMETER VARIATION IN THE PLUME FOR WATER INJECTION, CONTINUED

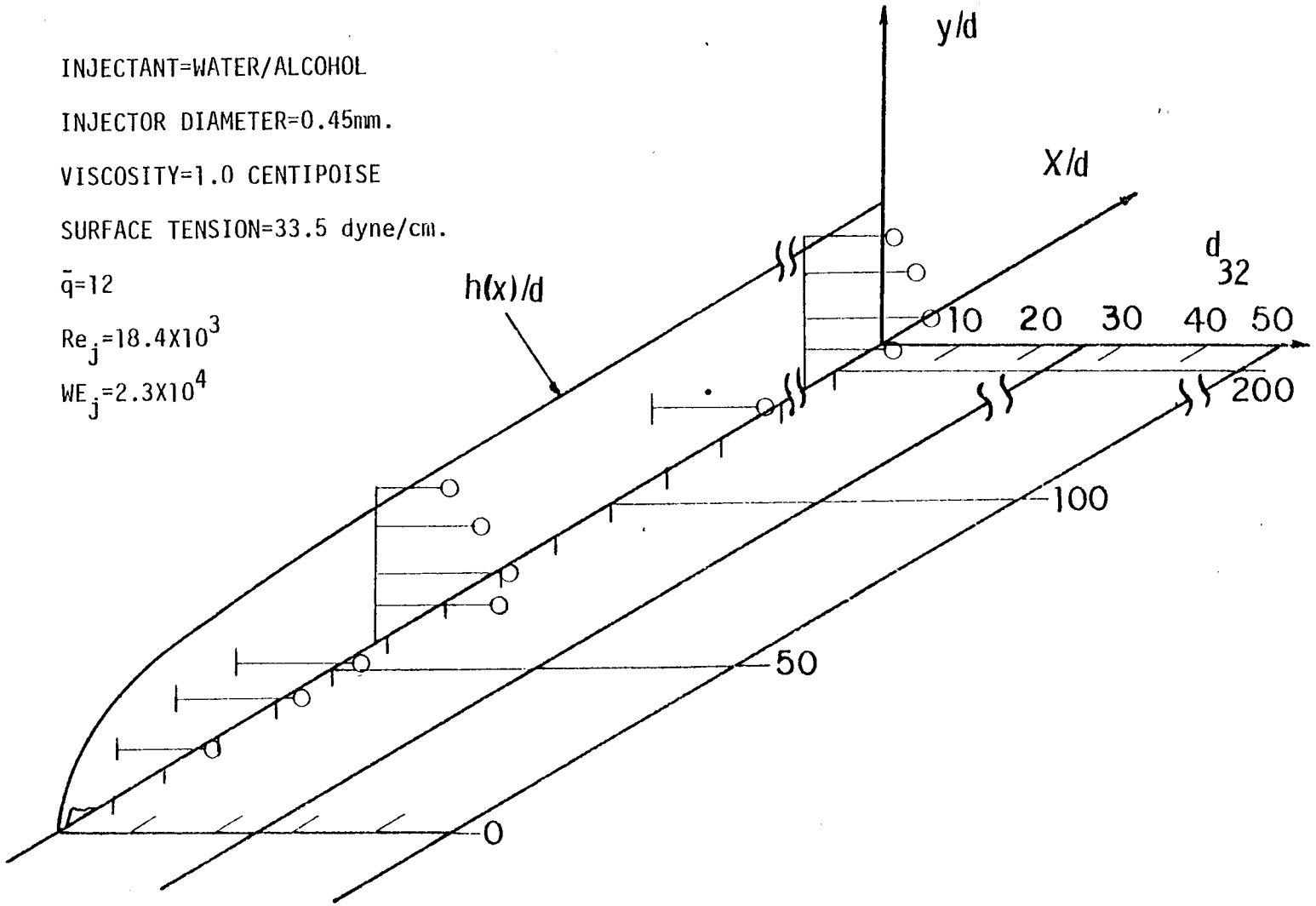

Fig. 40a MEAN DROPLET DIAMETER VARIATION IN THE PLUME FOR WATER/ALCOHOL INJECTION

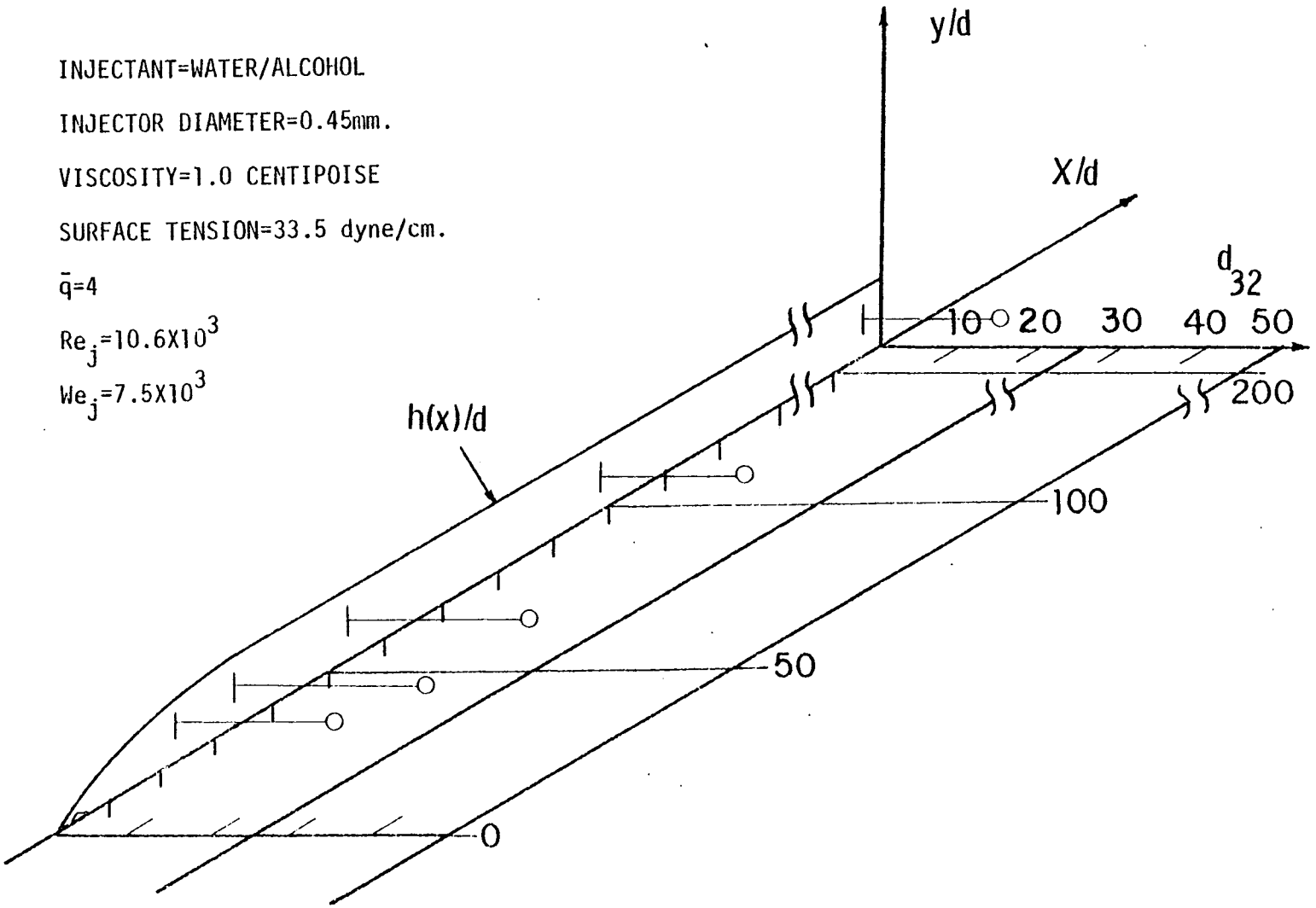

Fig. 40b MEAN DROPLET DIAMETER VARIATION IN THE PLUME FOR WATER/ALCOHOL INJECTION, CONTINUED

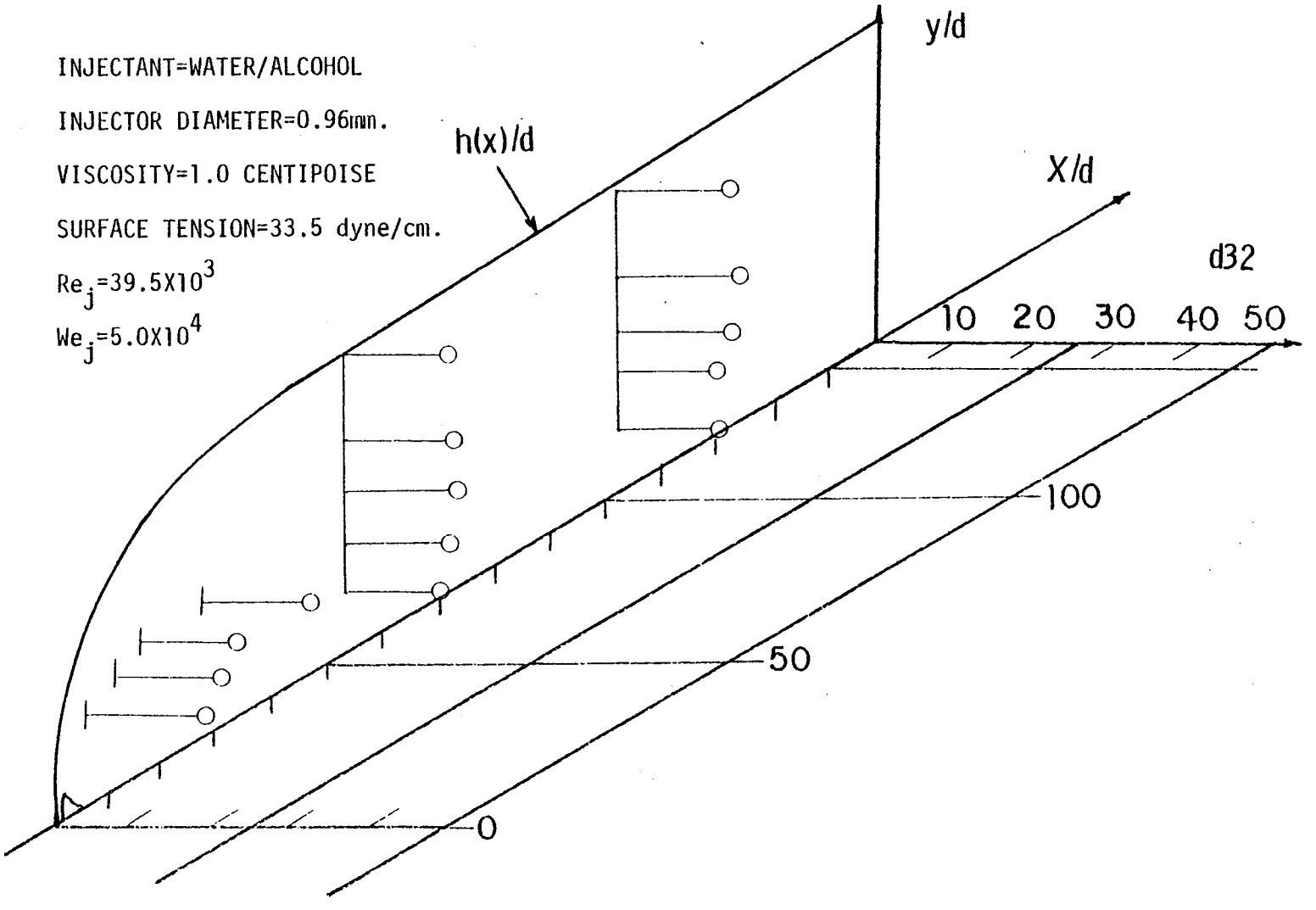

Fig. 40c MEAN DROPLET DIAMETER VARIATION IN THE PLUME FOR WATER/ALCOHOL INJECTION,CONTINUED

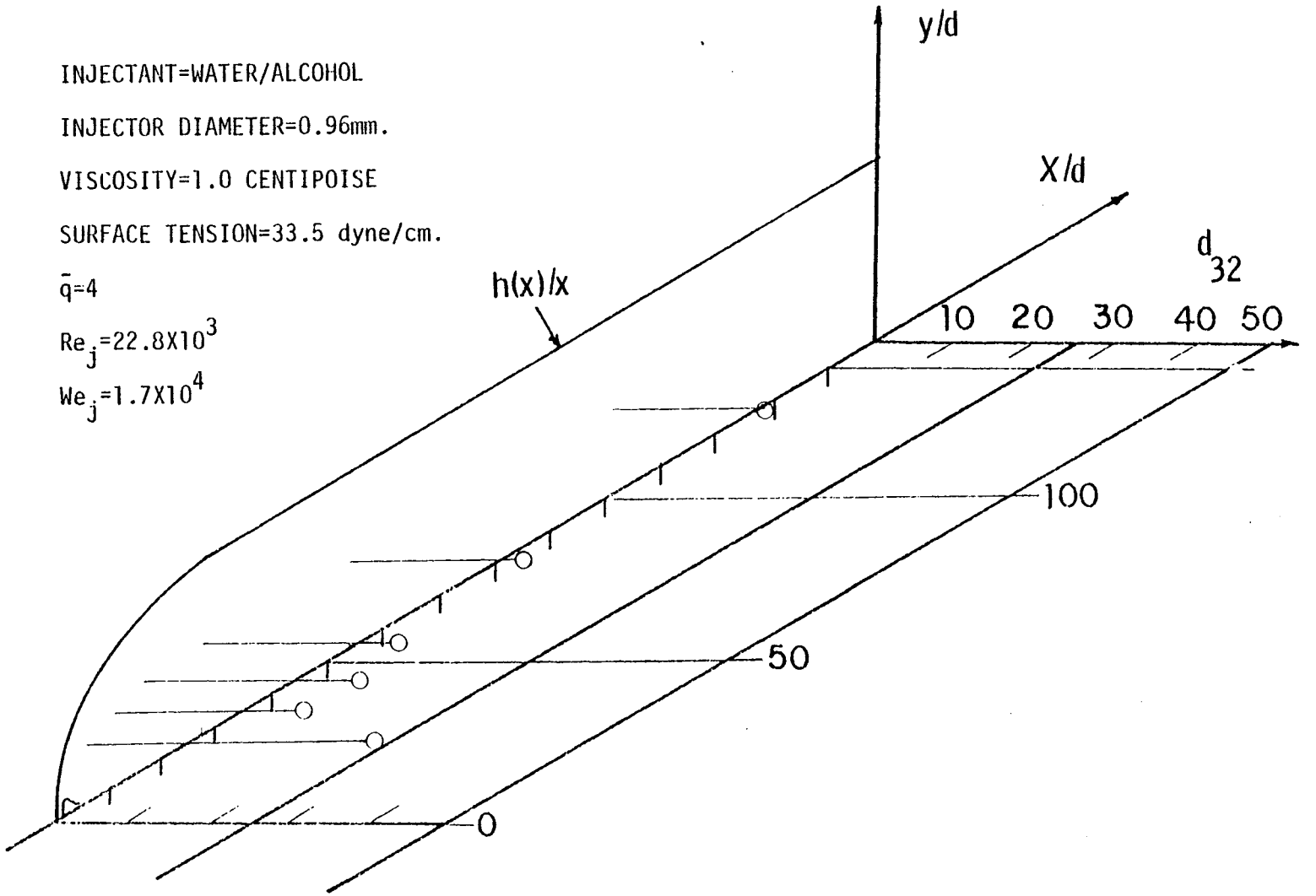

Fig. 40d MEAN DROPLET DIAMETER VARIATION IN THE PLUME FOR WATER/ALCOHOL INJECTION, CONTINUED

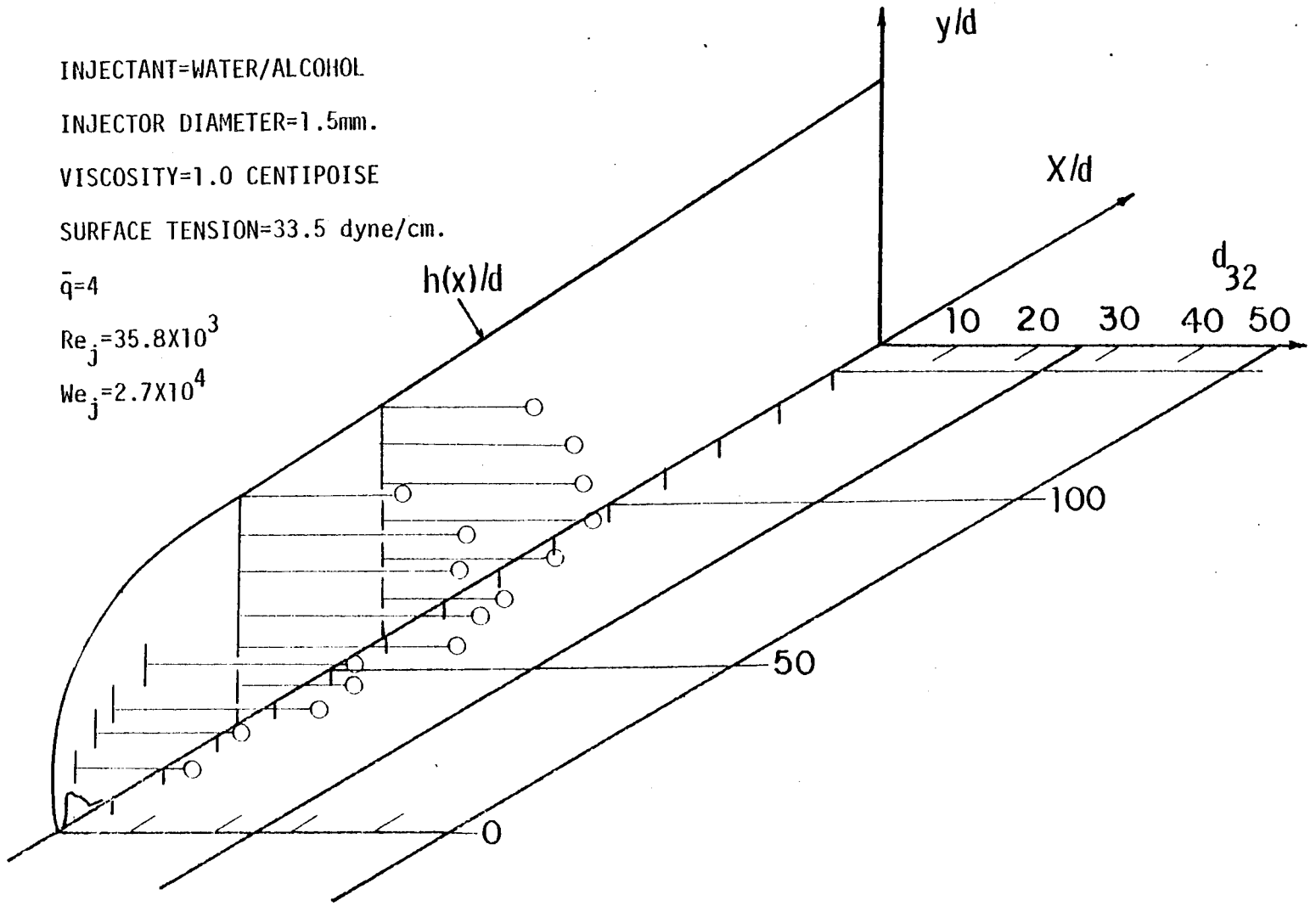

Fig. 40e MEAN DROPLET DIAMETER VARIATION IN THE PLUME FOR WATER/ALCOHOL INJECTION, CONTINUED

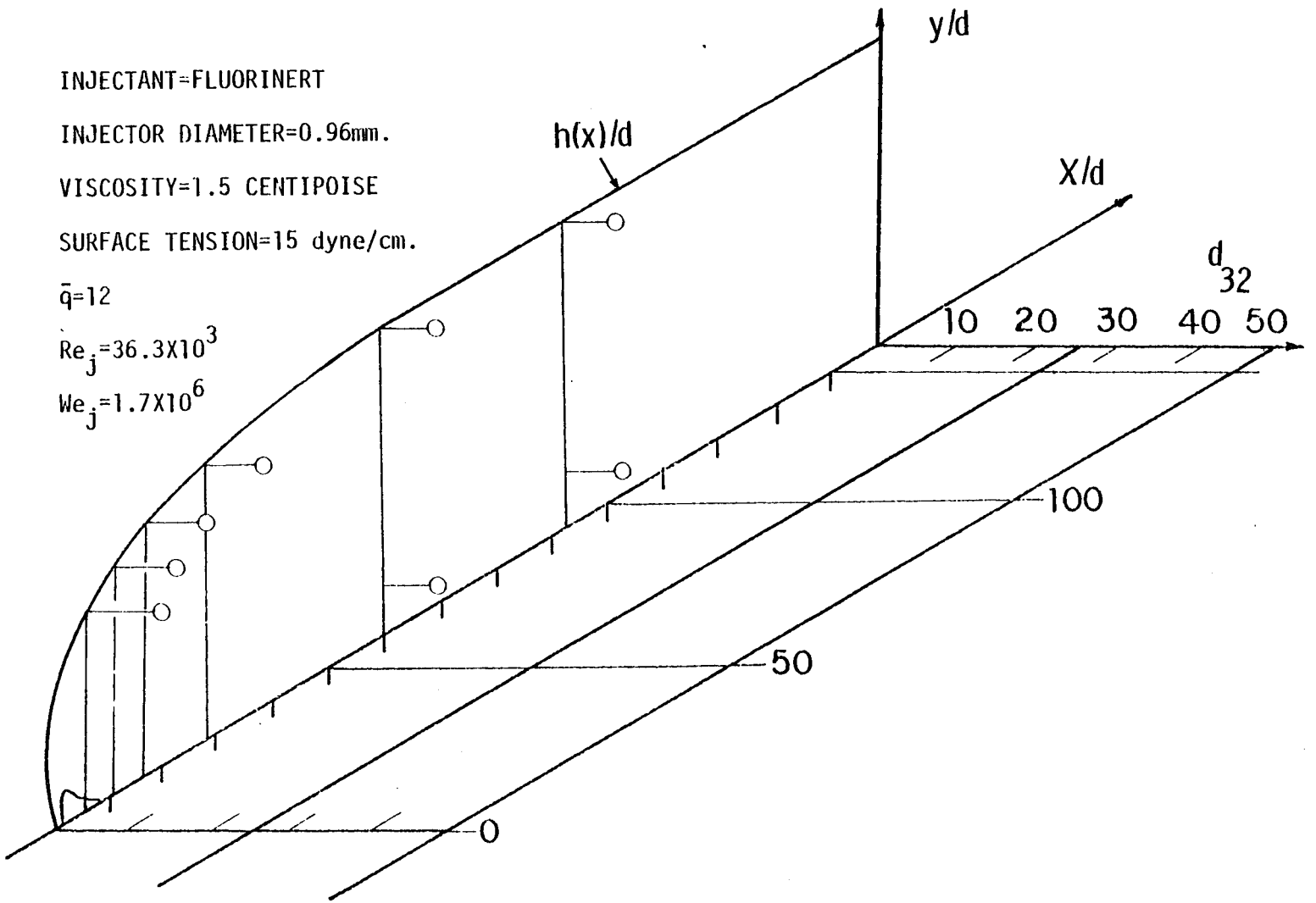

Fig, 41a MEAN DROPLET DIAMETER VARIATION IN THE PLUME FOR FLUORINERT INJECTION

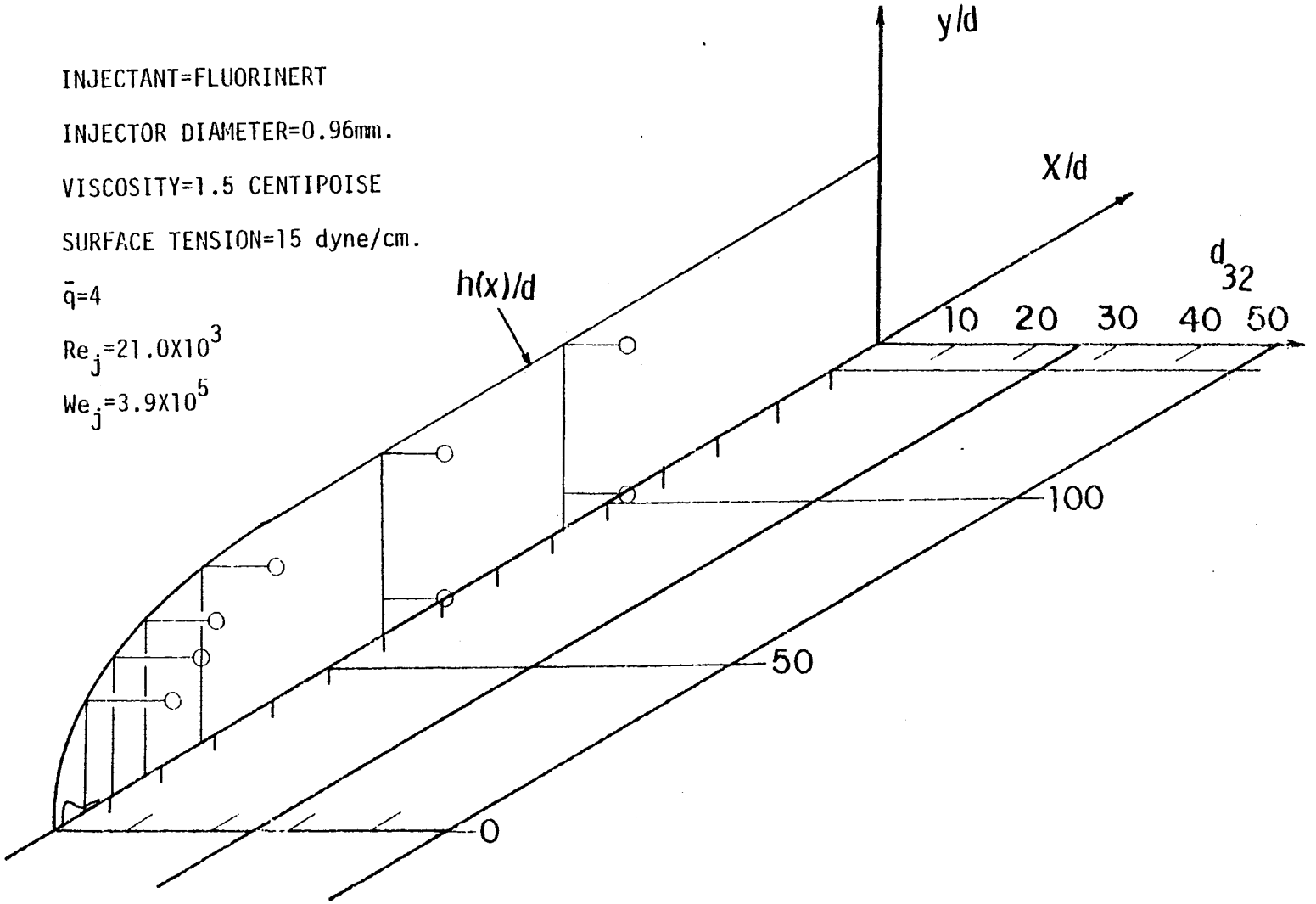

Fig. 41b MEAN DROPLET DIAMETER VARIATION IN THE PLUME FOR FLUORINERT INJECTION, CONTINUED

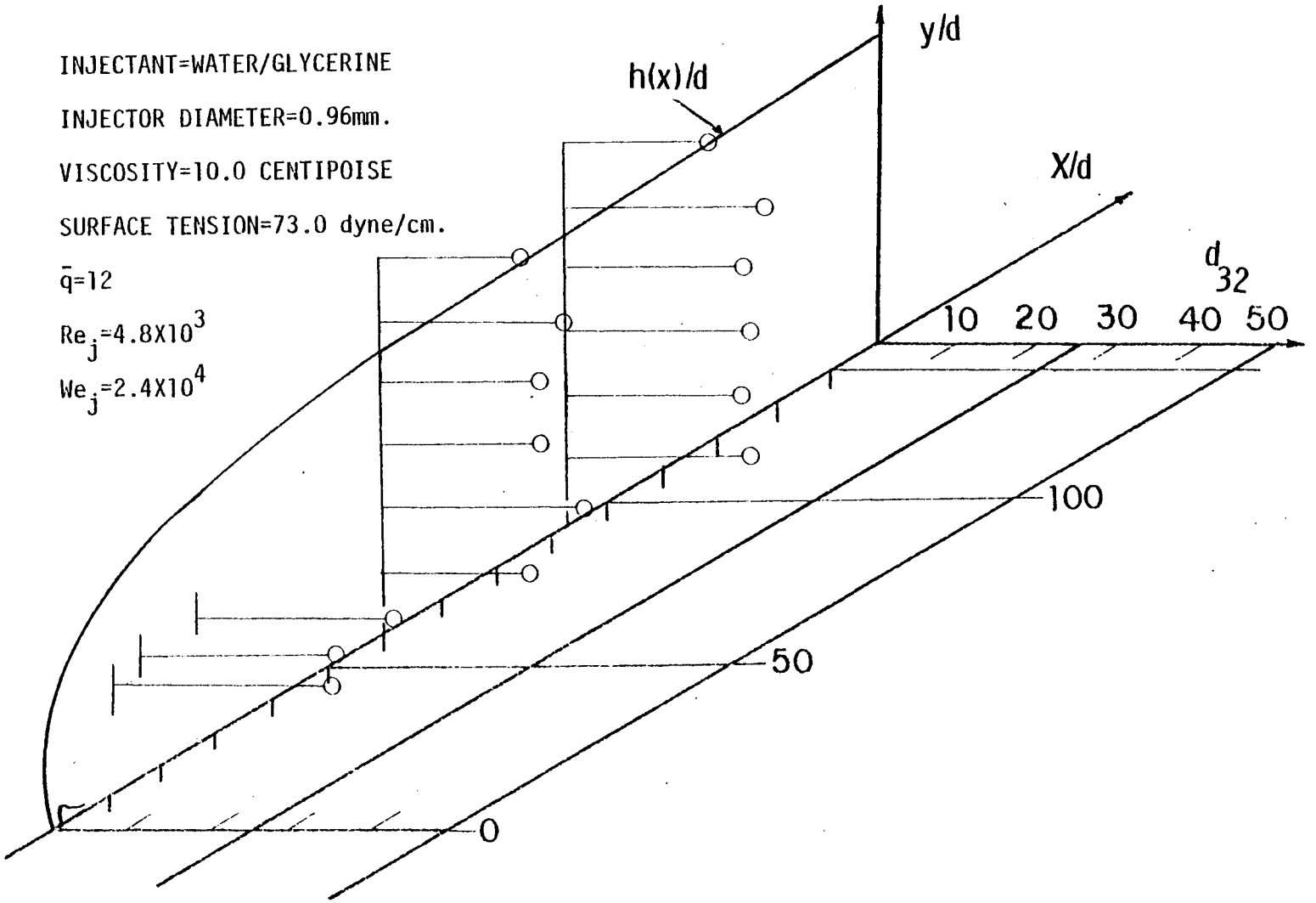

Fig. 42a MEAN DROPLET DIAMETER VARIATION IN THE PLUME FOR WATER/GLYCERINE INJECTION

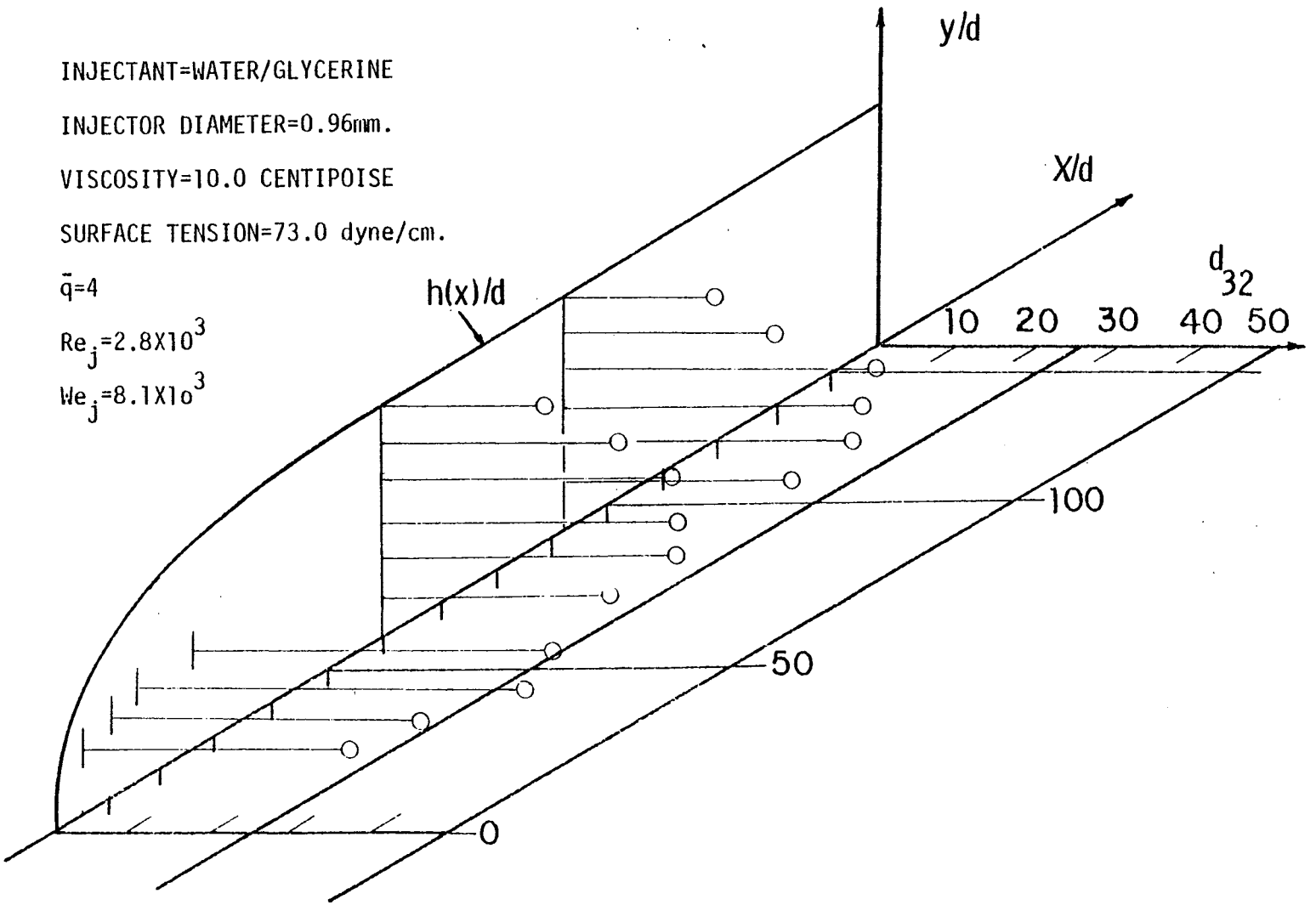

Fig. 42b MEAN DROPLET DIAMETER VARIATION IN THE PLUME FOR WATER/GLYCERINE INJECTION, CONTINUED

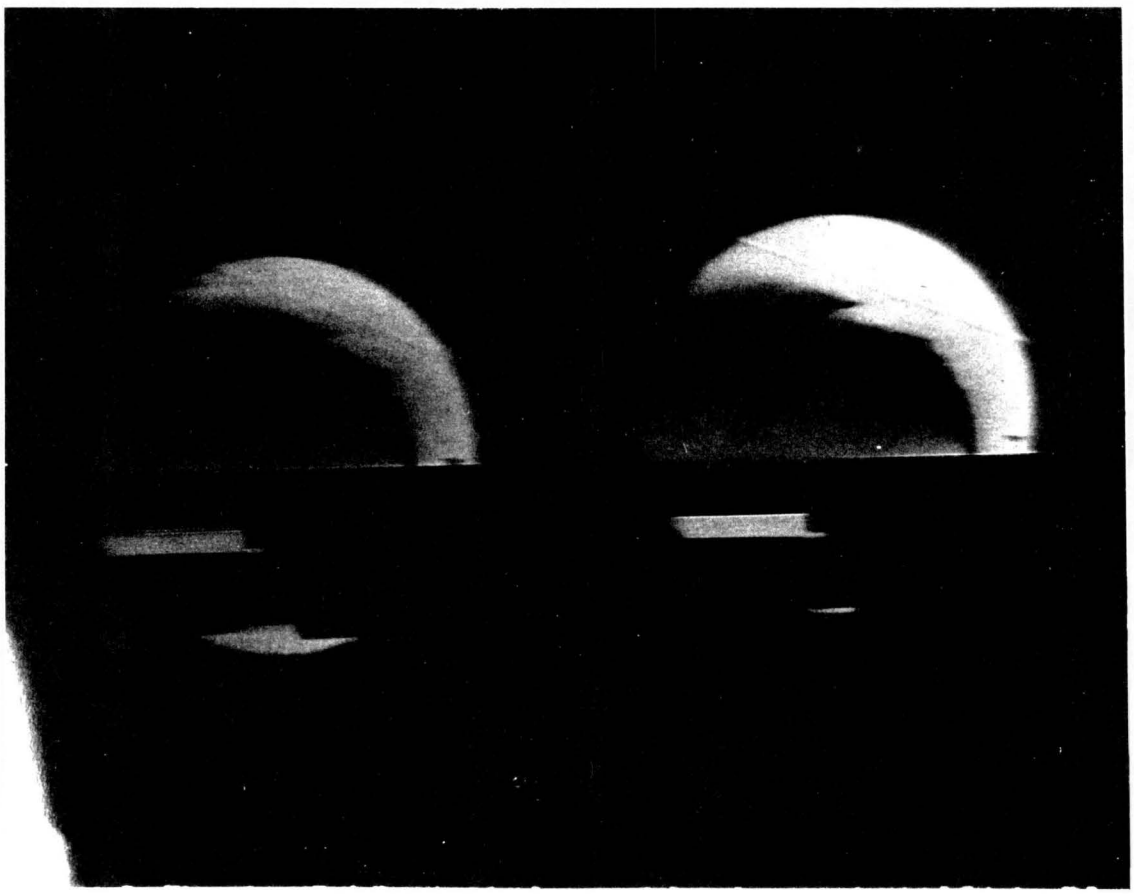

Fig. 43: Example of Multi-Exposure (Rotating Mirror) Photographs.

Water dt = 10 x 10^{-6} sec.

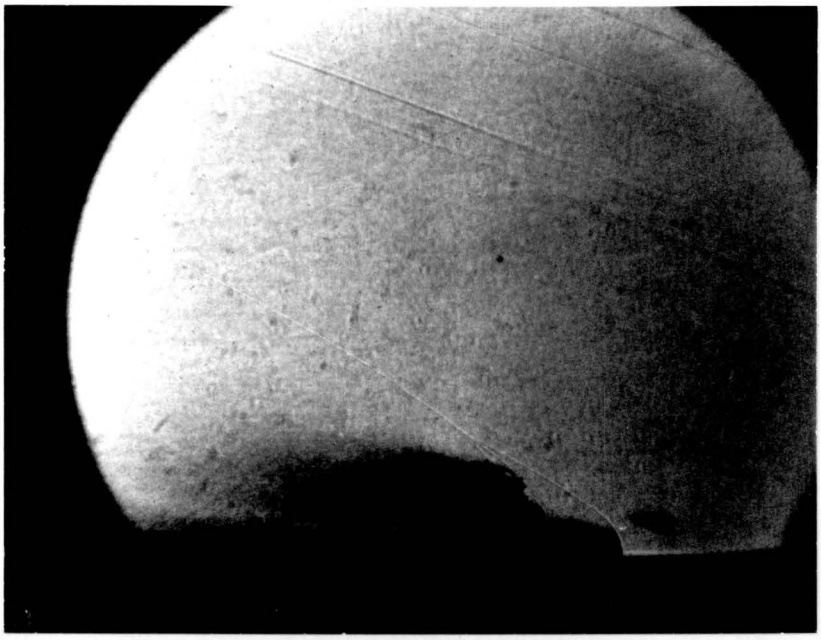

1st

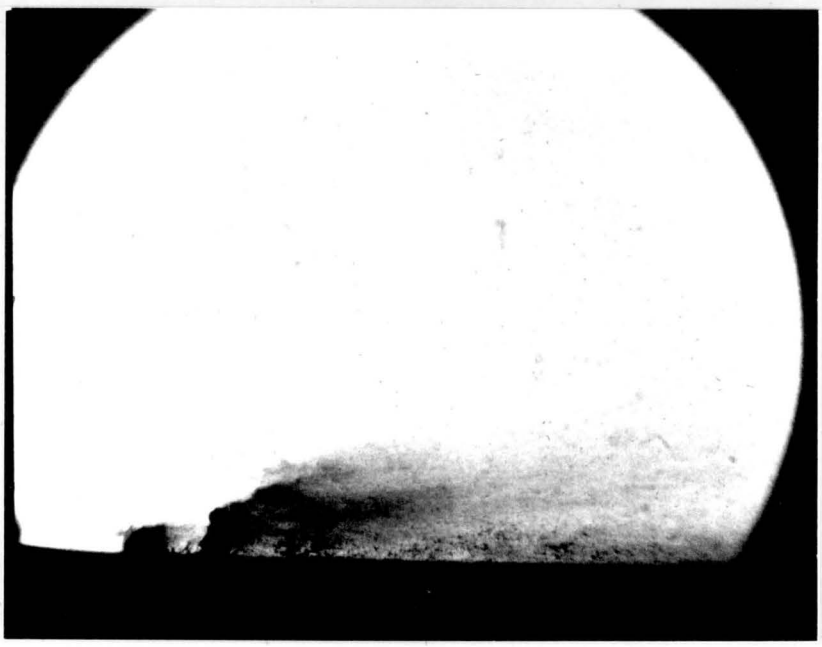

2nd

Fig. 44a: Multi-Exposure (Fixed Mirror) Photographs, Water, dt = 5×10^{-6} sec.

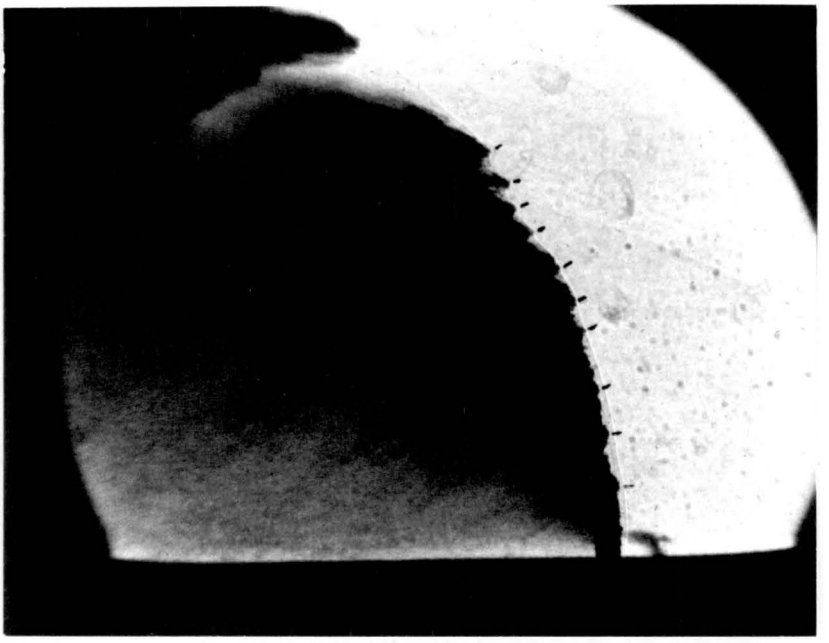

1st

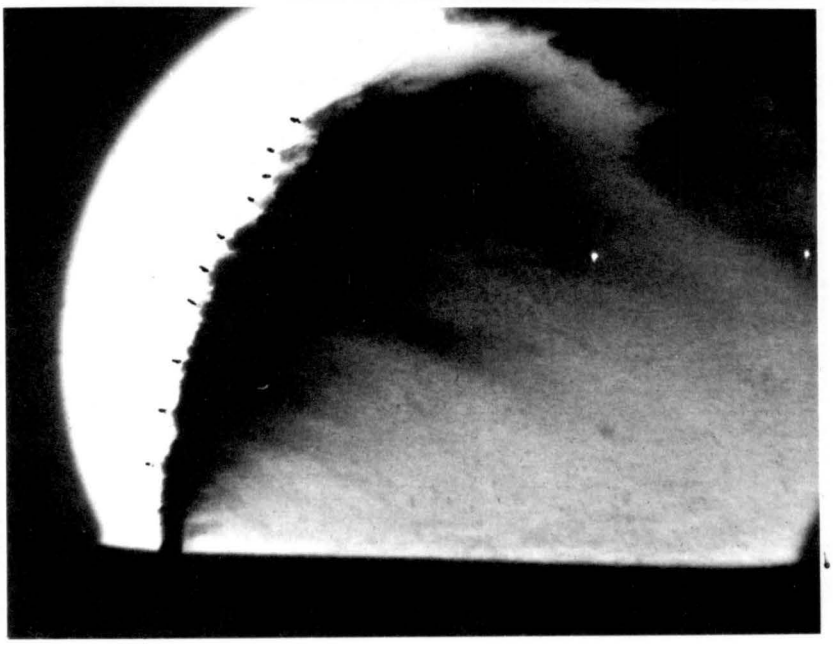

2nd

Fig. 44b: Multi-Exposure (Fixed Mirror) Photographs. Water/Alcohol, $dt = 3 \times 10^{-6}$ sec.

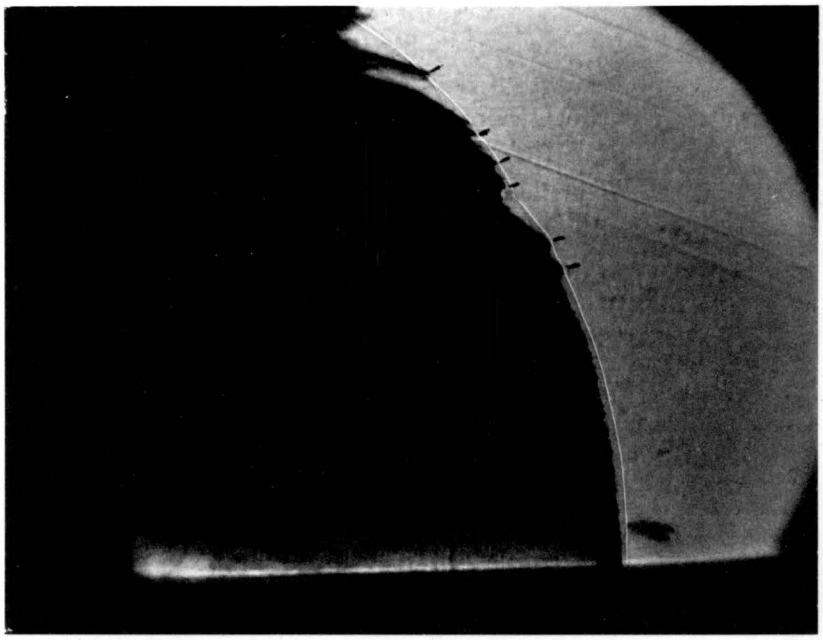

1st

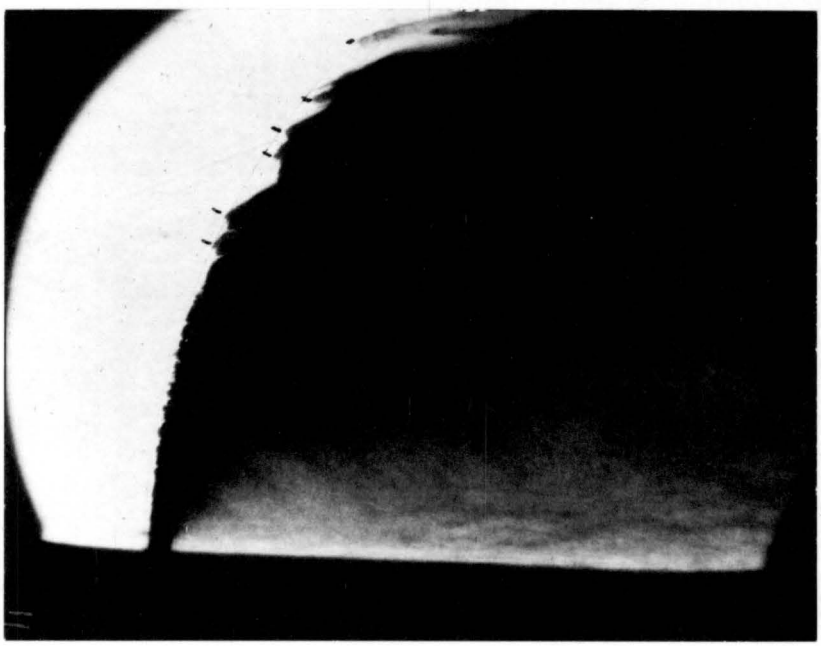

2nd

Fig. 44c: Multi-Exposure (Fixed Mirror) Photographs, Fluorinert, $dt = 3 \times 10^{-6}$ sec.

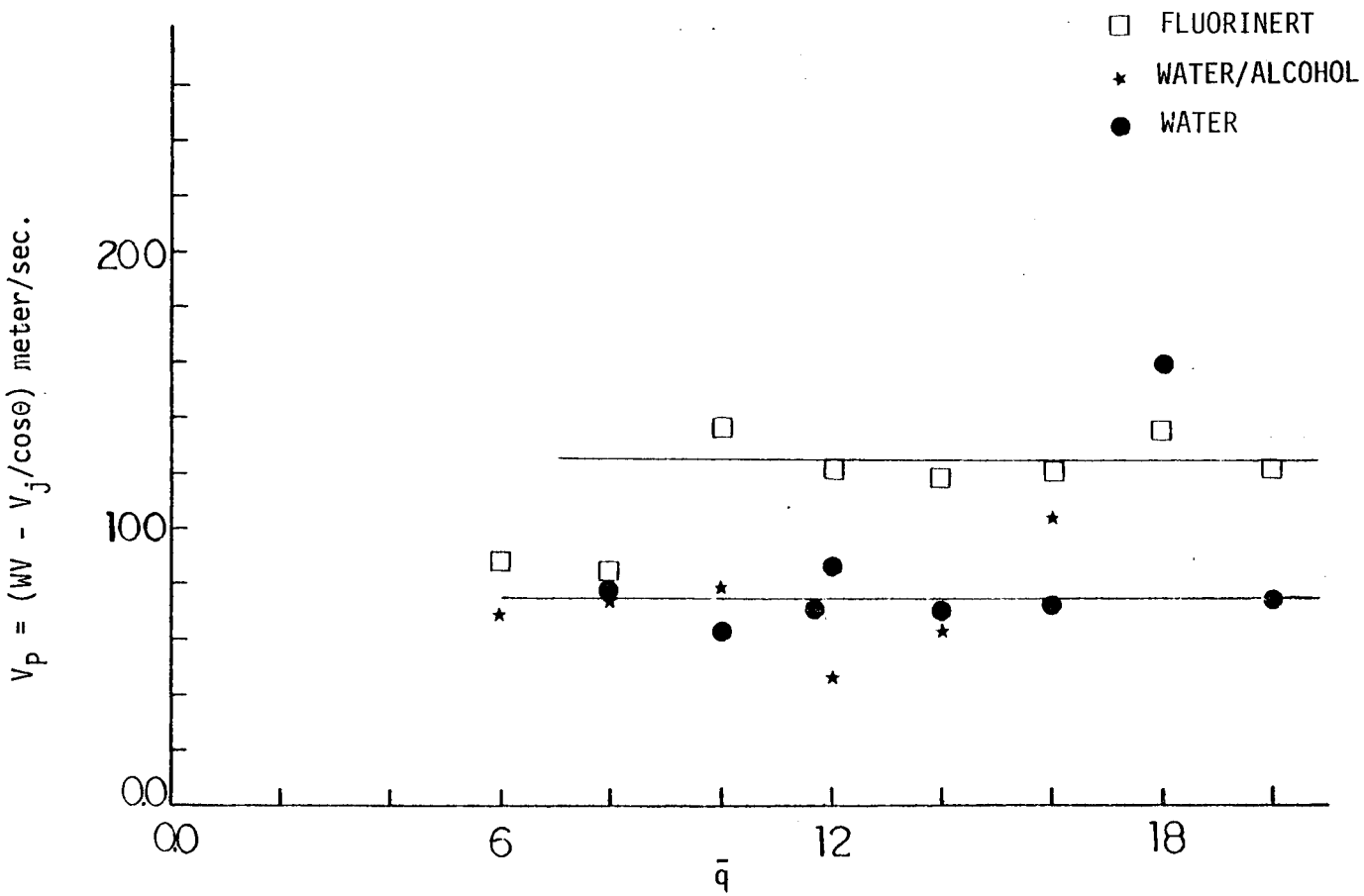

FIG. 45 WAVE PROPAGATION VELOCITY ON THE COHESIVE JET BODY VS. DYNAMIC PRESSURE RATIO, DIFFERENT SURFACE TENSION'S

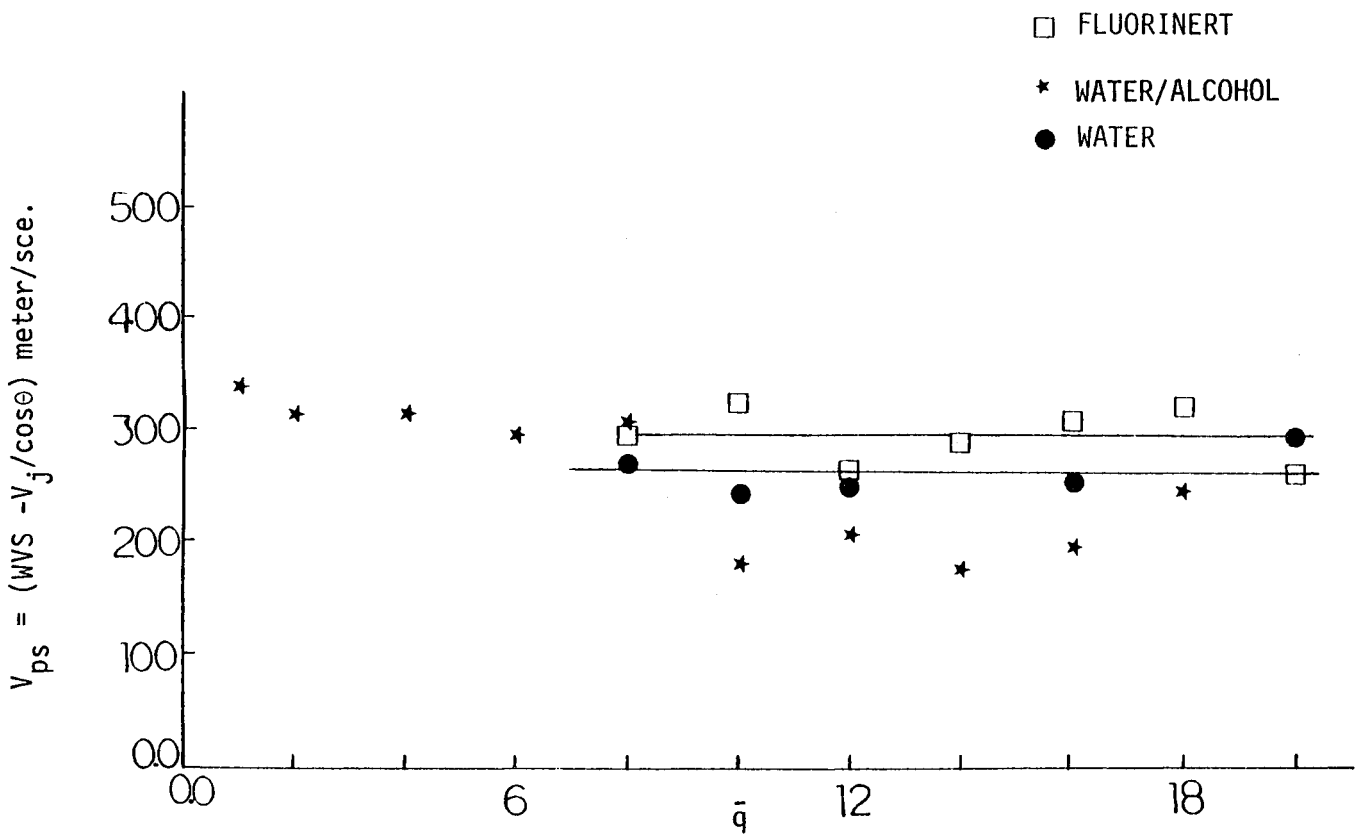

FIG. 46 WAVE PROPAGATION VELOCITY NEAR THE SONIC POINT VS. DYNAMIC PRESSURE RATIO, DIFFERENT SURFACE TENSION'S

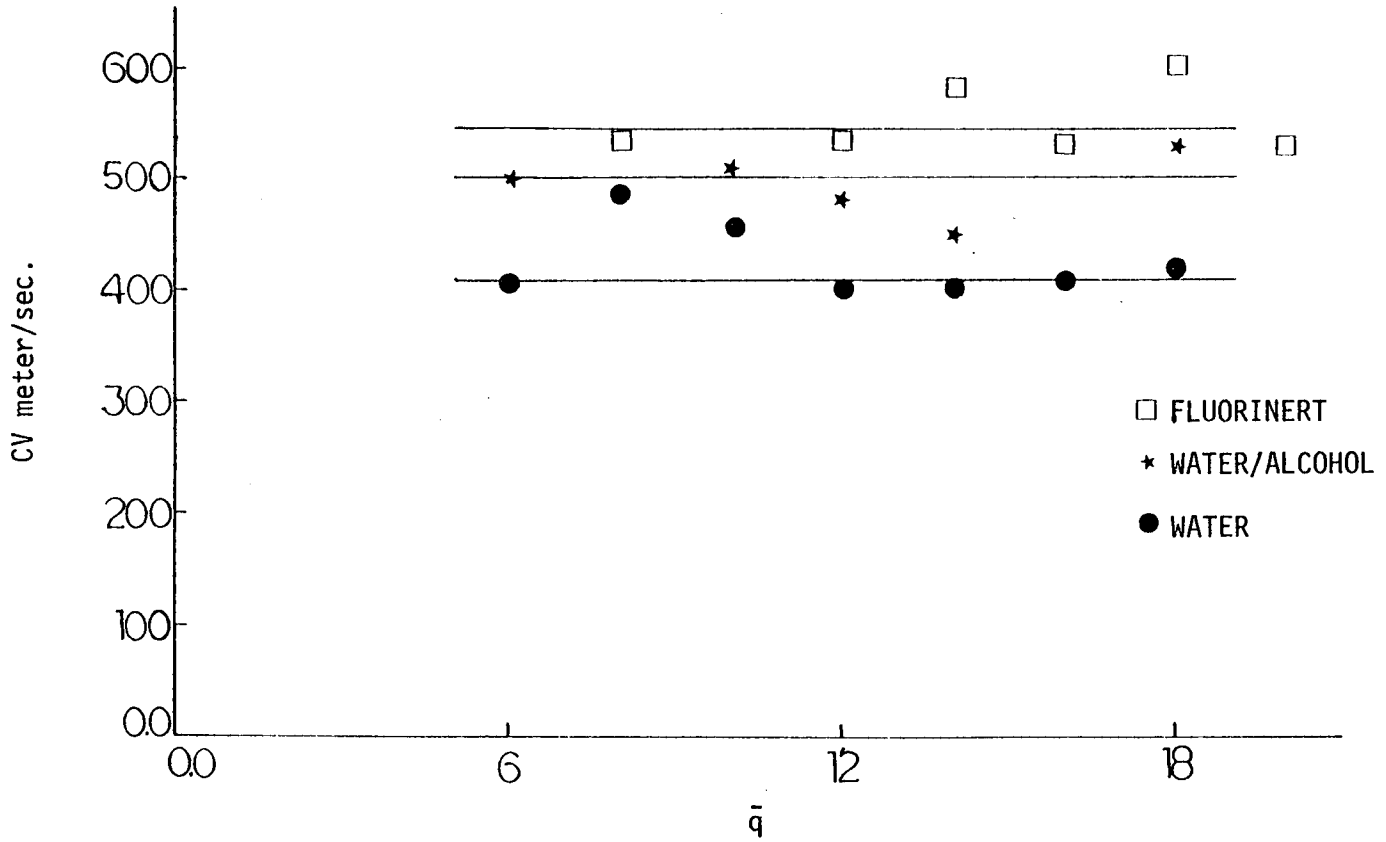

FIG. 47 CLUMP VELOCITY VS. DYNAMIC PRESSURE RATIO, DIFFERENT SURFACE TENSION 'S

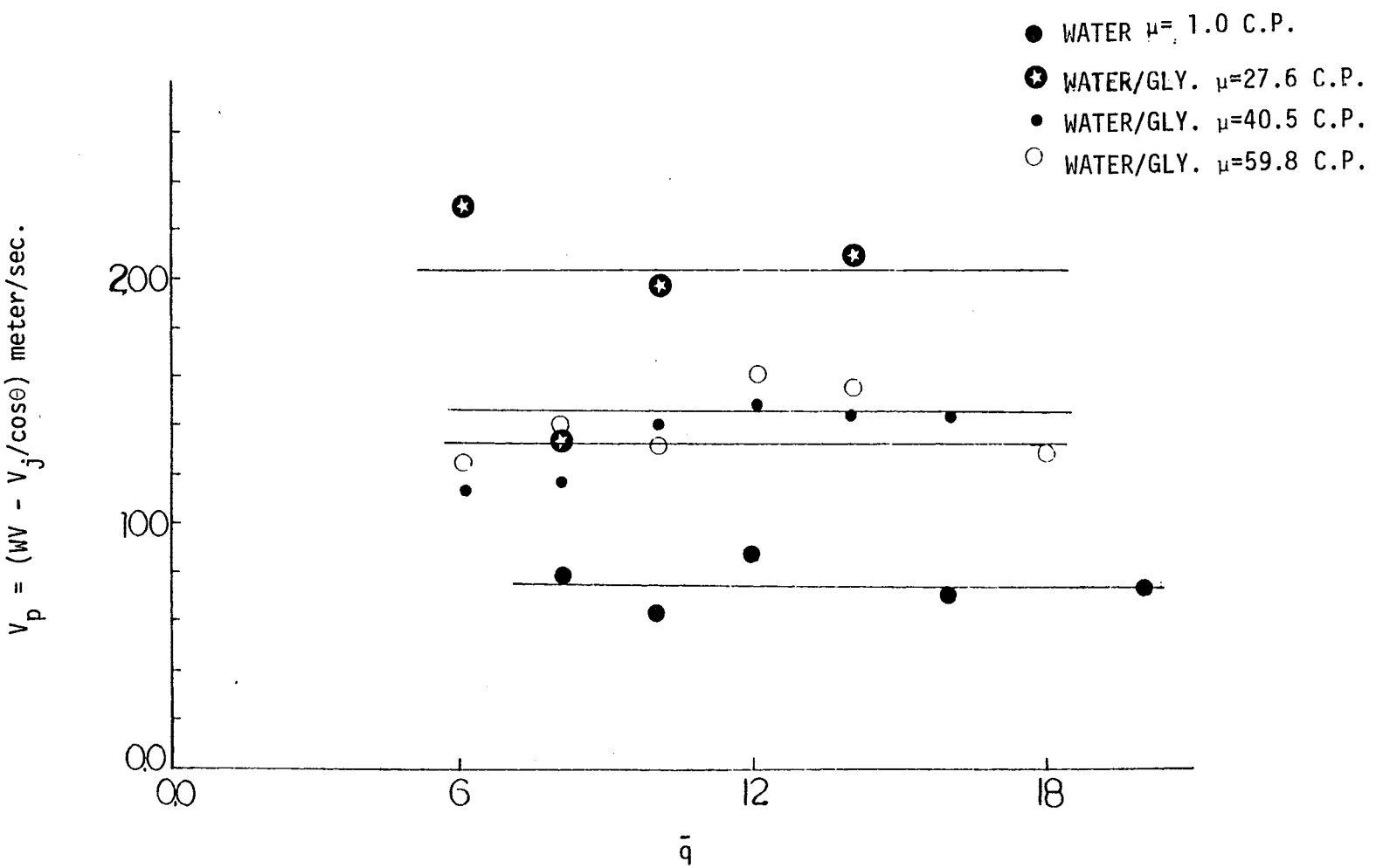

FIG. 48 WAVE PROPAGATION VELOCITY ON THE COHESIVE JET BODY VS. DYNAMIC PRESSURE RATIO DIFFERENT VISCOSITY'S

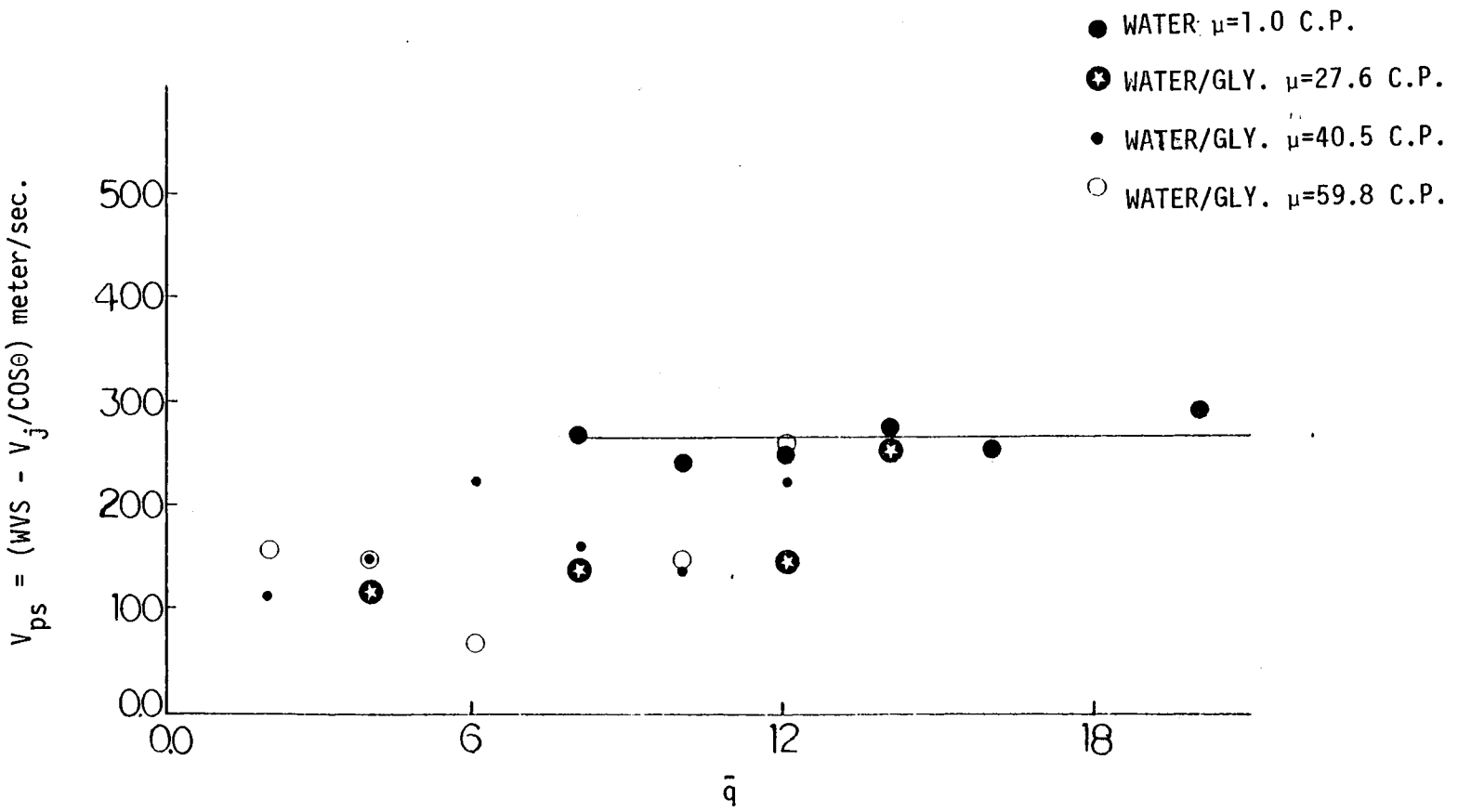

FIG.49 WAVE PROPAGATION VELOCITY NEAR THE SONIC POINT VS. DYNAMIC PRESSURE RATIO, DIFFERENT VISCOSITY'S

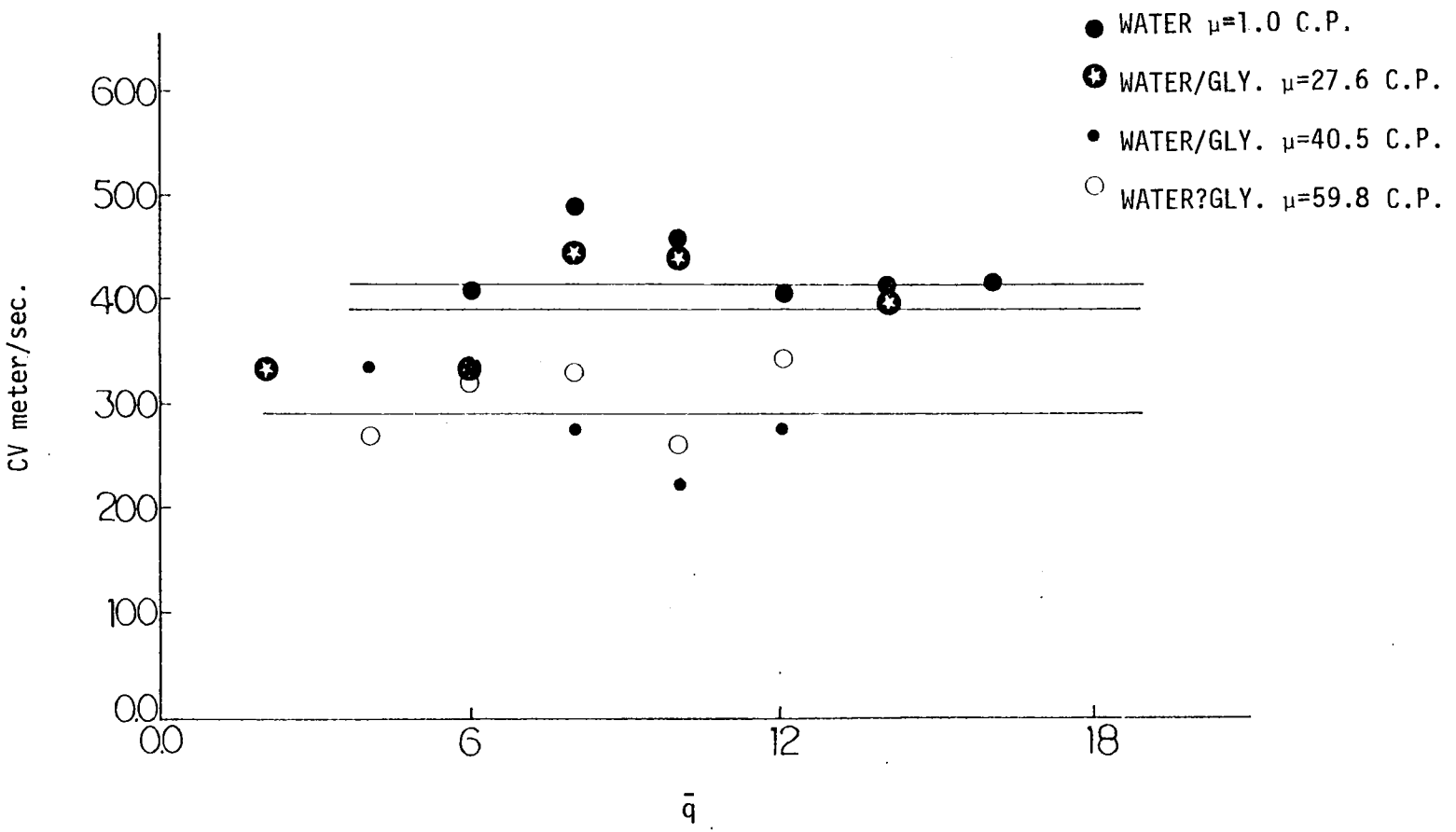

FIG.50 CLUMP VELOCITY VS. DYNAMIC PRESSURE RATIO, DIFFERENT VISCOSITY'S

TABLES

Table 1

Injectant Property

Injectant	Density (ρ) gm/cm^3	Surface Tension (σ) dyne/cm.	Viscosity (μ) centipoise
water	1.0	73.0	1.0
water/glycerine	1.15	73.0	10.5
water/glycerine	1.17	73.0	18.4
water/glycerine	1.18	73.0	27.6
water/glycerine	1.19	73.0	40.5
water/glycerine	1.20	73.0	59.8
water/alcohol	0.95	33.5	1.0
Fluorinert	1.78	15	1.5

Table 2

Wavelength, Amplitude
Jet Structure Data

Injector Diameter = 0.96 mm.
Injectant = water
Viscosity = 1.0 centipoise
Surface Tension = 73.0 dyne/cm.

	$\bar{q}$	λ/d	α/d	λ/d	$N\lambda F$	k/d	Tk/d
Regime 1	1	-	-	-	-	-	-
	2	0.5	0.2	2.5	2.0	-	1.8
Regime 2	4	0.7	0.3	2.3	3.0	-	1.3
	6	1.6	0.7	2.3	7.0	-	1.6
	8	1.2	0.5	2.4	7.0	-	3.4
	10	1.5	0.5	3.0	8.0	-	4.2
	12	1.5	0.5	3.0	7.0	-	3.8
Regime 3	14	0.8	0.5	1.6	9.0	-	3.6
	16	1.1	0.5	2.2	12.0	-	6.8
	18	1.4	0.5	2.8	9.0	-	3.6
	20	1.3	0.5	2.6	14.0	-	3.3

Table 3

Wavelength, Amplitude
Jet Structure Data

Injector Diameter = 0.96 mm.
Injectant = water/glycerine
Viscosity = 10.5 centipoise
Surface Tension = 73.0 dyne/cm.

	$\bar{q}$	λ/d	α/d	λ/α	$N\lambda F$	L/d	TR/d
Regime 1	1	1.0	0.3	4.0	3	-	-
	2	1.3	0.3	3.9	5	0.5	-
Regime 2	4	2.1	0.5	4.0	6	2.1	1.4
	6	1.8	0.5	3.3	7	1.5	1.3
	8	1.1	0.8	1.4	7	3.4	1.2
	10	1.3	0.6	2.0	8	3.0	1.5
	12	1.3	0.5	2.5	11	-	2.1
Regime 3	14	1.5	0.5	3.1	7	4.0	3.4
	16	1.6	0.7	2.5	7	3.0	4.1
	18	1.6	0.6	2.8	7	3.2	3.6
	20	1.8	1.00	1.8	7	3.0	3.2

Table 4

Wavelength, Amplitude
Jet Structure Data

Injector Diameter = 0.96 mm.
Injectant = water/glycerine
Viscosity = 18.4 centipoise
Surface Tension = 73.0 dyne/cm.

	q	λ/d	α/d	λ/	NλF	L/d	TR/d
Regime 1	1	0.5	0.1	5.0	6	3.7	-
	2	1.3	0.9	1.5	7	1.5	-
Regime 2	4	1.9	0.8	2.3	6	2.1	-
	6	2.8	0.9	3.0	6	2.3	1.0
	8	1.2	0.4	2.9	7	2.8	2.3
	10	1.7	0.7	2.3	8	2.5	1.9
	12	1.3	0.4	2.9	7	3.1	3.7
Regime 3	14	1.5	0.7	2.0	7	4.4	5.6
	16	0.9	0.4	2.5	7	3.6	2.1
	18	1.6	0.4	3.8	15	3.5	3.9
	20	1.4	0.7	2.0	15	2.6	3.7

Table 5

Wavelength, Wave Amplitude
Jet Structure Data

Injector Diameter = 0.96 mm.
Injectant = water/glycerine
Viscosity = 27.6 centipoise
Surface Tension = 73.0 dyne/cm.

	$\bar{q}$	λ/d	α/d	λ/d	$N\lambda F$	L/d	TR/d
Regime 1	1	1.2	0.5	2.4	4	1.6	-
	2	1.6	0.8	2.0	4	2.4	5.2
Regime 2	4	1.5	1.2	1.2	6	2.3	5.3
	6	1.3	1.7	0.8	7	2.5	6.6
	8	1.1	2.1	0.5	7	2.6	8.0
	10	1.3	1.3	1.0	7	4.5	7.5
	12	0.9	1.0	0.9	9	5.4	7.4
Regime 3	14	1.3	1.3	1.0	7	3.6	5.4
	16	2.0	1.3	1.5	7	3.9	4.3
	18	1.3	0.8	1.6	11	2.9	8.5
	20	0.80	0.80	1.0	14	2.4	-

Table 6

Wavelength, Amplitude
Jet Structure Data

Injector Diameter = 0.96 mm.
Injectant = water/alcohol
Viscosity = 1.0 centipoise
Surface Tension = 33.5 dyne/cm.

	$\bar{q}$	λ/d	α/d	λ/α	$N\lambda F$	L/d	TR/d
Regime 1	1	1.6	6.0	1.6	3	-	1.6
	2	2.5	0.8	3.1	3	-	2.2
Regime 2	4	2.0	0.8	3.1	3	-	3.5
	6	1.6	1.0	1.6	3	-	4.4
	8	1.6	0.4	4.0	6	-	3.4
	10	0.8	0.4	2.0	8	-	2.8
	12	1.2	0.4	3.0	-	-	3.6
Regime 3	14	2.0	0.4	5.0	4	-	6.2
	16	1.6	0.6	2.6	12	0.70	2.0
	18	1.2	0.4	3.0	-	0.90	7.3
	20	1.2	0.4	3.0	-	0.5	4.7

Table 7

Wavelength, Amplitude
Jet Structure Data

Injector Diameter = 0.96 mm.
Injector = Fluorinert
Viscosity = 1 5 centipoise
Surface Tension = 1.5 dyne/cm.

$\bar{q}$	λ/d	α/d	λ/α	$N\lambda F$	L/d	TR/d
1	0.9	0.2	5.6	2	-	-
2	1.7	0.7	2.5	4	-	-
4	2.8	0.9	3.2	4	-	6.7
6	3.3	0.7	4.7	4	-	13.5
8	1.9	0.7	2.8	4	-	11.4
10	5.0	1.1	4.5	4	-	16.6
12	1.9	1.2	1.6	7	-	13.5
14	1.4	0.7	1.9	7	-	12.2
16	1.5	0.9	1.8	7	-	12.6
18	1.9	0.8	2.4	8	-	15.0
20	2.0	0.7	2.8	8	-	-

Table 8

Jet Penetration Height
Injectant = WATER
Injector Diameter = 0.96 mm.
Viscosity = 1.0 centipoise
Surface Tension = 73.0 dyne/cm.

$\bar{q}$	1	2	4	6	8	10	12	14	16	18	20
m_j gm/sec.	9.1	12.8	18.1	22.2	25.6	28.7	31.4	34.0	36.3	38.5	40.6
v_j meter/sec.	12.4	17.5	24.8	30.4	35.1	39.2	43.0	46.4	49.6	52.6	55.5
h/d @ x/d = 5.2	4.7	5.2	7.9	9.4	11.0	12.3	15.6	15.6	16.1	16.6	17.7
h/d @ x/d = 10.4	6.0	7.2	12.0	13.5	14.6	15.4	18.2	20.8	19.8	20.8	22.9
h/d @ x/d = 26	6.7	8.1	13.5	17.7	19.6	18.7	22.4	26.6	26.0	27.6	29.1
h/d @ x/d = 52	7.8	9.4	13.5	18.7	21.9	22.1	26.0	29.0	28.6	30.7	31.4
$Re_j \times 10^3$	11.9	16.8	23.8	29.3	33.8	37.7	41.4	44.7	47.7	50.6	53.4
$We_j \times 11^3$	2.0	4.0	8.0	12.1	16.2	20.2	24.3	28.3	32.3	36.3	40.5

Table 9

Jet Penetration Height
Injectant = WATER/GLYCERINE
Injector Diameter = 0.96 mm.
Viscosity = 10.5 centipoise
Surface Tension = 73.0 dyne/cm.

$\bar{q}$	1	2	4	6	8	10	12	14	16	18	20
m_j gm/sec.	9.6	13.6	19.3	23.6	27.2	30.5	33.4	36.0	38.6	41.0	43.1
v_j meter/sec.	11.4	16.2	22.9	28.0	32.4	36.2	39.6	42.8	45.8	48.6	51.2
h/d @ x/d = 5.2	3.6	8.8	11.4	15.0	14.5	15.0	17.6	18.6	18.6	19.2	22.3
h/d @ x/d = 10.4	2.6	10.4	14.0	16.6	17.6	19.2	22.8	22.3	22.8	24.3	27.5
h/d @ x/d = 26	1.6	11.9	17.8	20.7	22.8	24.8	24.9	29.0	29.5	31.1	34.7
h/d @ x/d = 52	2.1	12.4	19.7	22.8	25.4	28.0	31.1	32.1	32.1	35.2	37.3
$Re_j \times 10^3$	1.2	1.7	2.4	2.9	3.4	3.8	4.1	4.5	4.8	5.1	5.4
$We_j \times 10^3$	1.9	3.9	7.9	11.8	13.8	19.8	23.7	27.6	31.7	35.7	39.6

Table 10

Jet Penetration Height
Injectant = WATER/GLYCERINE
Injector Diameter = 0.96 mm.
Viscosity = 18.4 centipoise
Surface Tension = 73.0 dyne/cm.

$\bar{q}$	1	2	4	6	8	10	12	14	16	18	20
m_j gm/sec.	9.6	13.6	19.2	23.5	27.2	30.4	33.3	36.0	38.5	40.8	43.0
v_j meter/sec.	11.2	15.8	23.4	27.4	31.5	35.3	38.7	41.8	44.7	47.4	50.0
h/d @ x/d = 5.2	3.1	7.2	11.9	13.5	15.0	14.5	15.0	18.1	20.7	20.7	
h/d @ x/d = 10.4	2.6	7.8	15.0	17.1	18.6	19.7	20.2	23.3	24.9	25.4	
h/d @ x/d = 26	2.1	8.1	16.6	19.7	22.8	24.9	28.0	28.5	31.6	33.1	
h/d @ x/d = 52	3.6	8.8	18.6	22.2	24.3	27.0	30.6	31.1	35.2	38.3	
$Re_j \times 10^3$	0.68	0.97	1.4	1.9	1.8	2.1	2.4	2.6	2.7	2.9	
$We_j \times 10^3$	1.9	3.8	8.4	11.6	15.3	19.2	23.2	27.0	30.8	34.7	

Table 11

Jet Penetration Height
Injectant = WATER/GLYCERINE
Injector Diameter = 0.96 mm.
Viscosity = 27.6 centipoise
Surface Tension = 73.0 dyne/cm.

$\bar{q}$	1	2	4	6	8	10	12	14	16	18	20
m_j gm/sec.	9.7	13.8	19.5	23.9	27.6	30.8	33.8	36.5	39.0	41.4	43.6
v_j meter/sec.	11.3	15.9	22.5	27.5	31.8	35.5	38.9	42.0	45.0	47.4	50.3
h/d @ x/d = 5.2	3.1	5.2	7.2	11.4	13.0	13.5	15.0	16.0	15.5	18.1	20.2
h/d @ x/d = 10.4	2.6	6.2	8.8	14.5	16.0	18.1	20.2	20.7	20.7	22.8	24.0
h/d @ x/d = 26	1.9	7.8	12.4	18.6	20.7	24.8	27.4	28.0	28.0	32.1	35.2
h/d @ x/d = 52	3.6	9.3	14.5	20.7	22.8	27.0	31.1	33.7	33.7	37.8	41.0
$Re_j x\ 10^3$	0.47	0.66	0.93	1.1	1.3	1.5	1.6	1.7	1.9	2.0	20.8
$We_j x\ 10^3$	19.9	3.9	7.9	11.8	15.7	19.6	23.6	27.5	31.6	35.4	39.4

Table 12

Jet Penetration Height
Injectant = WATER/GLYCERINE
Injector Diameter = 0.96 mm.
Viscosity = 40.5 centipoise
Surface Tension = 73.0 dyne/cm.

$\bar{q}$	1	2	4	6	8	10	12	14	16	18	20
m_j gm/sec.	9.7	13.7	19.4	23.7	27.4	30.6	33.6	36.2			
v_j meter/sec.	11.0	15.5	22.1	27.1	31.3	35.0	38.3	41.4			
h/d @ x/d = 5.2	3.1	3.6	6.2	9.1	10.4	11.4	13.5	14.5			
h/d @ x/d = 10.4	3.6	4.7	8.1	11.4	13.3	15.5	16.6	19.2			
h/d @ x/d = 26	3.6	5.2	10.6	16.0	18.1	22.3	23.6	27.4			
h/d @ x/d = 52	3.9	7.2	13.7	19.2	22.6	27.7	28.5	32.6			
$Re_j x\ 10^2$	3.1	4.4	5.2	7.6	8.8	9.85	10.8	11.6			
$We_j x\ 10^3$	1.9	3.8	7.7	11.6	15.4	1.9	23.0	27.0			

Table 13

Jet Penetration Height
Injectant = WATER/GLYCERINE
Injector Diameter = 0.96 mm.
Viscosity = 59.8 centipoise
Surface Tension = 73.0 dyne/cm.

$\bar{q}$	1	2	4	6	8	10	12	14	16	18	20
m_j gm/sec.	9.7	13.8	19.5	23.1	27.6	30.9	33.8	36.5			
v_j meter/sec.	11.0	15.5	22.1	27.0	31.2	34.7	38.3	41.3			
h/d @ x/d = 5.2	3.1	4.7	7.2	9.5	11.4	13.1	13.0	14.5			
h/d @ x/d = 10.4	3.1	5.7	8.8	12.4	16.6	16.6	16.6	16.6			
h/d @ x/d = 26	2.6	7.2	12.4	7.6	23.3	23.3	27.1	26.0			
h/d @ x/d = 52	4.1	9.4	15.0	22.2	25.4	29.0	29.5	32.1			
$Re_j \times 10^2$	2.1	3.0	4.3	5.2	6.1	6.7	7.5	8.0			
$We_j \times 10^3$	1.9	3.8	7.7	11.6	15.5	19.1	23.3	27.1			

Table 14

Jet Penetration Height
Injectant = WATER/ALCOHOL
Injector Diameter = 0.96
Viscosity = 1.0 centipoise
Surface Tension = 33.5 dyne/cm.

$\bar{q}$	1	2	4	6	8	10	12	14	16	18	20
m_j gm/sec.	8.8	12.4	17.6	21.6	24.9	27.8	30.5	32.4	35.2	37.4	39.4
v_j meter/sec.	12.5	17.8	24.6	30.9	35.7	39.9	43.7	46.4	50.5	53.6	56.5
h/d @ x/d = 5.2	3.9	6.8	9.3	10.5	13.2	15.4	14.4	16.0	17.1	18.6	17.2
h/d @ x/d = 10.4	4.6	7.7	11.0	12.9	16.3	18.6	17.8	20.2	20.2	21.9	21.8
h/d @ x/d = 26	4.2	8.32	14.0	16.8	19.4	23.0	22.5	24.9	25.3	28.0	29.0
h/d @ x/d = 52	4.3	9.5	14.1	17.1	20.2	24.1	24.1	26.1	26.4	29.4	29.5
$Re_j \times 10^3$	11.5	15.3	22.6	28.4	32.8	36.7	40.1	42.6	46.4	49.2	51.9
$We_j \times 10^3$	4.3	8.6	16.5	26.1	34.8	43.5	52.2	58.8	69.7	78.5	87.2

Table 15

Mean Droplet Diameter
Variation in the Plume
for Pure Water

Injection Diameter = 0.45 mm.
Injectant = water
Viscosity = 1.0 centipoise
Surface Tension = 73.0 dyne/cm.
$\bar{q}$ = 12.0
Re_j = 19.6×10^3
We = 11.3×10^3

x/d	y/d	h/d	D_{32} (micron)
10.9	8.3	16.4	-
22.0	9.8	19.7	24.0
32.8	10.5	21.3	21.0
54.4	11.4	23.0	19.0
109.4	6.6	24.0	12.0
109.4	12.0	24.0	14.0
109.4	21.9	24.0	13.0
207.7	6.6	24.0	12.0
207.7	12.0	24.0	14.0
207.7	21.9	24.0	15.0

Table 16

Mean Droplet Diameter
Variation in the Plume
for Pure Water

Injector Diameter = 0.45 mm.
Injectant = water
Viscosity = 1.0 centipoise
Surface Tension = 73.0 dyne/cm.
$\bar{q}$ = 4
$Re_j = 11.3 \times 10^3$
$We_j = 3.7 \times 10^4$

x/d	y/d	h/d	D_{32} (micron)
11.0	6.6	6.6	-
22.0	5.0	9.6	24.0
33.0	5.7	11.4	27.0
59.0	5.7	11.4	20.0
109.2	5.7	11.4	20.0
197.0	5.7	11.4	17.0

Table 17

Mean Droplet Diamter
Variation in the Plume
for Pure Water

Injector Diameter = 0.96 mm.
Injectant = water
Viscosity = 1.0 centipoise
Surface Tension = 73.0 dyne/cm.
q = 12
Re_j = 41.2×10^3
We_j = 2.3×10^4

x/d	y/d	h/d	D_{32} (micron)
5.2	7.2	14.5	-
10.4	9.4	18.8	13.0
16.1	10.4	20.7	14.0
26.8	10.9	21.7	14.0
60.0	6.2	24.9	11.0
60.0	9.3	24.9	11.0
60.0	12.4	24.9	14.0
60.0	15.5	24.9	14.0
60.0	18.6	24.9	14.0
60.0	21.7	24.9	13.0
60.0	24.9	24.9	13.0
93.2	3.1	24.9	14.0
93.2	6.2	24.9	14.0
93.2	9.3	24.9	13.5
93.2	12.4	24.9	16.0
93.2	15.5	24.9	16.0
93.2	18.6	24.9	16.0
93.2	21.7	24.9	16.0
93.2	24.9	24.9	10.0

Table 18

Mean Droplet Diameter
Variation in te Plume
for Pure Water

Injector Diameter = 0.96 mm
Injectant = water
Viscosity = 1.0 centipoise
Surface Tension = 73.0 dyne/cm.
$\bar{q}$ = 4
Re_j = 23.9×10^3
We_j = 8.1×10^3

x/d	y/d	h/d	D_{32} (micron)
5.2	4.6	9.3	-
10.4	5.5	10.9	19.0
16.1	6.2	12.1	19.0
26.8	6.5	14.0	23.0
60.0	3.1	14.5	14.0
60.0	6.2	14.5	14.0
60.0	8.3	14.5	23.0
60.0	12.4	14.5	21.0
60.0	15.5	14.5	14.0
93.2	3.1	14.5	17.0
93.2	6.2	14.5	19.0
93.2	8.3	14.5	23.5
93.2	12.4	14.5	23.0
93.2	15.5	14.5	10.0

Table 19

Mean Droplet Diameter
Variation in the Plume
for Pure Water

Injection Diameter = 1.5 mm.
Injectant = water
Viscosity = 1.0 centipoise
Surface Tension = 73.0 dyne/cm.
$\bar{q}$ = 4
Re_j = 36.3×10^3
We_j = 12.1×10^3

x/d	y/d	h/d	D_{32} (micron)
3.3	3.4	6.7	35.0
6.7	4.3	8.7	37.0
10.0	4.7	9.3	41.0
16.7	5.6	11.2	30.0
33.4	2.0	12.6	30.0
33.4	4.0	12.6	35.0
33.4	6.3	12.6	45.0
33.4	8.0	12.6	37.0
33.4	10.0	12.6	35.0
33.4	12.0	12.6	30.0
60.0	2.0	12.6	30.0
60.0	4.0	12.6	28.0
60.0	6.3	12.6	26.5
60.0	8.0	12.6	31.0
60.0	10.0	12.6	30.0
60.0	12.0	12.6	30.0

Table 20

Mean Droplet Diameter
Variation in the Plume
for 64/36 water/alcohol

Injection Diameter = 0.45 mm.
Injectant = water/alcohol
Viscosity = 1.0 centipoise
Surface Tension = 33.5 dyne/cm.
$\bar{q}$ = 12
Re_j = 18.4×10^3
We_j = 2.3×10^4

x/d	y/d	h/d	D_{32} (microns)
10.9	8.1	16.1	11.0
21.9	9.8	19.7	14.0
32.8	10.7	21.4	15.0
59.0	6.6	23.1	14.0
59.0	11.6	23.1	15.0
59.0	19.7	23.1	12.0
59.0	26.2	23.1	8.0
109.2	12.0	24.0	13.0
196.8	6.6	24.0	10.0
196.8	12.0	24.0	14.0
196.8	19.7	24.0	13.0
196.8	26.2	24.0	10.0

Table 21

Mean Droplet Diameter
Variation in the Plume
for 64/36 water/alcohol

Injector Diameter = 0.45 mm.
Injectant = water/alcohol
Viscosity = 1.0 centipoise
Surface Tension = 33.5 dyne/cm.
$\bar{q}$ = 4
Re_j = 10.6×10^3
We_j = 7.5×10^3

x/d	y/d	h/d	D_{32} (micron)
10.9	3.1	6.6	-
21.9	6.1	9.8	19.0
32.8	6.6	11.5	23.0
54.7	6.6	11.5	21.0
109.4	6.6	11.5	17.0
207.7	6.6	11.5	16.0

Table 22

Mean Droplet Diameter
Variation in the Plume
for 64/36 water/alcohol

Injector Diameter = 0.96 mm.
Injectant = water/alcohol
Viscosity = 1.0 centipoise
Surface Tension = 33.5 dyne/cm.
q = 12
Re_j = 39.5×10^3
We_j = 5.0×10^4

x/d	y/d	h/d	D_{32} (micron)
5.4	7.5	15.0	14.0
10.8	9.1	18.5	12.0
16.1	10.2	20.7	11.0
26.8	11.3	22.0	13.0
53.7	4.8	24.7	11.0
53.7	12.9	24.7	12.0
53.7	17.7	24.7	13.0
53.7	24.2	24.7	12.0
102.0	4.8	24.7	11.0
102.0	8.6	24.7	12.0
102.0	12.9	24.7	14.0
102.0	17.2	24.7	15.0
102.0	24.2	24.7	13.0

Table 23

Mean Droplet Diameter
Variation in the Plume
for 64/36 water/alcohol

Injector Diameter = 0.96 mm.
Injectant = water/alcohol
Viscosity = 1.0 centipoise
Surface Tension = 33.5 dyne/cm.
$\bar{q}$ = 4
Re_j = 22.8×10^3
We_j = 1.7×10^4

x/d	y/d	h/d	D_{32} (micron)
5.4	4.8	8.4	36.0
10.8	5.9	11.4	23.0
16.1	7.0	12.6	26.0
26.8	7.0	14.5	24.0
53.7	7.0	14.5	21.0
102.0	7.0	14.5	19.0

Table 24

Mean Droplet Diameter
Variation in the Plume
for 64/36 water/alcohol

Injector Diameter = 1.5 mm.
Injectant = water/alcohol
Viscosity = 1.0 centipoise
Surface Tension = 33.5 dyne/cm.
$\bar{q}$ = 4
Re_j = 35.8×10^3
We_j = 2.7×10^4

x/d	y/d	h/d	D_{32} (micron)
3.3	2.1	4.1	14.0
6.7	4.5	9.0	17.0
10.0	4.5	9.0	25.0
16.7	5.3	11.3	25.0
33.4	2.0	11.6	13.0
33.4	4.0	11.6	26.0
33.4	5.8	11.6	29.0
33.4	8.0	11.6	26.0
33.4	10.0	11.6	27.0
33.4	12.0	11.6	19.0
60.0	2.0	12.0	14.0
60.0	4.0	12.0	20.0
60.0	6.0	12.0	25.0
60.0	8.0	12.0	24.0
60.0	10.0	12.0	23.0
60.0	12.0	12.0	18.0

Table 25

Mean Droplet Diameter
Variation in the Plume
for Fluorinert

Injector Diameter = 0.96 mm.
Injectant = Fluorinert
Viscosity = 1.5 centipoise
Surface Tension = 1 5 dyne/cm.
$\bar{q}$ = 12
Re = $36.\times 10^{3}$
We = 1.7×10^{6}

x/d	y/d	h/d	D_{32}
5.2	15.0	15.0	7
10.4	18.5	18.5	7
15.6	20.4	20.7	7
60.0	3.1	24.9	5
60.0	24.9	24.9	5
93.0	3.1	24.9	5
93.0	24.9	24.9	5

Table 26

Mean Droplet Diameter
Varition in the Plume
for Fluorinert

Injector Diameter = 0.96 mm.
Injectant = Fluorinert
Viscosity = 1.5 centipoise
Surface Tension = 15 dyne/cm.
$\bar{q}$ = 4
Re = 2.1×10^3
We = 3.9×10^5

x/d	y/d	h/d	D_{32}
5.2	9.3	9.3	8
10.4	10.9	10.9	8
15.6	12.1	12.1	8
28.0	14.0	14.0	8
60	3.1	14.5	7
60	14.5	14.5	7
93	3.1	14.5	7
93	14.5	14.5	7

Table 27

Mean Droplet Diameter
Variation in the Plume
for 40/60 water/glycerine

Injector Diameter = 0.96 mm.
Injectant = water/glycerine
Viscosity = 10.0 centipoise
Surface Tension = 73.0 dyne/cm
$\bar{q}$ = 12
Re_j = 4.8×10^3
We_j = 2.4×10^4

x/d	y/d	h/d	D_{32} (micron)
10.4	8.6	17.2	26.0
15.5	9.6	19.3	24.0
25.9	9.9	19.8	24.0
60.0	5.2	23.3	17.0
60.0	10.4	23.3	24.0
60.0	15.5	23.3	19.0
60.0	20.7	23.3	19.0
60.0	25.9	23.3	22.0
60.0	31.0	23.3	17.0
93.2	5.2	23.3	22.0
93.2	10.4	23.3	21.0
93.2	15.5	23.3	22.0
93.2	20.7	23.3	21.0
93.2	25.9	23.3	24.0
93.2	31.0	23.3	17.0

Table 28

Mean Droplet Diameter
Variation in the Plume
for 40/60 water/glycerine

Injector Diameter = 0.96 mm.
Injectant = water/glycerine
Viscosity = 9.0 centipoise
Surface Tension = 73.0 dyne/cm.
$\bar{q}$ = 4
Re_j = 2.8×10^3
We_j = 8.1×10^3

x/d	y/d	h/d	D_{32}
5.2	5.3	10.6	32
10.4	6.4	12.9	38
15.6	7.0	13.9	47
26.0	7.8	15.6	44
60.0	3.1	18.7	28
60.0	6.2	18.7	36
60.0	9.3	18.7	36
60.0	12.5	18.7	35
60.0	15.6	18.7	29
60.0	18.7	18.7	19
93.0	3.1	18.7	28
93.0	6.2	18.7	35
93.0	9.3	18.7	36
93.0	12.5	18.7	39
93.0	15.6	18.7	25
93.0	18.7	18.7	18

Table 29

Disturbance Velocity Along the Jet

Injectant = water
Injector Diameter = 0.96 mm.
Viscosity = 1.0 centipoise
Surface Tension = 73.0 dyne/cm.

$\bar{q}$	v_j (m/sec.)	wv (m/sec.)	wvs	v
1	12.4	55.0	-	91
2	17.5	48.5	12.0	216
4	24.8	72.5	12.0	216
6	30.4	79.0	133	403
8	35.1	115.0	340	483
10	39.2	105.0	320	452
12	43.0	105.0	334	399
14	46.4	137.0	370	403
16	49.6	123.0	353	410
18	52.6	214.0	-	-
20	55.5	134.0	403	-

Table 30

Disturbance Velocity Along the Jet

Injectant = water/alcohol
Injector Diameter = 0.96 mm.
Viscosity = 1.0 centipoise
Surface Tension = 33.5 dyne/cm.

$\bar{q}$	v_j (meter/sec.)	wv (m/s)	wvs	cv
1	12.5	96	350	66
2	17.8	75	350	-
4	24.6	120	365	-
6	30.9	101	360	500
8	35.7	126	382	546
10	39.9	117	261	512
12	43.7	92	293	480
14	46.4	110	267	427
16	50.5	156	296	416
18	57.6	237	353	530

Table 31

Disturbance Velocities Along the Jet

Injectant = Fluorinert
Injector Diameter = 0.96 mm.
Viscosity = 1.5 centipoise
Surface Tension = 15 dyne/cm.

$\bar{q}$	v_j (m/s)	wv	wvs	cv
1	9.2	54	-	-
2	13.0	68	-	-
4	18.5	71	-	-
6	22.6	114	-	-
8	26.1	112	349	533
10	29.1	167	384	541
12	31.9	157	325	532
14	34.5	155	351	580
16	36.9	160	385	530
18	39.1	176	397	650
20	41.3	167	344	526

Table 32

Disturbance Velocities Along the Jet

Injectant = water/glycerine
Injector Diameter = 0.96 mm.
Viscosity = 27.6 centipoise
Surface Tension = 73.0 dyne/cm.

$\bar{q}$	v_j (m/s)	wv (m/s)	wvs (m/s)	cv (m/s)
1	11.3	-	-	166
2	15.9	111	-	333
4	22.5	78	154	236
6	27.5	260	-	333
8	31.8	172	200	444
10	35.5	23.5	-	444
12	38.9	213	225	-
14	42.0	257	344	401

Table 33

Disturbance Velocities Along the Jet

Injectant = water/glycerine
Injector Diameter = 0.96 mm.
Viscosity = 40.5 centipoise
Surface Tension = 73.0 dyne/cm.

$\bar{q}$	v_j (m/s)	wv (m/s)	wvs (m/s)	cv (m/s)
1	11.0	-	-	111
2	15.5	55	142	166
4	22.1	140	193	333
6	27.1	153	278	333
8	31.3	174	220	277
10	35.0	170	205	222
12	38.3	202	298	272
14	41.4	369	-	-

Table 34

Disturbance Velocities Along the Jet

Injectant = water/glycerine
Injector Diameter = 0.96 mm.
Viscosity = 59.8 centipoise
Surface Tension = 73.0 dyne/cm.

$\bar{q}$	v_j (m/sec)	wv (m/sec)	wvs (m/s)	cv (m/sec)
1	11	-	-	-
2	15.5	112	188	180
4	22.1	160	290	270
6	27.0	142	120	330
8	31.2	151	226	330
10	34.7	176	213	260
12	38.3	190	330	388
14	41.3			

The vita has been removed from the scanned document

EFFECT OF PHYSICAL PROPERTIES ON BREAK-UP AND ATOMIZATION OF LIQUID JETS IN A SUPERSONIC CROSSFLOW

by

Abdollah S. Nejad

(ABSTRACT)

A detailed study of the effects of injectant physical properties on the break-up and atomization of a transverse liquid jet in a supersonic airstream was conducted. The tests were run at Mach 3 with ambient stagnation temperature and stagnation pressure of 2.4 atm. Viscosity and surface tension of the injectant along with the injector diameter and the ratio of the jet to freestream dynamic pressures were individually varied (μ = 1.0 - 59.8 centipoise, σ = 15, 33.5, 73.0 dyne/cm., d = 0.45, 0.96, 1.5 mm., $\bar{q}$ = 1.20) and their effect on the structure and the atomization processes of the jet were established. The investigation employed a short exposure (9×10^{-9} sec.) photographic technique to establish the instantaneous structure of the jet in the crossflow. Relatively long exposure (10^{-3} sec.) photographs were obtained to study the time averaged behavior of the jet in the crossflow. Two multi-exposure photographic techniques were used to study the velocities of the surface waves that lead to jet break-up along the windward edge of the jet. By employing the Diffractively Scattered Light Method, the mean droplet diameter resulting from atomization at various transverse and axial locations in the spray plume was investigated. The important results are: 1) jet penetration in the crossflow initially

increases with increasing viscosity and then decreases, 2) jet penetration is essentially independent of surface tension, 3) for the cases of moderate viscosity and surface tension (values approximately those of water) wave growth and cross fracture of the jet column of the jet is the main mechanism of breakup and atomization, 4) for high viscosity (μ > 40 centipose) ligament formation is the principal mechanism of atomization, 5) increasing viscosity reduces wave growth on the jet surface, 6) wave speed initially increases with increasing viscosity then decreases, 7) wave speed and liquid clump velocities increase with decreasing surface tension, 8) liquid clump velocity decreases with increasing viscosity and surface tension, 9) wave propagation speed is independent of $\bar{q}$, 10) mean droplet diameter as the injector diameter decreases (D_{32} = 16 at x/d = 93.2, y/d = 12.4, d_j = 0.96 mm compared to D_{32} = 14 at x/d = 207.7, y/d = 12, d_j = 0.45 mm.), 11) increasing viscosity increases droplet diameter (D_{32} = 16 at x/d = 93.2, y/d = 12.4 μ = 1.0 to D_{32} = 21 at x/d = 93.2, y/d = 10.4, μ = 10.0), 12) decreasing surface tension decreases the droplet diameter (D_{32} = 14, σ = 73.0 dyne/cm., D_{32} = 5, σ = 15 dyne/cm.).